

CHARGING OF MACROPARTICLES EJECTED FROM A PULSED VACUUM ARC

BY

FILIP RYSANEK

B.S., University of Illinois at Urbana-Champaign, 1998

M.S., University of Illinois at Urbana-Champaign, 2002

DISSERTATION

Submitted in partial fulfillment of the requirements
for the degree of Doctor of Philosophy in Aerospace Engineering
in the Graduate College of the
University of Illinois at Urbana-Champaign, 2007

Urbana, Illinois

UMI Number: 3270015

INFORMATION TO USERS

The quality of this reproduction is dependent upon the quality of the copy submitted. Broken or indistinct print, colored or poor quality illustrations and photographs, print bleed-through, substandard margins, and improper alignment can adversely affect reproduction.

In the unlikely event that the author did not send a complete manuscript and there are missing pages, these will be noted. Also, if unauthorized copyright material had to be removed, a note will indicate the deletion.

UMI[®]

UMI Microform 3270015

Copyright 2007 by ProQuest Information and Learning Company.

All rights reserved. This microform edition is protected against unauthorized copying under Title 17, United States Code.

ProQuest Information and Learning Company
300 North Zeeb Road
P.O. Box 1346
Ann Arbor, MI 48106-1346

CERTIFICATE OF COMMITTEE APPROVAL

University of Illinois at Urbana-Champaign
Graduate College

December 7, 2006

We hereby recommend that the thesis by:

FILIP RYSANEK

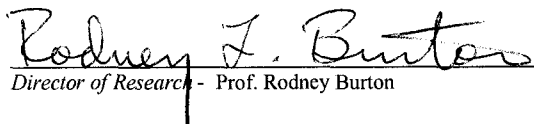
Entitled:

Charging of Macroparticles Ejected from a Pulsed Vacuum Arc

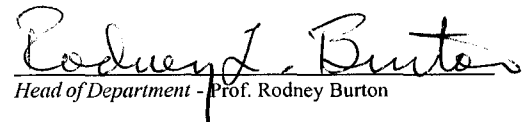
Be accepted in partial fulfillment of the requirements for the degree of:

Doctor of Philosophy

Signatures:

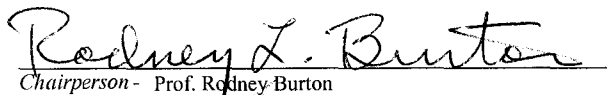


Director of Research - Prof. Rodney Burton

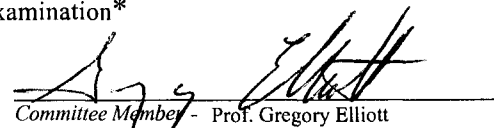


Head of Department - Prof. Rodney Burton

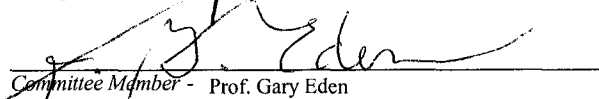
Committee on Final Examination*



Chairperson - Prof. Rodney Burton



Committee Member - Prof. Gregory Elliott



Committee Member - Prof. Gary Eden



Committee Member - Dr. Michael Keidar

Committee Member -

Committee Member -

* Required for doctoral degree but not for master's degree

© 2007 by Filip Rysanek. All rights reserved.

Abstract

A pulsed vacuum arc discharge emits a plasma as well as macroparticles in the form of micron-sized molten droplets of cathode material. Due to their direction of flight and submicron to 100 μm diameter, these macroparticles often pose a contamination threat for both spacecraft-based thrusters, and thin film deposition systems. The velocity, mass and charge of copper macroparticles emitted by a 100 A arc was experimentally measured, and compared to a model based on thermionic electron emission. The macroparticle velocity was determined by using a time-of-flight velocity filter. Less than 1% of collected particles are larger than 5.7 μm , but they account for 50% of the collected mass. The charge was calculated by measuring particle deflection in a transverse electric field. The model predicts, and the experimental results verify, that the charge on the macroparticles is positive, as compared to the negative charge expected for a DC vacuum arc. Experimental results show a roughly quadratic dependence of particle charge on the particle diameter ($q \sim D^2$), with a 1 μm particle having a positive charge of ~ 1000 electronic charges (1.6×10^{-16} C), and a 5 μm particle having a charge of ~ 25000 electronic charges. The model is particle temperature dependent, and gives $q \sim D^2$ at 1750 K and $q \sim D^{1.7}$ at 2200 K. Arguments are also made for limitations on particle temperature due to radiative and evaporative cooling.

for Jenn

Acknowledgements

This project would not have been possible without the help and support of countless people. Whether by funding my work, allowing me to use their equipment, or simply by coming to the lab to watch as I install a new high voltage power supply, a great many people have made this work possible.

First, I'd like to thank my advisor Dr. Rodney Burton. His support and guidance have been invaluable to this project and throughout my graduate career. His engineering knowledge has helped me to develop from a graduate student who asks a lot of questions into an engineer (who asks a lot of questions).

Alameda Applies Sciences Corp in California is the company that started this all with their offer to provide four thrusters for our student built CubeSat. They introduced me to the vacuum arc thrusters, and sparked the interest that would eventually become the foundation for my PhD.

I would also like to thank Dr. Michael Keidar. His suggestions ultimately guided me to the topic of my work, and his help in the modeling of these thrusters have been a great help.

I would also like to thank Lori Ballinger and the Aerospace Engineering business office for their constant support and encouragement. Lori's willingness to support a poor graduate student without funding meant a great deal.

Although we don't speak about it very often, my family has been a great source of support. Their patience and trust that yes, I will eventually finish has helped push me through these years.

The one family member that I wish to thank most of all is my wife Jennifer. She has been by my side throughout, always willing to listen to my issues, offering just the right advice, and always encouraging me to push through the hard times. Her constant willingness to help in any way possible, even when it involves sitting in the lab with me while I run a long and tedious test, has made all the difference in the world.

I want to thank the machinists in the Aerospace Engineering and Theoretical and Applied Mechanics Machine Shop for all their help. Their ability to decipher my scribblings, often written on scratch paper, has been most valuable during the design phase of this work. They are always willing to work with you to put together what you want, even if you don't know exactly what that is.

Many people have provided help in the way of guidance, equipment or even translation throughout this project. A number of pieces of equipment were borrowed for use on this project and without them, this project would have ground to a halt. Two of the power supplies key to the operation of this project were loaned by Clark Wagner and Dr. Eden of the Optical Physics lab, as well as Mike Williams. Some of the other people who offered the use of their equipment include, Gavin Horn at Amtel, Junghoon Yeom and Jea-hyeong Han in the Micro-Nano-Mechanical Systems Lab in the Mechanical Science and Engineering department. I would also like to thank Wayne Solomon, and Darren King of the Chemical Oxygen Iodine Laser group for allowing me to use their machining equipment for the items that I was able to machine myself.

The work done on the scanning electron microscope and the atomic force microscope was carried out in the Center for Microanalysis of Materials, University of Illinois, which is partially supported by the U.S. Department of Energy under grant DEFG02-91-ER45439. Scott Maclaren took time out of his already heavily taxed schedule, where he regularly works into the wee hours of the night, to perform the AFM work necessary to measure the volume of the particles. Without his help, this work would surely have been set back at least a month, while I try to learn the intricacies of the AFM. The code used to perform analysis on the AFM data, along with support for its use was given by Stefan Vinzelberg of Atomic Force F&E GmbH.

Finally, I'd like to thank all my friends for their support and patience through my graduate career. The list of friends who have helped me through these years is too long to list here. I may not have been in contact with them all as often as I should, but they are often on my mind. Launch!!

Table of Contents

List of Figures.....	ix
List of Symbols.....	xiv
Chapter 1 Introduction.....	1
1.1 Vacuum Arc Thruster	1
1.2 Cathode Spots	4
1.2.1 Macroparticles	7
1.3 Motivation.....	8
Chapter 2 Approach and Apparatus	10
2.1 Approach.....	10
2.1.1 Macroparticle Trajectory	10
2.1.2 Macroparticle Mass	15
2.1.3 Macroparticle Charge	17
2.2 Facility Description	18
2.3 Apparatus.....	18
2.3.1 Vacuum Arc Source.....	18
2.3.2 Orifice and Deflection Plates.....	22
2.3.3 Witness Plate Mount.....	24
2.3.4 Assembly	25
2.3.5 Velocity Filter.....	26
2.4 Scanning Electron Microscope Results	30
2.4.1 Macroparticle Shape on Witness Plate	30
2.4.2 Data Reduction	32
2.5 Atomic Force Microscopy Results	34
Chapter 3 Experimental Results.....	41
3.1 Witness Plate Alignment	41
3.2 Results.....	46
3.3 Error Analysis.....	53
3.4 Summary.....	57
Chapter 4 Macroparticle Charging Model.....	58
4.1 Background.....	58

4.2	Macroparticle Thermionic Emission	60
4.2.1	Negatively Charged Particle	61
4.2.2	Positively Charged Particle Without External Electric Field	61
4.2.3	Particle in Transverse Electric Field.....	63
4.3	Macroparticle Temperature	68
4.4	Model Results	70
4.5	Discussion.....	75
Chapter 5	Summary and Conclusion.....	82
5.1	Summary.....	82
5.2	Future Work.....	84
Appendix A	Velocity Filter Timing Circuit.....	86
List of References	89
Author's Biography	94

List of Figures

Figure 1.1 Schematic of the circuit used on a typical vacuum arc thruster	1
Figure 1.2 Schematic of a coaxial geometry vacuum arc thruster.....	2
Figure 1.3 Schematic of a sandwich geometry vacuum arc thruster	2
Figure 1.4 Schematic of a ring geometry vacuum arc thruster.....	3
Figure 1.5 Photograph of Illinois Orbiting Satellite (ION), UIUC 2 kg CubeSat.....	3
Figure 1.6 Scanning electron microscope image of cathode surface after vacuum arc operation	5
Figure 1.7 Characterization of potential hump formed near the cathode surface of a vacuum arc	7
Figure 1.8 Sketch of macroparticle flight from a cathode spot	8
Figure 2.1 Schematic of macroparticle trajectory through transverse electric field.....	11
Figure 2.2 Schematic (top-view) of the relationship between the orifices and line of sight in the experimental setup	13
Figure 2.3 High resolution SEM image of a macroparticle after impact. The area A is measured in pixels	16
Figure 2.4 Relationship between the macroparticle diameter in flight, and the impact surface area and diameter of collected macroparticle on the witness plate	17
Figure 2.5 Schematic of the micro-vacuum arc thruster used on UIUC CubeSat ION.....	19
Figure 2.6 Front view of vacuum arc thruster used in this work.....	19
Figure 2.7 Current in the main discharge of the vacuum arc, pulse rate = 8.5 Hz	20
Figure 2.8 Current in the trigger pulse of the vacuum arc.....	21
Figure 2.9 Side view of thruster showing thrust direction and location of orifice	22
Figure 2.10 Schematic of the boron nitride orifice.....	23
Figure 2.11 Picture of boron nitride orifices	23
Figure 2.12 Schematic of the overall experimental setup (top-view).....	25
Figure 2.13 Photo image of experimental setup without velocity filter or deflecting electric field plates.....	26
Figure 2.14 Schematic view of the velocity filter setup and operation	27

Figure 2.15 Fraction of particles allowed through the velocity filter, plotted for delay times 1100, 870, 640, and 430 μ s.....	28
Figure 2.16 Typical disk used in the velocity filter	29
Figure 2.17 Moderate magnification of macroparticles on a silicon wafer witness plate showing a wide range of MP sizes	31
Figure 2.18 High magnification image of a relatively large macroparticle "a" from Figure 2.17	31
Figure 2.19 Very high magnification of a 1 μ m diameter macroparticle	32
Figure 2.20 AFM 3D image representation of an 11.5 μ m diameter macroparticle along with two cross-section height profiles	36
Figure 2.21 AFM 3D image representation of a 2.36 μ m diameter macroparticle along with two cross-section height profiles	37
Figure 2.22 AFM 3D image representation of a 3.65 μ m diameter macroparticle along with two cross-section height profiles	38
Figure 2.23 AFM 3D image representation of a 0.78 μ m diameter macroparticle along with two cross-section height profiles	39
Figure 2.24 Particle volume measured using an atomic force microscope, plotted versus the particle impact diameter	40
Figure 3.1 Collected particle distribution without an electric field or velocity filter for two tests using the 0.51 mm orifice.....	42
Figure 3.2 Number density of particles normalized by the total number of collected particles versus the z-location, along with the calculated particle distribution width based on the 0.51 mm orifice geometry.....	43
Figure 3.3 Fraction of mass in the form of particles that are larger than a particle diameter D^* , plotted versus D^*	44
Figure 3.4 Schematic showing the relative location of the un-deflected particle distribution	44
Figure 3.5 Collected particle distribution without an electric field or velocity filter for the secondary configuration.....	45

Figure 3.6 Number density of particles normalized by the total number of collected particles versus the z-location, along with the calculated particle distribution width based on the 0.37 mm orifice geometry.....	46
Figure 3.7 Particle impact diameter versus displacement from original trajectory for particles traveling 88 m/s	47
Figure 3.8 Particle impact diameter versus displacement from original trajectory for particles traveling 110 m/s	47
Figure 3.9 Particle impact diameter versus displacement from original trajectory for particles traveling 145 m/s	48
Figure 3.10 Particle impact diameter versus displacement from original trajectory for particles traveling 214 m/s.....	48
Figure 3.11 Particle impact diameter versus displacement from original trajectory for particles traveling 110 m/s, using the secondary geometry.....	49
Figure 3.12 Accumulated macroparticle charge, plotted versus the particle diameter in flight for particles traveling 88 m/s, along with curve fit of the form $q=C_2D^2+C_1D+C_0$. Test performed using 0.51 mm orifice configuration.....	50
Figure 3.13 Accumulated macroparticle charge, plotted versus the particle diameter in flight for particles traveling 110 m/s, along with curve fit of the form $q=C_2D^2+C_1D+C_0$. Test performed using 0.51 mm orifice configuration.....	51
Figure 3.14 Accumulated macroparticle charge, plotted versus the particle diameter in flight for particles traveling 145 m/s, along with curve fit of the form $q=C_2D^2+C_1D+C_0$. Test performed using 0.51 mm orifice configuration.....	51
Figure 3.15 Accumulated macroparticle charge, plotted versus the particle diameter in flight for particles traveling 214 m/s, along with curve fit of the form $q=C_2D^2+C_1D+C_0$. Test performed using 0.51 mm orifice configuration.....	52
Figure 3.16 Accumulated macroparticle charge, plotted versus the particle diameter in flight for particles traveling 110 m/s, along with curve fit of the form $q=C_2D^2+C_1D+C_0$. Test performed using 0.37 mm orifice configuration.....	52
Figure 3.17 Curve fit of macroparticle charge, plotted versus diameter of particle in flight for all tested velocities.....	53

Figure 4.1 Plot of the potential along the z-axis (top) and the potential (dashed) and electric field (solid arrows) lines near a 10 μm diameter macroparticle with $q= 3000e$ and $E_z = 0$	62
Figure 4.2 Plot of the potential along the z-axis (top) and the potential (dashed) and electric field (solid arrows) lines near a 10 μm diameter macroparticle with $q= 3000e$ and $E_z = 5.5\times 10^5$ V/m.....	65
Figure 4.3 Plot of the potential along the z-axis (top) and the potential (dashed) and electric field (solid arrows) lines near a 10 μm diameter macroparticle with $q= 30,000e$ and $E_z = 5.5\times 10^5$ V/m	66
Figure 4.4 Thermionic current from a 10 μm diameter particle at $T_p = 2200$ K, plotted versus the MP charge, both with and without and external electric field $E_z=5.5\times 10^5$ V/m	68
Figure 4.5 Vapor pressure of copper versus temperature	70
Figure 4.6 Macroparticle charge and temperature during flight for a 1 μm diameter particle, with initial conditions: $T_o=2200$ K and $q_o=0$	72
Figure 4.7 Macroparticle charge and temperature during flight for a 10 μm diameter particle, with initial conditions: $T_o=2200$ K and $q_o =0$	72
Figure 4.8 Power loss due to radiation and thermionic emission during flight for a 1 μm diameter particle, with initial conditions: $T_o=2200$ K and $q_o =0$. $\Delta T_p = 564$ K	73
Figure 4.9 Power loss due to radiation and thermionic emission during flight for a 10 μm diameter particle, with initial conditions: $T_o=2200$ K and $q_o =0$. $\Delta T_p = 92$ K	73
Figure 4.10 Final MP charge and change in MP temperature plotted versus the starting temperature for a 1 μm diameter particle, with initial conditions: $q_o = 0$	74
Figure 4.11 Final MP charge and change in MP temperature plotted versus the starting temperature for a 10 μm diameter particle, with initial conditions: $q_o = 0$	74
Figure 4.12 Final macroparticle charge plotted versus diameter for various initial temperatures, along with an approximate curve fit to the experimental data.....	75
Figure 4.13 Error associated with the assumption of a constant charge on the MP during flight though the electric field.....	77
Figure 4.14 Comparison between final MP charge vs. diameter for two work functions.....	79
Figure 4.15 Electron mean free path in the vicinity of a 1 μm and 10 μm diameter macroparticle versus the particle temperature	81

Figure A.1 Pulse timing diagram for the velocity filter timing circuit..... 87
Figure A.2 Flow diagram for the velocity filter timing circuit..... 88

List of Symbols

A	surface area of the macroparticle on witness plate, and Richardson's constant = 1.20173×10^6 ($\text{A m}^{-2} \text{K}^{-2}$)
a,b	coefficients of D_i to volume correlation
C_p	specific heat of the macroparticle
d	separation between electric field plates
d_1, d_2	diameter of first and second orifice
D_i	macroparticle diameter after impact
D	macroparticle diameter in flight
e	electric charge = 1.602×10^{-19} (J C^{-1})
E_z	deflecting electric field
E_r, E_θ	radial and azimuthal electric field in the vicinity of the macroparticle
E_s	electric field at the surface of the macroparticle
f	copper work function
F	potential in the vicinity of the macroparticle
h	Planck's Constant = 6.626×10^{-34} (J s)
h_1	width of the cathode
h_2	width of cathode image on witness plate
I_{the}	electric current due to thermionic emission
J_{the}	current density due to thermionic emission
k	Boltzmann's constant = 1.381×10^{-23} (J K^{-1})
l_1	distance between the thruster and first orifice
l_2	distance between the second orifice and witness plate
m_e	electron mass = 9.109×10^{-31} (kg)
M_p	mass of macroparticle
n_e	electron number density
P_{the}	power lost to thermionic emission
P_{rad}	power lost to radiation
q_0	initial macroparticle charge
q	coulomb charge of macroparticle
a	macroparticle radius
s_0	macroparticle displacement on the witness plate
s	separation between the two orifices
T_0	initial macroparticle temperature
T_p	macroparticle temperature
V_0	voltage between the deflecting electric field plates
V_p	volume of the macroparticle
l	length of deflecting electric field
v_x, v_z	components of macroparticle velocity
ϵ	emissivity of the particle
ϵ_0	permittivity of free space = 8.8542×10^{-12} ($\text{C V}^{-1} \text{m}^{-1}$)
ρ_s	density of solid copper
ρ_l	density of liquid copper
σ	Steffan-Boltzmann constant = 5.670×10^{-8} ($\text{Watt m}^{-2} \text{K}^{-4}$)

Chapter 1

Introduction

Recent years have seen a decrease in spacecraft size, along with a need for smaller propulsion systems. There is a wide range of available propulsion systems for satellites larger than 1000 kg. Many of these scale down for use in smaller 100 kg, or even 10 kg satellites. However, spacecraft weighing on the order of 1 kg have few propulsion options capable of providing orbit transfer, active attitude control, or even de-saturation of momentum wheels.

1.1 Vacuum Arc Thruster

Among the few options that do exist for satellites smaller than 1 kg are vacuum arc thrusters (VAT).^{1,2,3} These thrusters provide thrust by utilizing the high velocity ions ejected from the cathode of a vacuum arc. The reduced mass of these thrusters is achieved by using an inductive energy storage (IES) power processing unit. Figure 1.1 shows a simplified schematic of the thruster circuit.

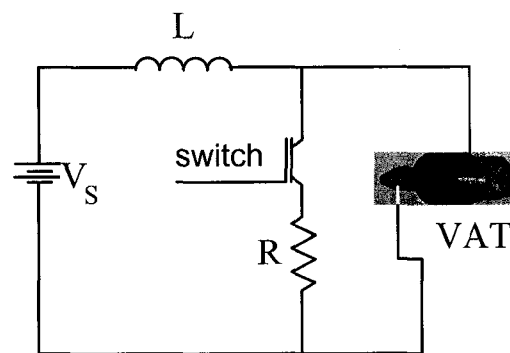


Figure 1.1 Schematic of the circuit used on a typical vacuum arc thruster

A semiconductor switch is closed to draw current from the DC, low voltage power supply through an inductor. Once the switch is opened, a voltage peak of $L \frac{dI}{dt}$ is produced, igniting a plasma by running current through a thin metal film coating between the two electrodes.^{4,5} Since these thrusters operate in a pulsed mode they can provide a wide range

of thrust and I_{sp} depending on cathode material, pulse frequency, pulse shape, geometry, and other variables.

One of the factors that makes the VAT a useful and versatile thruster is the range of geometries available. Three main geometries are commonly used in the thruster design. The coaxial geometry shown in Figure 1.2 has a central cathode and an outer anode, separated by an insulator. In the sandwich geometry shown in Figure 1.3, the thruster electrodes and insulator material are layered sheets. Finally the ring geometry (Figure 1.4) has a cylindrical cathode with a ring shaped anode separated by a ring shaped insulator.

In each of the geometries, the key to igniting the discharge is a thin metallic film on the insulator between the two electrodes. During operation, the arc discharge re-deposits a layer of cathode material on the insulator between the two electrodes, maintaining the thin metal film necessary for operation. In the ring geometry, because the insulator is opposite the location of the arc discharge, this re-deposition of the metal film on the insulator is enhanced. This makes the ring geometry more robust than the other geometries.

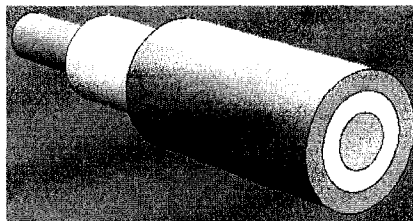


Figure 1.2 Schematic of a coaxial geometry vacuum arc thruster

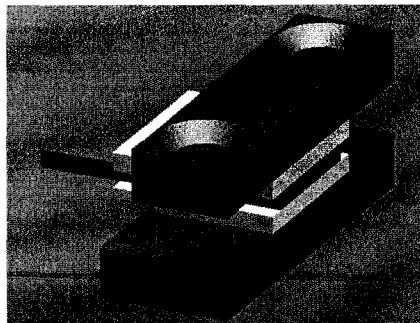


Figure 1.3 Schematic of a sandwich geometry vacuum arc thruster

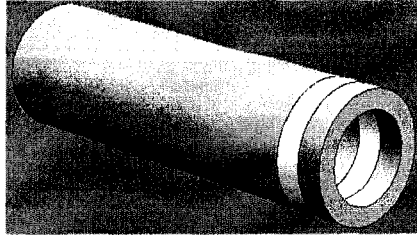


Figure 1.4 Schematic of a ring geometry vacuum arc thruster

Along with the versatility of the geometry, the VAT has the advantage of using a high density solid (namely the cathode metal) as the fuel. This allows the VAT to be more compact, and also allows the option of incorporating the thruster into the structure of the spacecraft, possibly even using the spacecraft structure as the fuel itself. A four thruster version of the VAT weighing a total of 200 g has been incorporated into a 2 kg CubeSat satellite at the University of Illinois shown in Figure 1.5.⁶ Unfortunately the launch of the CubeSat from Baikonur Cosmodrome in Kazakhstan on 26-July 2006 failed to reach orbit, and the satellite was lost⁷.

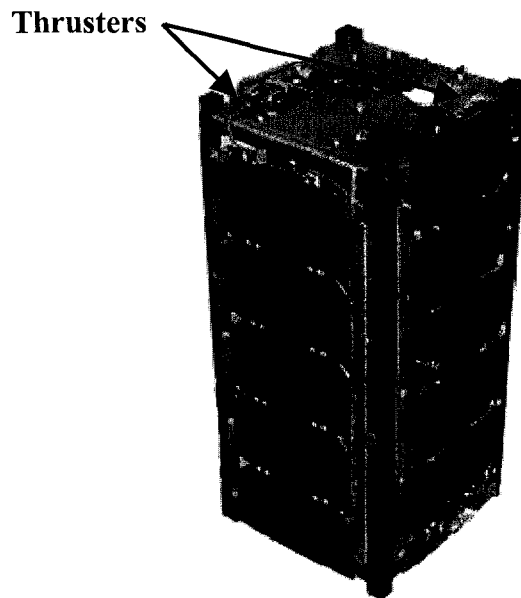


Figure 1.5 Photograph of Illinois Orbiting Satellite (ION), UIUC 2 kg CubeSat

The most recent version of the VAT is the magnetically enhanced vacuum arc thruster (MVAT). The inductor used to store the energy during operation is coiled around the

thruster itself, providing a magnetic field which collimates the exhaust, reducing spacecraft contamination and increasing thrust by 50%. In a recent study, the MVAT demonstrated an impulse bit of $2.7 \mu\text{N}\cdot\text{s}$ while firing at 50 Hz and 10 Watts.⁸ Although this thruster system (including PPU) weighs 1 kg, future work will focus on mass reduction for use on even smaller satellites.

Along with the vacuum arc thruster, vacuum arcs are used in many applications. The first published paper on the topic was written by Arthur Wright in 1877. In the 1880s, Thomas Edison applied for a patent for the use of vacuum arcs for metal film deposition for use in duplicating phonograms.⁹ Vacuum arc deposition is a process still used today. The largest commercial application includes a nitrogen background gas to form a TiN coating on drill bits greatly increasing their lifetime. Vacuum arcs are also used in high current switching. The ability to quickly change states from the insulating vacuum to the conducting metal vapor of a vacuum arc are desirable for such an application. Another application of vacuum arcs is vacuum arc degassing or remelting, where a vacuum arc is used to purify the cathode material. Degassing has the effect of removing impurities such as sulfur, while remelting results in more uniform metal alloys with a controllable grain size.¹⁰

1.2 Cathode Spots

At first glance, the vacuum arc of a VAT is a relatively simple phenomenon. However, the seemingly simple operation hides features that have been studied for decades and continue to be studied today. At moderate currents, the arc attaches to the cathode at individual spots, on the order of $10 \mu\text{m}$ in diameter, while attaching to the anode as a diffuse plasma.^{11,12,13} Each cathode spot can support a limited amount of current depending on the cathode material.¹⁴ When the current exceeds this value, (approximately 100 A for copper cathode) multiple cathode spots are formed simultaneously. The cathode spot lifetime ranges from nanoseconds to microseconds.^{15,16} Spots that have a lifetime on the order of microseconds are generally attributed to short lifespan spots that reattach to the same location. Cathode spots generally attach to small scale deformations in the cathode material, due to the enhanced electric field. The site of a previous cathode spot, has many of these deformations, often resulting in reattachment.

Since the current travels through a micrometer-sized area, the current density at the cathode surface within the cathode spot ranges from 10^9 to 10^{12} A/m².^{17,18} The extreme current densities result in a high magnetic pressure on the order of 150 atm. The high current density results in heating and melting of the cathode material, leaving small craters in the cathode surface. Figure 1.6 shows an SEM image of the cathode surface after arcing. Two types of spots are shown in this image. One highlighted cathode spot is on the order of 5 μ m in diameter. A number of smaller spots, in the upper right corner are on the order of 1 μ m in diameter. The larger crater was likely formed from a cathode spot with a longer lifetime. The size and shape of the crater is often dependent on the amount of oxide contamination of the cathode surface.¹⁹ Larger crater diameters are often generated by arcing to uncontaminated, or "clean" surfaces. Cleaning a surface is accomplished by prolonged arcing, or intense glow discharge resulting in ion bombardment.

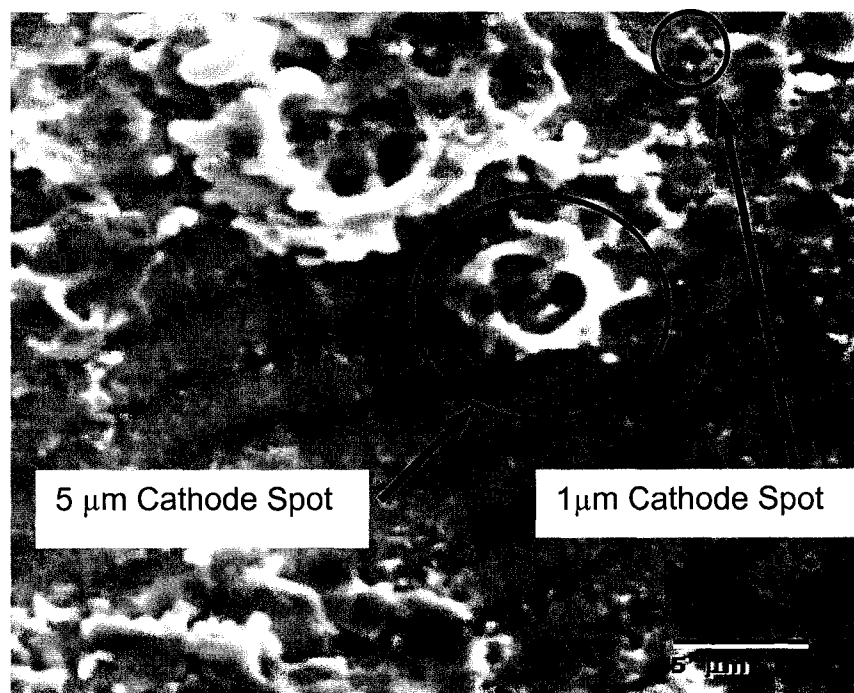


Figure 1.6 Scanning electron microscope image of cathode surface after vacuum arc operation

During the arc discharge, the cathode mass loss can be accounted for by the emission of ions, neutrals, and macroparticles in the form of molten droplets. The neutrals are evaporated from molten metal, both of the cathode and of macroparticles. Neutrals account for less than 1% of the total emitted flux because the majority are ionized by electron

collisions.²⁰ Once the neutrals are ionized, these ions are primarily accelerated toward the cathode by the sheath voltage, but a portion is accelerated away from the cathode. Daalder showed that the number of ions emitted from the cathode is proportional to the total charge transfer, accounting for 7% - 10% of the total arc current for a wide range of materials.^{21,22} While the number of ions and neutrals is generally proportional to the charge transfer, the number of macroparticles increases with the pulse duration.²² The ions emitted from a cathode spot are accelerated to high velocities ranging as high as 23 km/s, with copper ion velocities at 13.2 km/s.²³ The mean ion charge state is 2.0 for copper, and generally higher than 1 for most materials.²³ The value of the electron temperature varies from 1 eV to 4 eV within the literature.^{11,16}

The plasma of a vacuum arc is a complicated phenomenon. The electrons necessary to carry the current are extracted from the cathode by a combination of thermionic heating of the cathode surface, and field emission. When these two processes occur simultaneously in what is called thermo-field (TF) emission, the electron yield is increased non-linearly, allowing the vacuum arc to operate as it does.²⁴ The cathode surface is heated by ions accelerated toward the cathode in the sheath. The cathode surface temperature is also enhanced by resistive heating of the arc current in the cathode. The temperature of the cathode spot liquid surface ranges from 2500-4000 K for copper.^{25,26} The field emission is enhanced by the electric field at the surface, generated by the space charge of the ions flowing toward the cathode. In this way, both conditions for TF emission are caused primarily by the ion flow toward the cathode surface. The ions are generated by the ionization of neutral vapor evaporated from the hot cathode spot surface, as well as macroparticle surfaces.^{24,26}

The acceleration mechanism of the ions emitted from the cathode has been studied for decades. Initially, there were two schools of thought regarding the acceleration of the ions. One theory was that they were accelerated by the extreme pressure near the cathode spot,²⁷ enhanced by the friction drag force between the outward streaming electrons and ions. Another theory was that a potential hump (characterized in Figure 1.7) was generated by the high ion concentration near the cathode, along with the higher mobility of the electrons.^{28,29,30} However, it was later shown that the two acceleration mechanisms were

dependent on each other, and both added to the acceleration of the ions.³¹ Hantzsche calculated the contribution of the electric field, pressure gradient, and ion-electron friction to the acceleration of the ions, and concluded that each provides a comparable force, with ion-electron friction drag causing the largest contribution.¹¹

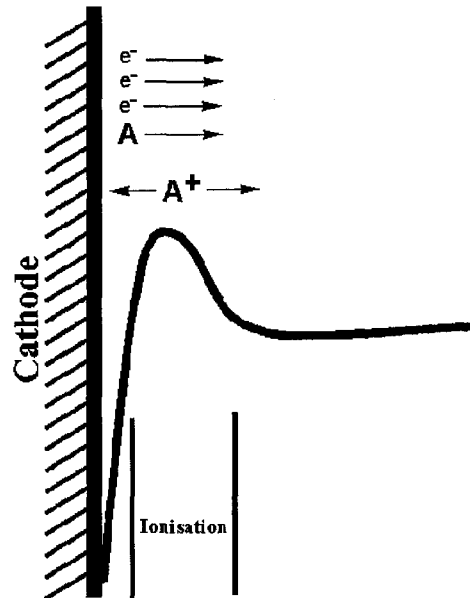


Figure 1.7 Characterization of potential hump formed near the cathode surface of a vacuum arc

1.2.1 Macroparticles

The macroparticles (MPs) emitted from the cathode are in the form of micrometer-sized molten metal droplets. These macroparticles are formed as a result of recoil from outward-directed ions acting on the molten surface of the cathode spot. Qualitatively, the high magnetic and gas dynamic pressure at the cathode spot surface splashes out droplets of cathode material from the small puddle of molten metal in the cathode spot. McClure estimated that this mechanism could eject macroparticles from the surface at velocities ranging from 20 to 200 m/s.²⁵ The measured velocity of the macroparticles ranges up to 800 m/s with a peak around 200 m/s as measured by a laser Doppler anemometer.³² It was also shown that the axial velocity of molybdenum macroparticles increases with axial location as well as instantaneous arc current. Radial velocity increases only slightly with location within the arc.³³ Qualitatively, this appears to be consistent with the work of McClure,²⁶

which states that the macroparticles are accelerated by the momentum imparted on them by collisions with high velocity ions.

Daalder's study of the exhaust mass of vacuum arcs²² has shown that the majority of macroparticles exit the cathode at a slight angle to the cathode plane. For copper, peak macroparticle emission is approximately 10° from the cathode plane, and 20° - 30° for cadmium. The study also showed that macroparticle size decreases with increasing angle from the cathode plane but increasing transfer charge increases the appearance of larger macroparticles at large angles.



Figure 1.8 Sketch of macroparticle flight from a cathode spot

As the macroparticle travels through the plasma, it collides with both electrons and ions. These collisions, along with electron emission from the surface, charge the macroparticle during its flight. A more complete model of the macroparticle charge process will be discussed in a later section.

1.3 Motivation

One of the uses of vacuum arcs is the vacuum arc thruster described above. Due to their high scalability along with a small impulse bit these thrusters have potential as an electric propulsion system on a wide range of missions. However, one factor that has limited the use of electric propulsion in general has been the risk of spacecraft contamination. The ions emitted from electric propulsion systems usually have a very high directed velocity, limiting their contribution to spacecraft contamination. On the other hand, macroparticles are emitted from the cathode of a vacuum arc at shallow angles, often making their direction of flight toward the spacecraft. They have a large mass which can disrupt optical instruments on board. They are also composed of a conductive material which can damage electronic systems.

Another common use for vacuum arcs is vacuum arc deposition. This is the use of a vacuum arc to deposit a thin metallic film coating.³⁴ The relatively high velocity of the ions emitted from the vacuum arc provides energetic depositing particles. The fact that ions are being deposited makes it possible for an electric field to be employed to accelerate or decelerate the ions, allowing for flexibility in the deposition energy. One of the prime difficulties in vacuum arc deposition is the appearance of macroparticles in the deposition layer. These macroparticles act to degrade the uniformity of the deposited layer.

One way to reduce the number of macroparticles in the deposited film is by turning the ions 90° with the magnetic field inside of a quarter-torus.³⁵ This reduces the macroparticle number density along the centerline by a factor of 50, but it is suspected that macroparticles electrically reflect from the walls of the chamber and continue to contaminate the deposition layer. Additionally increasing the magnetic field did not significantly change the macroparticle concentration on the centerline of the magnetic field.

Experiments have shown that another method of reducing the number of macroparticles in the deposited film is to negatively bias the substrate. However, not all the macroparticles are reflected by the electric field, possibly due to macroparticle charging within the substrate sheath.³⁶ Although both these methods reduce the number of macroparticles in the deposited film, the existence of any MPs still limits the usefulness of a vacuum arc deposition film.

One way to reduce macroparticle contamination on a spacecraft is to control their trajectory with electromagnetic forces. However, before a system can be designed with confidence, more needs to be known about the macroparticles. The velocity and size distribution of macro particles, including the direction of flight has already been studied. However, although there have been models developed, there is little if any experimental data on the charge of these macroparticles. This work is a study of the charge, mass, and velocity relationship of macroparticles from a vacuum arc.

Chapter 2

Approach and Apparatus

As mentioned above, macroparticles are formed when the kinetic and magnetic pressure produced at the surface of the cathode spot pushes onto the puddle of molten metal. This pressure has the effect of splashing molten copper from the cathode surface at a (generally) large angle to the surface normal. These molten droplets travel through the arc plasma, and are thus subject to electron and ion collisions. Multiple sources have indicated that the macroparticles coming from a vacuum arc are electrically charged.^{16,26,37} There is little experimental data in the literature to back up this assertion, and even less to determine the extent of the macroparticle charge. For this reason, an experiment was designed to determine the charge and velocity of macroparticles coming from a vacuum arc or other macroparticle source.

2.1 Approach

A simple experiment to measure the charge of MPs emitted from a vacuum arc could be devised by measuring the current from collected MPs. Assuming the electrical noise of the arc could be filtered, and the signal properly amplified, integrating the current would result in a measurement of the MP charge. However, simply measuring the charge of MPs emitted from a vacuum arc would not provide information such as the particle size distribution, necessary to help alleviate the problem of macroparticle contamination. For that, the mass and velocity are also necessary. To this end, an experiment was designed to measure the charge, mass and velocity of macroparticles emitted by measuring the effect that a transverse electric field has on their trajectory.

2.1.1 Macroparticle Trajectory

Consider a particle traveling through a perpendicular electric field as depicted in Figure 2.1. If the particle is assumed to have a constant charge q , the force exerted on the charged particle traveling through the electric field E_z is the charge times the electric field. The initial velocity of the particle is v_x . The electric field between two parallel plates each ℓ long, set d apart, and at voltages of $\pm V_o/2$ is calculated as

$$E_z = V_o / d \quad 2-1$$

The time that the particle spends in the electric field is ℓ/v_x . After traveling in the electric field, the component of the velocity that is parallel to E_z is

$$v_z = \frac{q}{M_p} \frac{V_o}{d} \frac{\ell}{v_x} \quad 2-2$$

where M_p and q are the mass and charge of the macroparticle respectively. The total displacement s_o of the macroparticle by the electric field is:

$$s_o = \frac{qV_o}{2M_p d} \left(\frac{\ell}{v_x} \right)^2 \quad 2-3$$

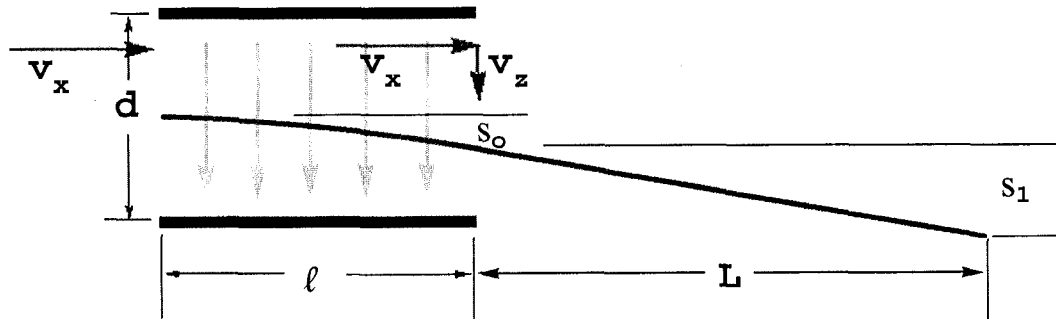


Figure 2.1 Schematic of macroparticle trajectory through transverse electric field

After the particle has exited the electric field, it travels in a straight line trajectory. The displacement of the particle after it has completed this portion of its flight is s_1 where:

$$s_1 = L \frac{v_z}{v_x} = L \frac{q}{M_p} E_z \frac{\ell}{v_x^2} \quad 2-4$$

The total particle displacement is the sum:

$$s_o + s_1 = \frac{qV_o}{2M_p d} \left(\frac{\ell}{v_x} \right)^2 + L \frac{q}{M_p} \frac{V_o}{d} \frac{\ell}{v_x^2} \quad 2-5$$

For the experimental setup in this work, the particle is collected immediately after the electric field, so the total displacement is simply s_0 .

Another possible way to design the experiment would be to use a magnetic field to deflect the particles. A particle traveling through only a magnetic field B , perpendicular to its velocity v_x , will travel with a radius of curvature of:³⁸

$$r = \frac{M_p v_x}{qB} \quad 2-6$$

If this particle traveled through a magnetic field of length ℓ , the change in direction of flight that it would experience is

$$\alpha = \sin^{-1}\left(\frac{\ell}{r}\right) \quad 2-7$$

and the total displacement of the particle at the end of the magnetic field would be

$$s_0 = r(1 - \cos(\alpha)) = \frac{M_p v_x}{qB} \left(1 - \cos\left(\sin^{-1}\left(\frac{\ell}{r}\right)\right)\right) \quad 2-8$$

If two 100 mm long parallel plates separated by 15 mm are charged to +/- 3750 V ($V_0=7500$), we can produce an electric field of 5×10^5 V/m transverse to the direction of flight. If a 0.5 μm diameter copper macroparticle, charged to 8×10^{-17} C is traveling 200 m/s, this electric field will displace it by 2.9 mm. This displacement is easily measurable by collecting the macroparticles on a witness plate. On the other hand, if we were able to produce a 1 T magnetic field that is 100 mm long, then the displacement of the same macroparticle would be 1.6 μm . Such a displacement, only three particle diameters is barely measurable. For this reason, an electric field was chosen to displace the macroparticle for this experiment.

To measure the displacement s_0 , the particles are collected on a witness plate. The most important characteristic of the witness plate is that the surface be clean, flat and polished to make the collected macroparticles easily visible in a scanning electron microscope or optical

microscope. Polished silicon wafers are readily available and come polished to within nanometer roughness. Silicon wafers have the added benefit of having a significantly different atomic weight than most cathode materials considered for this study. This is useful because the back-scattered electron detector in the SEM shows a high contrast based on molecular weight. This simplifies the search for macro particles, and allows for the use of a lower resolution image to establish the location and size of the particles.

In order to measure the displacement on the witness plate, the macroparticles coming from the vacuum arc must first be collimated or filtered to allow only MPs with a certain trajectory to impact the witness plate. This is done by firing the macroparticles through an orifice. The objective is to produce a distribution area of collected macroparticles on the witness plate that is relatively small. Assuming a straight line MP trajectory, the smallest distribution that is possible with an orifice would occur if the orifice were infinitely small. In such a case, if the witness plate and cathode source were equidistant from the orifice, the distribution on the witness plate would be the size of the cathode itself, with the location of the macroparticle inside the distribution corresponding to the mirror image of the initiation point of the MP. If two orifices are used, the portion of the witness plate that is visible through the orifices becomes limited. This is done in order to reduce the chances that macroparticles generated by stray arcing away from the cathode result in a macroparticle on the witness plate. A top-view schematic of this setup is shown in Figure 2.2, where h_1 represents the width of the cathode and h_2 represents the image of the cathode or the macroparticle distribution on the witness plate. The diameters of the orifices are labeled d_1 and d_2 , with $d_1 > d_2$. The distance between the cathode and the first orifice is l_1 , the distance between the second orifice and the witness plate is l_2 , and the distance between the orifices is s .

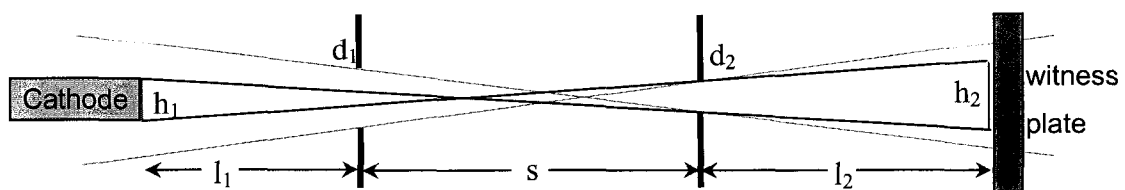


Figure 2.2 Schematic (top-view) of the relationship between the orifices and line of sight in the experimental setup

With the assumption that $d_1 > d_2$, using similar triangles, we can find the width h_2 according to the following equation.

$$\frac{\frac{h_1}{2} + \frac{d_2}{2}}{l_1 + s} = \frac{\frac{h_2}{2} - \frac{d_2}{2}}{l_2} \quad 2-9$$

$$h_2 = \left(\frac{h_1 + d_2}{l_1 + s} \right) l_2 + d_2$$

By adjusting the location and size of the cathode, the size of the macroparticle distribution can be kept to a few millimeters. With the addition of an electric field after the second orifice, the macroparticles can be deflected sufficiently to measure their deflection from the original trajectory. Then, by determining the velocity and mass of the macroparticles, the charge of each MP can be determined.

This calculation assumes that there is no interaction between the orifice and the macroparticle in flight. However, if the particle has a charge, and the wall of the orifice is at a ground potential, the particle trajectory may be affected by the attraction of the charge to its image charge in the ground plane. The magnitude of the image charge is equal and opposite to the charge of the macroparticle. The closest that the macroparticle could be to the wall of the orifice is if it were virtually touching the wall, or one particle radius. For this case, the force exerted on the particle is estimated to be:

$$\text{Force} = \frac{q^2}{4\pi\epsilon_0 D^2} \quad 2-10$$

where D is the particle diameter and ϵ_0 is the permittivity of free space.

If we assume that the particle charge is increasing linearly with particle diameter,³⁹ and is in the range between 10^{-16} to 10^{-15} Coulombs, then the effect of the image charge on the particle motion is negligible. This is simply a 1D calculation, and does not consider the effect of the entire circular orifice, which would reduce the force acting on the particle. Nor does this calculation take into account 3D effects as the particle is approaching the orifice.

However, because the charge of the particles is not known, a non-conducting orifice should be used to reduce or eliminate this effect.

Using Eq. 2-9 for the particle displacement on the witness plate, the relation for the charge of the MPs as a function of the mass M_p , velocity v_x and displacement s_o is:

$$q = 2 \frac{s_o M_p}{\ell^2 E_z} v_x^2 \quad 2-11$$

2.1.2 Macroparticle Mass

From Eq. 2-12, in order to determine the charge of the MP, both its trajectory and mass must be known. The displacement s_o of the MP on the witness plate describes its trajectory, while the size of the MP on the witness plate is an indication of the macroparticle mass. By estimating the volume V_p of collected MPs from measurements taken of individual particles,²² Daalder generated a curve fit to correlate the measured outer diameter of the impacted particles to the volume of a macroparticle. In Daalder's work, this relation took the form:

$$V_p = a D_i^b = a \left(\frac{4}{\pi} \right)^{\frac{b}{2}} A^{\frac{b}{2}} \quad 2-12$$

where the impact diameter D_i is in μm and the volume V_p is in μm^3 , where the coefficients a and b for copper are 0.178 and 2.672 respectively. Because the macroparticles are circular on the witness plate surface, the volume V_p is also written in terms of the area A (Figure 2.3) of the impacted MP. For this work, an Asylum MFP-3D atomic force microscope (AFM) was used to take measurements of particles impacted on the witness plate. These measurements resulted in a detailed height profile of the impacted particles. The results of these measurements are described in detail in Section 2.5, including 3D images representing some of the measured particles. A particle analysis routine was used to calculate the volume of the particles,⁴⁰ and a curve fit of the data reveals the values of the coefficient a and b of Equation 2-12 to be 0.0628 and 2.828 respectively. Some possible reasons why these values are different from those in Daalder's work will also be discussed in Section 2.5.

The software used during the analysis of the SEM images gives the number of pixels that each particle encompasses. This correlates to the area A of the impacted macroparticle in micrometers squared. Since the impacted macroparticles are circular in the SEM images, the diameter is calculated from the impact area A. Figure 2.3 is a high resolution SEM image showing a MP after impact.

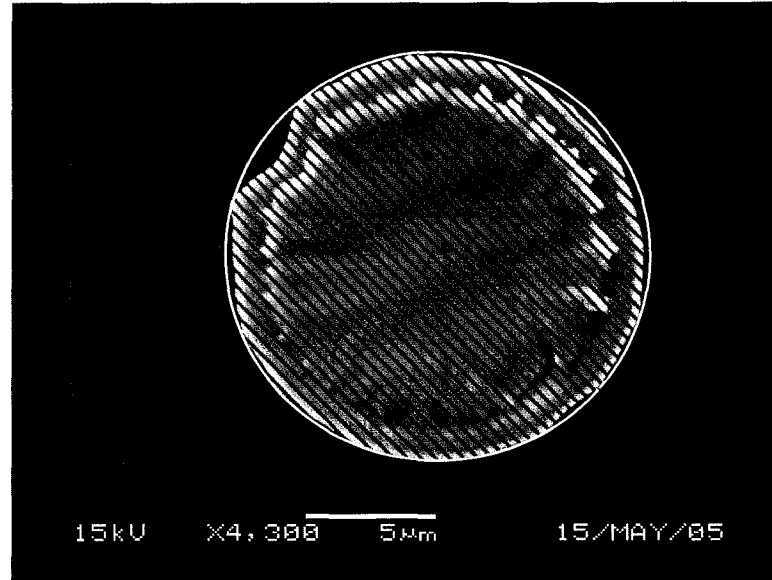


Figure 2.3 High resolution SEM image of a macroparticle after impact. The area A is measured in pixels

Equation 2-12 along with the volume of a sphere, results in a relation between the impacted surface area in μm^2 and the diameter of the macroparticle during the flight. To get the actual flight diameter of the liquid copper, the volume is scaled by the ratio of densities of copper in solid to liquid form which introduces a diameter correction of 4%. For this calculation, the density of copper in the liquid form (at 1083 °C) is $8.00 \times 10^{-15} \text{ kg}/\mu\text{m}^3$.⁴¹ The particle diameter D in flight is then:

$$D = 2 \left(\frac{3a\rho_s}{4\pi\rho_l} 2^b \pi^{-b/2} \right)^{1/3} A^{b/6} \quad 2-13$$

Figure 2.4 shows the flight diameter D , plotted versus the impact area A (Eq. 2-13) and the impact diameter D_i where a and b are 0.0628 and 2.828 respectively from the AFM data described above.

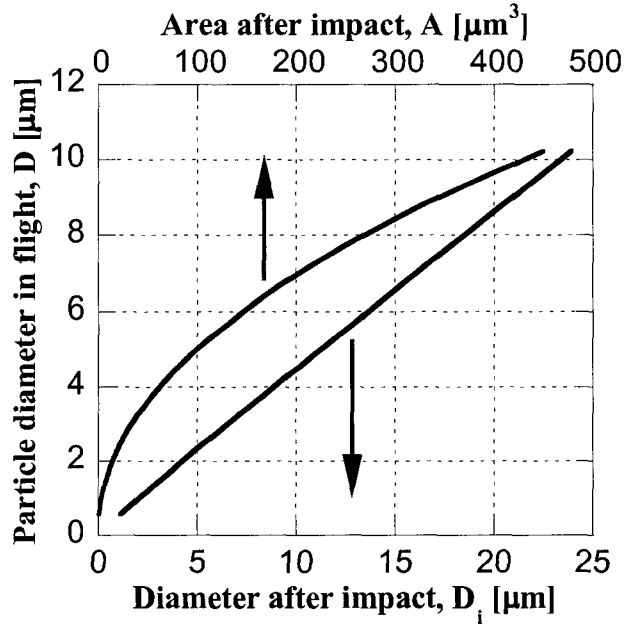


Figure 2.4 Relationship between the macroparticle diameter in flight, and the impact surface area and diameter of collected macroparticle on the witness plate

From Ref. 42, the density ρ_s of solid copper at 20°C is $8.93 \times 10^{-15} \text{ kg}/\mu\text{m}^3$ making the final mass as a function of impacted surface area:

$$M_p = \rho_s V_p = \rho_s a D_i^b = \rho_s a \left(\frac{4A}{\pi} \right)^{b/2} \quad 2-14$$

2.1.3 Macroparticle Charge

Combining the knowledge of the MP mass in Eq. 2-14 with the equation relating the MP charge to its displacement on the witness plate Eq. 2-11 above, we get a relation for the charge on the particle as a function of its transverse displacement s_0 from its original trajectory in meters, impacted surface area A in μm^2 , and velocity v_x in m/s:

$$q = 2 \frac{\rho_s d}{\ell^2 V_0} a \left(\frac{4}{\pi} \right)^{b/2} s_0 v_x^2 A^{b/2} \text{ coulombs} \quad 2-15$$

where the values of the coefficients a and b are 0.0628 and 2.828 respectively. This analysis is valid for the case where the charge on the macroparticle is constant throughout its flight in the electric field. As will be discussed in a later section, the charge of the particle is expected to vary during its flight due to thermionic emission. In order to determine the MP charge from the measured location on the witness plate, the initial temperature as well as an appropriate model for the MP charge must be known. If the rate at which the MP emits electrons is known, then the effect that the electric field has on the flight path of the MP is determined by integrating the equations of motion. A comparison of such an analysis with the "constant charge" expression is shown in Chapter 4.

2.2 Facility Description

The experiment is conducted in the University of Illinois Electric Propulsion Lab facility. The thruster operates in a 1 m diameter 1.5 m long chamber. The vacuum is maintained by a 1500 l/s Balzers TPH1500 turbomolecular vacuum pump. The turbo pump is backed by a 1180 l/s Roots blower, 614 l/s Roots blower, and two 71 l/s Kinney mechanical displacement pumps. The thruster begins operation at a vacuum of approximately 40-50 μ Torr. By the end of each experiment, the pressure has fallen to approximately 20 μ Torr. The pressure is measured by a Granville-Phillips model 270 ionization gauge, placed 15 cm above the turbo pump. The testing occurs approximately in the middle of the chamber, directly above the turbo pump, where the pressure is expected to be only a few μ Torr above the measured pressure. At these pressures, the mean free path of a nitrogen molecule is larger than the diameter of the chamber.

2.3 Apparatus

2.3.1 Vacuum Arc Source

The design of the vacuum arc for this experiment was based on the micro-vacuum arc thruster (μ VAT).¹ The μ VAT was designed to provide attitude control to micro and nano-satellites. It can be designed in a number of geometries including a coaxial, layered

sandwich, as well as a ring geometry. Due to its ease of construction, the sandwich or BLT geometry was used for this experiment. This geometry uses layers of flat sheets to comprise the different components of the thruster and was used on the UIUC CubeSat ION satellite. The first layer in this thruster is the cathode which is also the structure of the satellite. The cathode is separated from the anode by a ceramic insulator. This insulator is coated with a thin conductive film to help initiate the breakdown. Past the anode is another insulator separating it from an aluminum layer used to hold the layers together. Figure 2.5 is a CAD representation of this thruster.

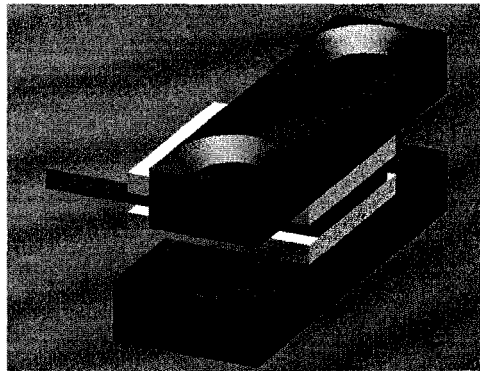


Figure 2.5 Schematic of the micro-vacuum arc thruster used on UIUC CubeSat ION

This thruster design is used with the small inductive power supply (Figure 1.1) described earlier, making it suitable for small satellites. However, the thruster performance is sensitive to the thickness of the thin conductive film coating the ceramic between the anode and the cathode. For this experiment, the design of the thruster was modified to include a trigger electrode. Figure 2.6 is a schematic of the front view of the thruster, showing the different layers listed.

- 1) Insulated structure (Kapton/Al.)
- 2) Insulating high alumina ceramic
- 3) Cathode (copper)
- 4) Alumina silicate ceramic
- 5) Trigger electrode (copper)
- 6) Insulating high alumina ceramic
- 7) Anode (aluminum)

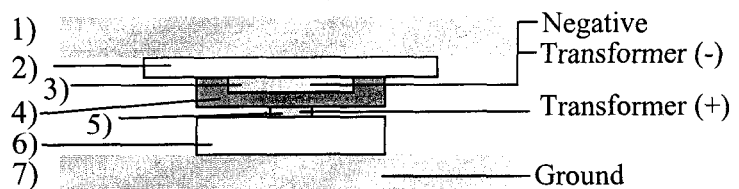


Figure 2.6 Front view of vacuum arc thruster used in this work

The power processing unit used in this lab vacuum arc source is different from the inductive energy storage circuit used in the flight model thruster. Instead of storing the discharge energy in an inductor, it is stored in an eight-stage pulse forming network (PFN).⁴³ With 3 μF capacitors charged to -600 V, and 30 μH inductors, the PFN is designed to deliver 100 amps for 150 μs . The designed current of 100 amps is intended to limit the number of cathode spots formed during a single pulse as described in Section 1.2.¹⁴ A resistance of 2 Ohms is placed in series with the discharge to match the impedance of the PFN. The typical current pulse is shown in Figure 2.7. The PFN is charged using a Converter Power Inc. Model RCS-3000, negative polarity power supply.

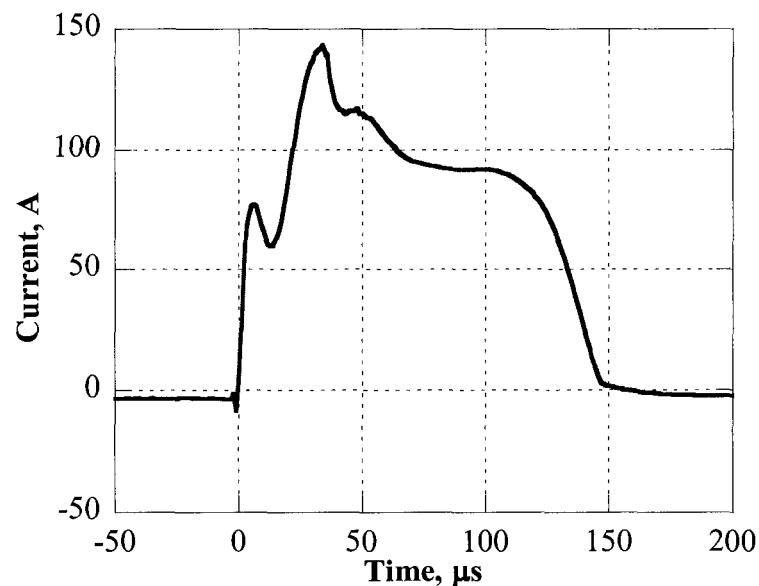


Figure 2.7 Current in the main discharge of the vacuum arc, pulse rate = 8.5 Hz

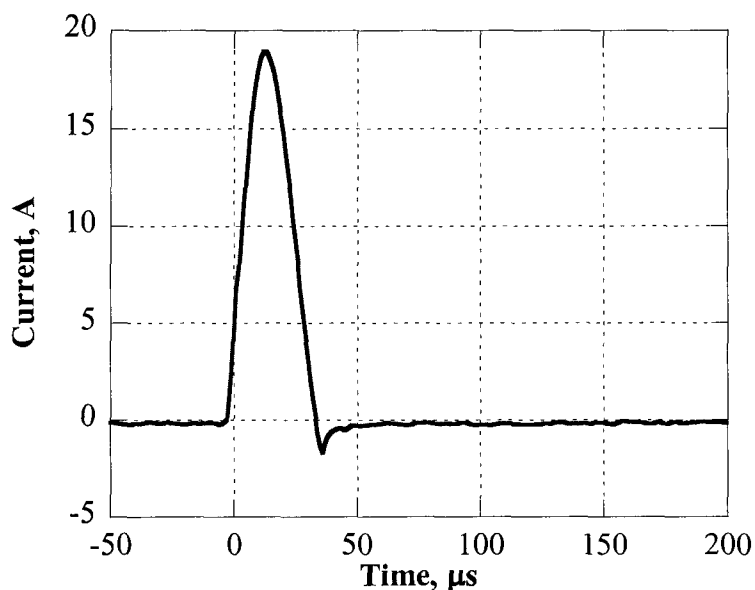


Figure 2.8 Current in the trigger pulse of the vacuum arc

The triggering pulse is generated by discharging a $9.2 \mu\text{F}$ mica capacitor through a $\sim 1:3$ transformer. With the capacitor charged to -600 V , the transformer secondary produces a 16.7 kV potential across an open circuit. This voltage is sufficient to initiate the breakdown between the trigger electrode and the cathode, producing a plasma to initiate the main discharge between the cathode and anode. Figure 2.8 shows the trigger pulse current. The trigger capacitor was charged using a Hipotronics model 803-5A power supply set to negative polarity. This setup is similar to the setup used by Brown et al. in Ref. 44. The trigger pulse is generated by a firing circuit which closes a silicon control rectifier (SCR) to send the current to the transformer.

The energy stored in the trigger circuit capacitor is approximately 35% that of the main discharge. It is uncertain what fraction of that energy is deposited into the trigger pulse, due to the presence of the transformer. It is possible that the trigger pulse also generates macroparticles. The design of this experiment did not distinguish between MPs generated from the trigger pulse and those generated from the main discharge.

According to Daalder,²² the angle at which macroparticles exit the cathode surface depends on the material. For copper, the angle at which the most macroparticles exit is between 5° and 15° from the cathode plane. For this reason, the vacuum arc source was tilted to an

angle of approximately 50° to the cathode normal, in order to increase the number of macroparticles emitted in the direction of interest. A smaller angle, which might further increase the number of macroparticles, would also increase the chance of arcing to the ground plane instead of the anode. This layout is shown in Figure 2.9

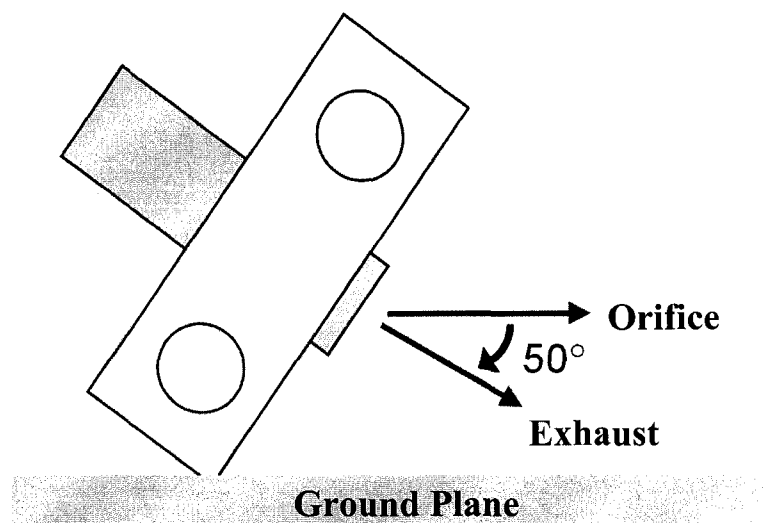


Figure 2.9 Side view of thruster showing thrust direction and location of orifice

2.3.2 Orifice and Deflection Plates

The double orifice assembly used in this experiment uses a pair of boron nitride plates. For the majority of the experiments, the first orifice is 0.53 mm in diameter, and the second is 0.51 mm, approximately 50 times the diameter of a $10\ \mu\text{m}$ particle. In order to reduce the width of the particle distribution due to the size of the orifice, one experiment was performed with a second orifice diameter of 0.37 mm. The orifice is fabricated by drilling into a $1/8$ " boron nitride plate, and using a $1/8$ " drill to countersink the hole to where the orifice depth is approximately 0.5 mm. Figure 2.10 and Figure 2.11 show a schematic of the orifice in the boron nitride plate, and photo of the plates respectively.

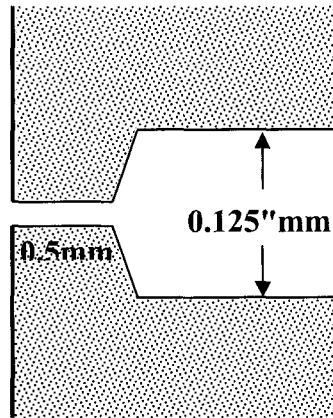


Figure 2.10 Schematic of the boron nitride orifice

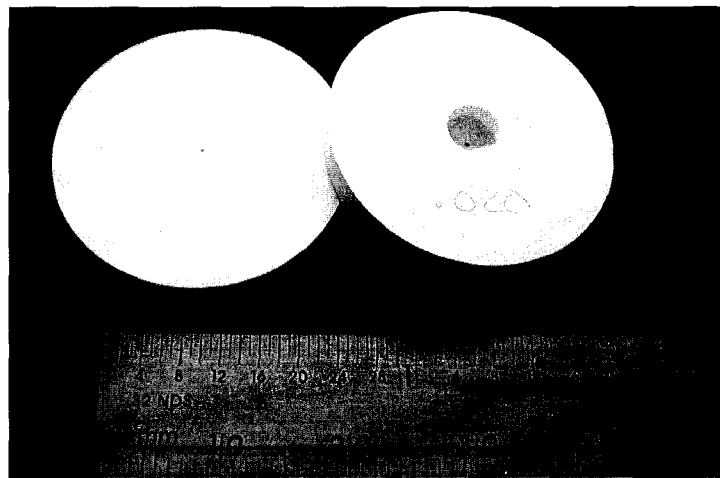


Figure 2.11 Picture of boron nitride orifices

The witness plate is a 20 mm tall by 30 mm wide section of a diced silicon wafer. The wafer used is a P-type Si:B wafer with a 5 – 25 ohm-cm resistivity. The wafer is cleaned first by acetone, using a lint-free wipe to remove any large particles or films. Then the witness plate is cleaned with isopropyl alcohol (IPA), de-ionized water, and again IPA. The witness plate is then dried either using dry nitrogen, or by slowly dragging a sheet of camera lens paper across the surface. This is done until all the IPA has evaporated, leaving no residue.

Due to the finite orifice diameter and the location of the witness plate with respect to the orifice, the distribution on the witness plate is expected to be larger than the width of the cathode. The width of the distribution on the witness plate (h_2), calculated by using Equation 2-9 for the primary and secondary setup listed in Table 2.1 are 1.9 mm and 1.2 mm

respectively. The primary setup, used in the majority of the experiments, uses an orifice diameter of 0.51 mm and cathode width of 0.8 mm. The secondary setup uses a smaller, 0.37 mm diameter orifice and 0.4 mm width cathode in a single test to reduce the particle distribution on the witness plate.

Table 2.1 List of variables (see Figure 2.2) used to calculate the width of the macroparticle distribution

	Description	Primary Setup [mm]	Secondary Setup [mm]
h_1	width of the cathode	0.8	0.4
l_1	distance from cathode to first orifice	90	90
s	distance between the orifices	19	19
l_2	distance from second orifice to the witness plate	116	116
d_1	diameter of first orifice	0.53	0.53
d_2	diameter of second orifice	0.51	0.37
h_2	width of the particle distribution on witness plate. "cathode image" (calculated)	1.9	1.2

The electric field used to deflect charged particles after they travel through the orifices is generated by charging two 98 x 25 mm parallel copper plates to opposite polarities. They are placed in a Delrin holder, to keep the plates from arcing to the ground plane above or below. The nominal voltage between the two plates (V_0) is 7000 volts, and the separation between the plates is 12.8 mm. This results in a nominal electric field of 5.5×10^5 V/m. Two separate power supplies were used to charge the electric field plates. The positive polarity plate used a Trion Inc Model 420733 power supply operating with a voltage divider. The negative polarity plate was charged with a Universal Voltronics Model BAP 32-5.5 power supply.

2.3.3 Witness Plate Mount

The tests to determine the location of the unperturbed particle distribution use a different witness plate than the tests where the deflecting electric field was present. In order to compare the location of the deflected particles with the location of particles that were not deflected, it is necessary to be able to compare the location of particles on different witness plates. To enable this, the witness plate mount is designed to position the witness plate

precisely between tests. The mount is designed so the right side of the witness plate contacts at only one point. This feature helps to ensure that the lateral location of the witness plate will be identical when it is replaced after removal. It also ensures that a measurement from the right edge (more specifically, from the location of the contact with the mount) on one witness plate will be comparable to measurements on a different witness plate. This reproducibility will be demonstrated in the results section.

2.3.4 Assembly

The thruster, velocity filter (described below), orifices, witness plate, and electric field plates are all placed onto a grounded aluminum plate. Once the electric field plates are aligned, another aluminum plate is attached on top of the experiment downstream of the orifices. This is to ensure a uniform electric field, without a potential gradient dominated by a single ground plane. This entire assembly, along with the transformer is placed into the vacuum tank. Figure 2.12 is an overall schematic of the thruster setup. Figure 2.13 shows a photo image of the setup without the velocity filters or deflecting electric field plates.

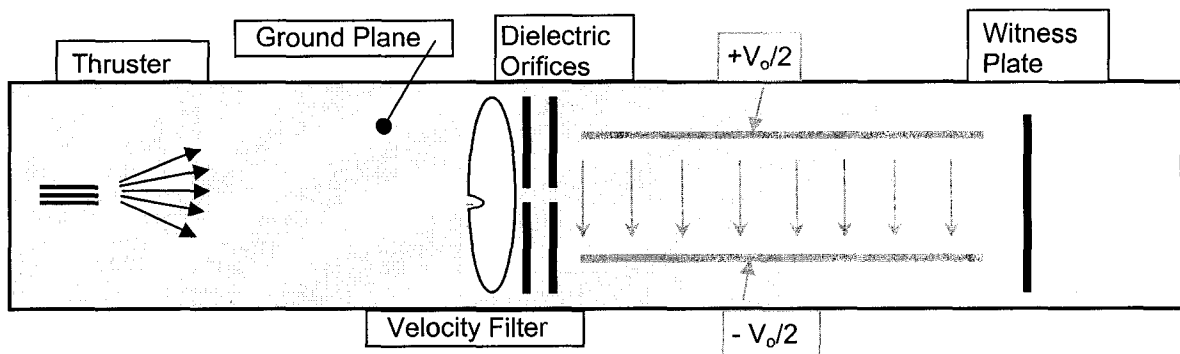


Figure 2.12 Schematic of the overall experimental setup (top-view)

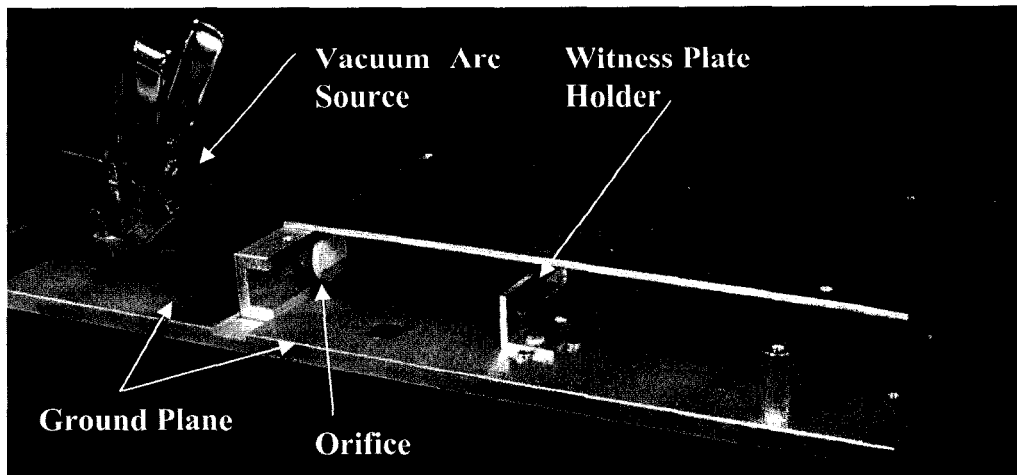


Figure 2.13 Photo image of experimental setup without velocity filter or deflecting electric field plates

2.3.5 Velocity Filter

The velocity of the macroparticles is determined by using a time-of-flight velocity filter to allow particles within a certain velocity range to reach the witness plate. The velocity filter operates by only allowing particles to pass through the filter and orifices during a short "window" of time after the $150\ \mu\text{s}$ current pulse. The velocities that are transmitted are primarily determined by the delay between the beginning of the arc current pulse and the opening window. This delay corresponds to the time of flight of the particle, and ranges from $400\ \mu\text{s}$ to $1100\ \mu\text{s}$. Particles traveling too fast will reach the velocity filter before the window is open, while particles traveling too slowly will arrive after the window has closed.

The velocity filter produces this window opening by blocking the entrance to the orifice with a spinning slotted disk. When the slot in the disk is in line with the entrance to the orifice, particles can proceed through the filter. By adjusting the spin rate, the width of the slot, and the time when the thruster is fired, the velocity of particles that will pass through the filter can be adjusted. Figure 2.14 shows a schematic view of the velocity filter setup. A typical "window" duration is $220\ \mu\text{s}$.

If all the particles were generated at one known time, then the velocity filter could be designed to allow all the particles traveling in a certain velocity range, and obstruct all those traveling faster or slower. However, if we assume the macroparticles are generated some

time during the 140 μs current pulse, particles traveling some velocities will only make it through the filter depending on when during the current pulse they were generated.

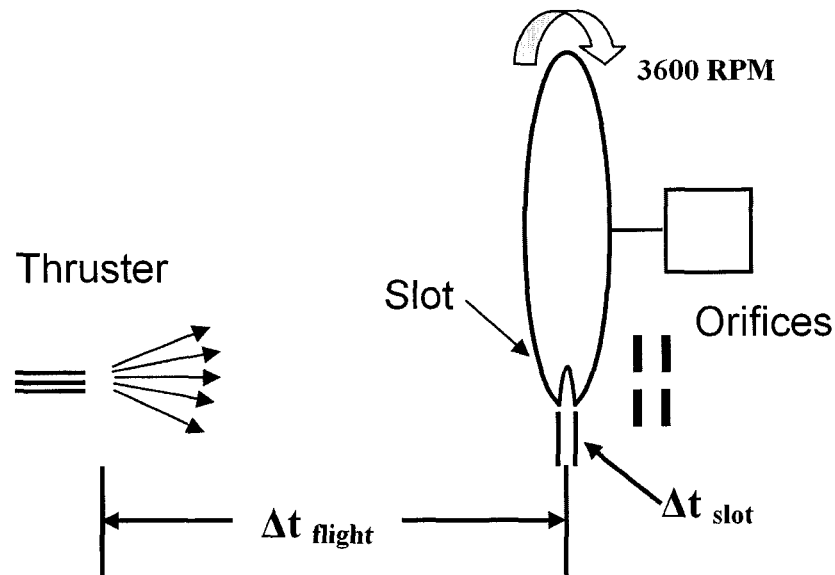


Figure 2.14 Schematic view of the velocity filter setup and operation

If we know the probability distribution of generating a macroparticle throughout the pulse, then we can calculate the percentage of particles (of a particular velocity) that are transmitted through the velocity filter. For any given velocity, the percentage of particles that will make it through the filter is equal to the percentage probability that the particle was generated at a time during the pulse, when it will reach the filter during that opening window. Figure 2.15 shows the fraction of particles that will make it through the velocity filter for four different delay times Δt_{flight} between the current pulse and the opening window. The figure assumes that the probability distribution of generating a macroparticle throughout the pulse is constant and is based on the characteristics in Table 2.2. Table 2.3 shows a summary of the information described in Figure 2.15.

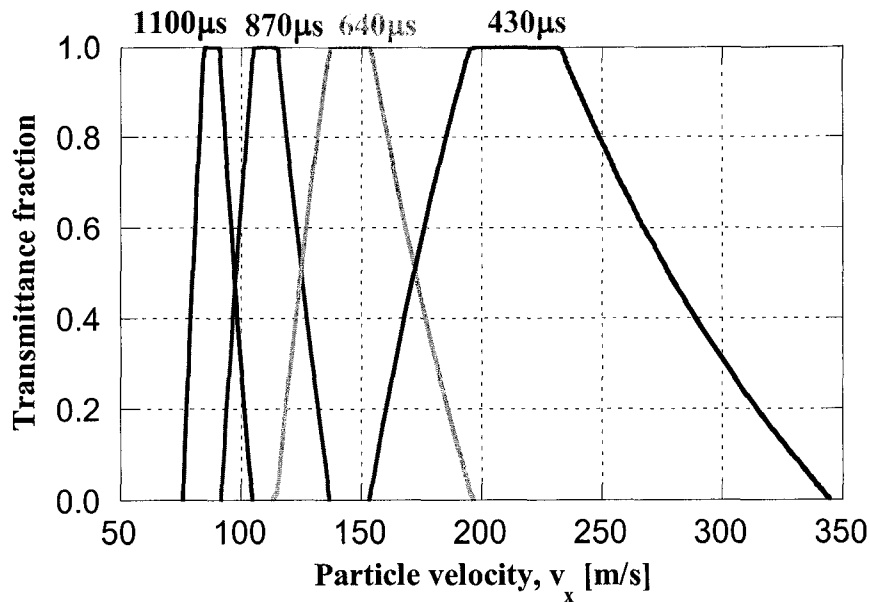


Figure 2.15 Fraction of particles allowed through the velocity filter, plotted for delay times 1100, 870, 640, and 430 μs

Table 2.2 Physical characteristics of velocity filter

spin rate	3600 rpm
radial location on disk of orifice	46.8 mm
slot width	3.92 mm
pulse width	140 μs
distance from arc to the velocity filter	100 mm

Table 2.3 Performance characteristics of the velocity filter used

delay time [μs]	1100	870	650	430
velocity [m/s]	88	110	145	214
negative error [m/s]	-8	-12	-20	-42
positive error [m/s]	+9	+15	+27	+63

The timing of the velocity filter is achieved by using a light and sensor pair to sense the location of the slot as it passes a point in its rotation. Once the slot passes the sensor, a timing pulse is triggered, which sends a second delayed pulse to the arc firing circuit to initiate the vacuum arc. The delay time listed in Table 2.3 and Figure 2.15 is the amount of time between the end of the timing pulse and the time when the slot reaches the orifice. This is also the flight time of the MP from the thruster to the orifice, for particles traveling at the velocity listed. Appendix A describes the timing circuit.

The motor and disk used in the velocity filter are recycled from a computer hard drive. The hard drive platter was machined with three slots for stability while spinning. The location of the light/sensor pair is directly opposite the orifice. If two slots were machined into the disk, the thruster would fire at the same time that the sensor received a signal. This is undesirable because the electromagnetic interference from the vacuum arc affects the sensor. Figure 2.16 shows a picture of a typical 95.3 mm diameter velocity filter disk used during the experiments.

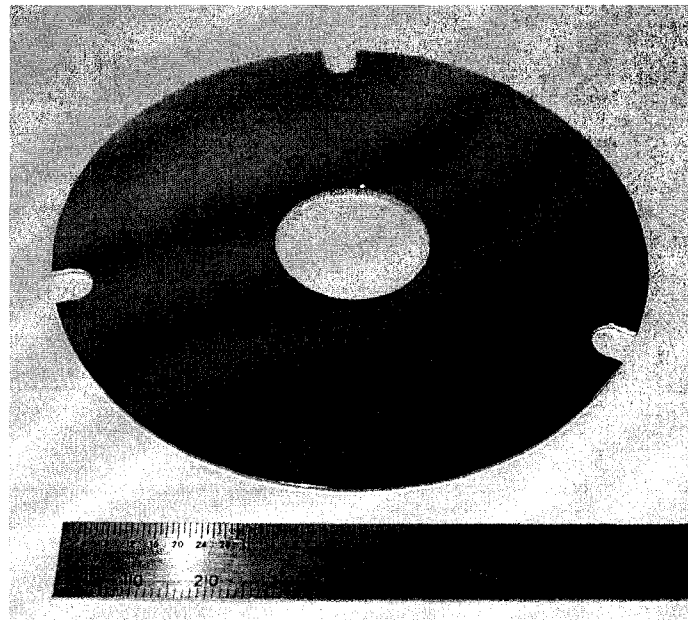


Figure 2.16 Typical disk used in the velocity filter

A hard drive motor is typically a variable reluctance stepper motor. Some hard drive stepper motors require 12 pulses per revolution (ppr), while others operate at 18 ppr. Initially a circuit was designed to control the hard drive motors. This circuit could operate the motor at a variable spin rate, but due to limitations in design, the repeatability of the spin rate was very limited. To alleviate this problem, the controller card from a Maxtor hard drive was used during the experiment. This controller card was designed to operate at 5400 RPM with a 12 ppr. The reason this controller card was used is because no extra electronics are necessary for the controller to spin the motor. The motor used is an 18 ppr motor from an IBM hard drive. This combination of motor and controller results in a spin rate of 3600 RPM. When the vacuum arc source is not pulsing, the rotation rate of the motor is extremely precise. The rotation rate of the disk is 3600 ± 0.3 RPM. However, the electrical

noise generated during the arc discharge reduces the precision of the motor to 3600 ± 10 RPM. This uncertainty

2.4 Scanning Electron Microscope Results

A single test consists of firing the vacuum arc source at approximately 8 Hz for 200,000 shots. After some preliminary tests were performed to verify the repeatability of the alignment of the setup, four tests were performed to measure the charge on macroparticles of different velocities. Each of these tests corresponds to the velocities listed in Table 2.3. After these four tests, one final test was performed to reduce the error bars of the results by reducing the undeflected particle distribution width.

2.4.1 Macroparticle Shape on Witness Plate

After the test, the witness plate was removed from the experimental setup, and the macroparticles were observed using a JEOL model 6060 scanning electron microscope. Figure 2.17 thru Figure 2.19 show some high resolution images of the macroparticles collected on the witness plate showing a wide range of macroparticles sizes. Particle "a" in Figure 2.17 (shown close up in Figure 2.18) is approximately $16 \mu\text{m}$ in diameter (D_i), while some of the smaller MPs such as "g" and "h" have a diameter less than $1 \mu\text{m}$. Table 2.4 shows a summary of the diameters of some of the larger MPs shown in Figure 2.17. Typical macroparticle cross-sections are shown in Section 2.5.

Table 2.4 List of particle diameters in Figure 2.17

Particle	Diameter D_i in μm
a	16
b	8.5
c	4.0
d	3.8
e	1.6
f	1.0
g	0.8
h	0.5

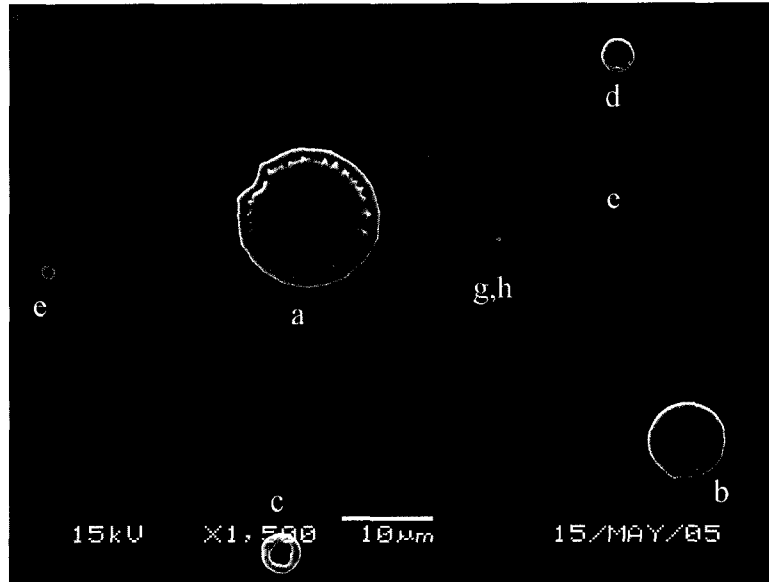


Figure 2.17 Moderate magnification of macroparticles on a silicon wafer witness plate showing a wide range of MP sizes

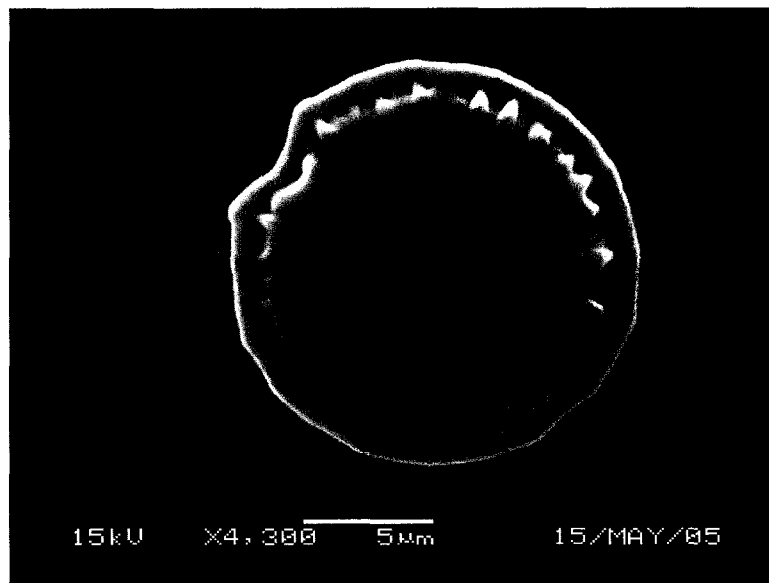


Figure 2.18 High magnification image of a relatively large macroparticle "a" from Figure 2.17

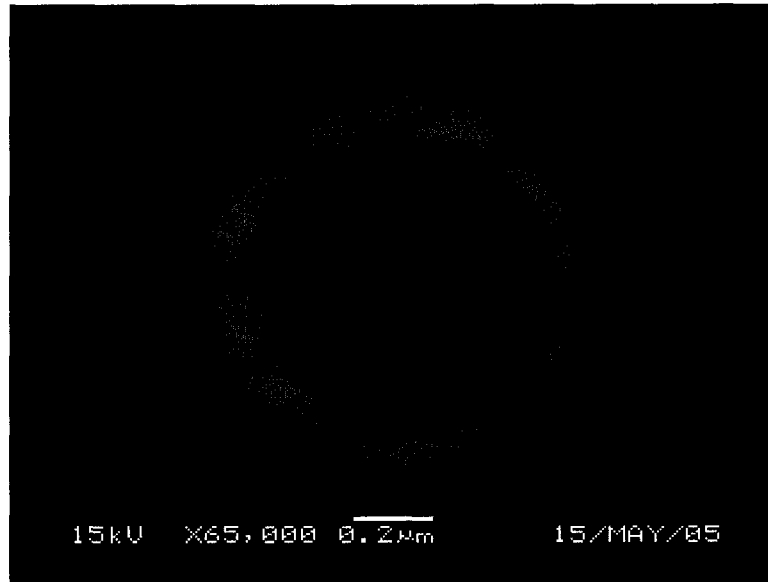


Figure 2.19 Very high magnification of a 1 μm diameter macroparticle

The shape of the macroparticles in the SEM images is consistent with the premise that the macroparticles are in the form of molten metal droplets when they impact the witness plate. The vast majority of the impacted macroparticles and almost all of the particles with a diameter less than 5 μm have the shape of a flattened torus with a thin layer of material in the middle as shown in Figure 2.19. However, the shape of the larger particles appears to vary slightly. For example, particle "b" in the bottom right of Figure 2.17 appears to have the typical shape. Particle "a", the dominant particle in the center of the image appears to have a height profile where the peak is not at the outside diameter. Finally, particle "c" at the bottom of the image has the shape of a torus, but the aspect ratio, or thickness of the toroid to the diameter appears larger than the majority of the macroparticles. We hypothesize that this variation is due to a combination of particle velocity and temperature at impact.

2.4.2 Data Reduction

After each test, the witness plates were scanned at 200x magnification. In order to aid in finding the MPs, the SEM was operated in back-scattered electron mode. This mode shows a high contrast between the low molecular weight of the background Si (28) and the Cu (63.5).

Approximately 220 images were taken for each test over an area approximately 10 mm x 4 mm on the witness plate. These images were stitched together using a stitching program called Panorama Factory.⁴⁵ Each image taken is 0.500 mm offset from the previous image. The field of view on each image is 0.640 mm across, resulting in an overlap of 0.140 mm or 280 pixels.

Before the particles can be counted in the final image, the image must be converted to black and white from the 256 shades of gray. This is done by choosing a threshold level where all the lighter pixels become white, and all the darker pixels become black. This threshold level is chosen manually by increasing the level until only the particles, and not the background noise appear white. In some cases, this threshold level also has the effect of artificially changing the particle size. If the shade of the pixels on the edge of a particle is near the threshold level, that pixel may or may not be counted toward the size of the particle depending on the threshold level. For this reason care was taken to consistently choose a threshold which is just above the level where the background noise is eliminated.

Once the image is converted to black and white, a software package called ImageJ⁴⁶ is used to determine the location and pixel count of each particle. The x location is then used to determine the particle displacement from its initial trajectory, and the pixel count is used to determine the diameter of the impacted particle.

The particle displacement from its initial trajectory s_0 is determined by measuring the distance between the x-location of the particle and the center of the unperturbed particle distribution. To determine the center of the unperturbed particle distribution, a separate test is conducted with no deflecting electric field. After this test, the distance from the distribution center and the witness plate edge is measured. That distance is then used to locate the undisturbed distribution center for the experiments with an electric field. The witness plate edge is used to align the witness plate on the holder, so the location of the center of distribution is the same for each witness plate.

The pixel count corresponds to the surface area of the particle on the witness plate. By assuming that the macroparticles are circular on the witness plate, the surface area is

converted into a particle impact diameter D_i by using the equation for the area of a circle. The flight diameter, mass, and charge are then calculated according to Eq. 2-13 thru 2-15.

2.5 Atomic Force Microscopy Results

In order to correlate the impact diameter of the macroparticle to a flight diameter, particle height profiles were taken using an Asylum MFP-3D AFM. Figure 2.20 thru Figure 2.23 show 3D representations of the particles after impact with the witness plate along with cross-sections of each particle. The figures show the wide range of MP shapes measured by the AFM. The diameter of the particles measured range from 0.3 to 40 μm . An Asylum particle measurement package⁴⁰ was used to calculate the volume of 36 particles to within an estimated accuracy of 1% - 2%. The volume of the particles measured range from 0.002 μm^3 to 2700 μm^3 . Figure 2.24 on page 38 shows the measured particle volume V_p plotted versus the impacted particle diameter D_i , along with the curve fit used in the data reduction. The plot also includes the curve fit of the work done by Daalder in 1976.

The measured volume for the current work is lower by 30 to 70% for a given particle diameter than the results of Daalder's work in 1976. There are a number of possible reasons for the difference between the results. First, the particles in the current system travel farther and through a lower vacuum (higher pressure) than in Daalder's work. Because the temperature of the MPs decreases during the flight, this could have resulted in a lower temperature during impact

Also, the witness plates used by Daalder were made of stainless steel instead of the silicon wafer used in the current work. This could have resulted in a different particle shape due not only to the interaction between the copper and witness plate material, but also due to the different values of thermal conductivity. The thermal conductivity of silicon and stainless steel are 150 and 16 W/mK respectively, significantly less than 385 W/mK for copper. Heat transfer from the MP to the witness plate as the MP impacts is a complicated phenomenon. As the MP impacts, the size of the interface is increasing and the temperature of the MP is changing as it cools. This results in a complicated calculation for the heat conduction to the witness plate which will not be solved in this work.

Finally, the MPs measured in this work have a peak z-axis height ranging from 0.6 μm for the largest particles to less than 0.1 μm . Daalder's work determined the particle volumes by using an optical microscope designed to measure z-axis height of a sample.⁴⁷ The resolution of this instrument which is limited by optics to be no better than 0.5 μm , is far surpassed by the more modern AFM technology used in this work. Where Daalder measured the height of two points on the macroparticle and calculated a volume based on that measurement, the AFM gives on the order of 1×10^6 height measurements with sub nanometer height resolution. Daalder's work may simply have resulted in an overestimation of the volume due to the limited resolution of data available.

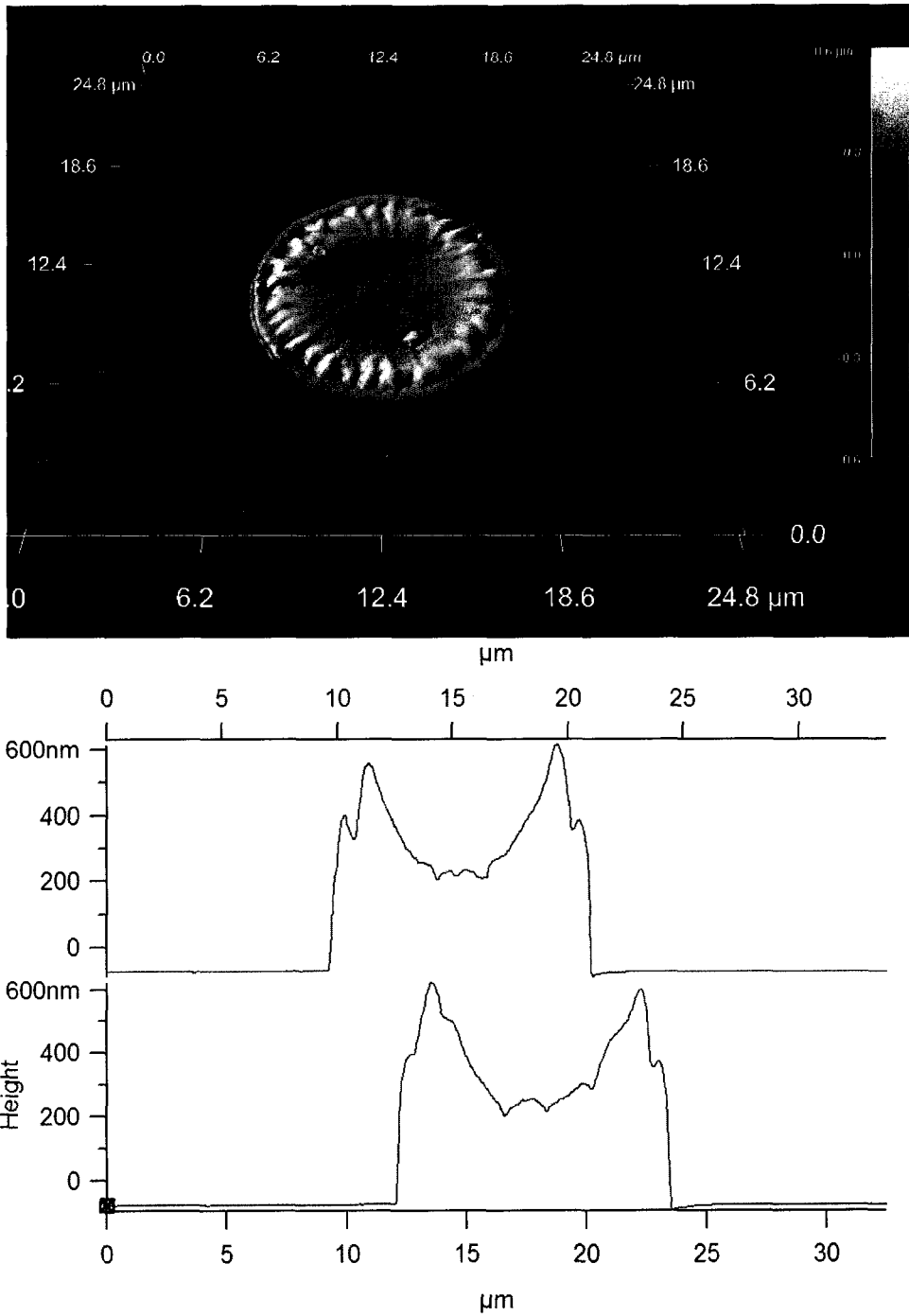


Figure 2.20 AFM 3D image representation of an 11.5 μm diameter macroparticle along with two cross-section height profiles

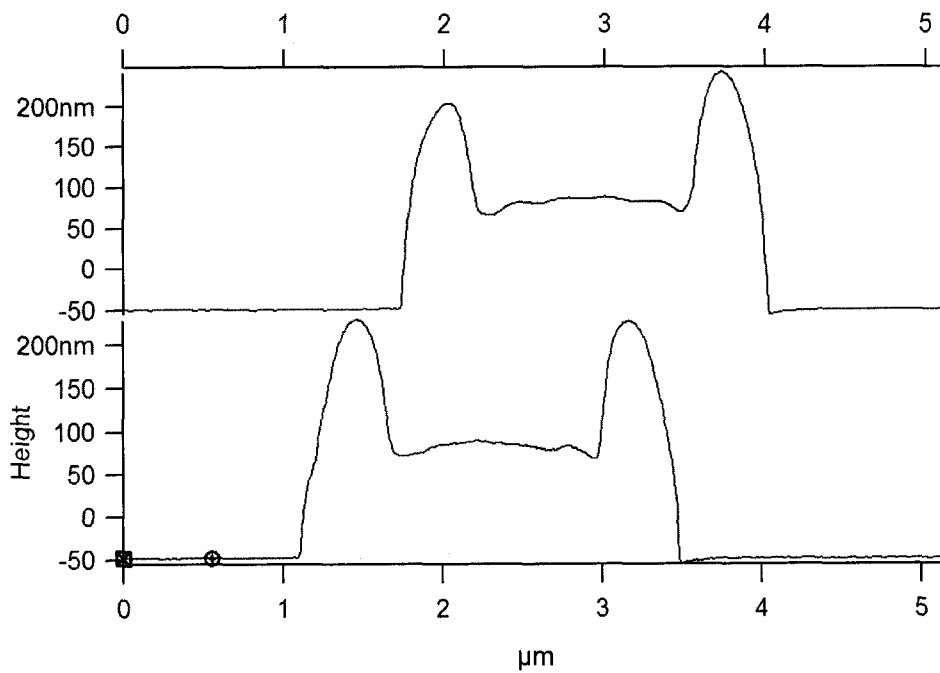
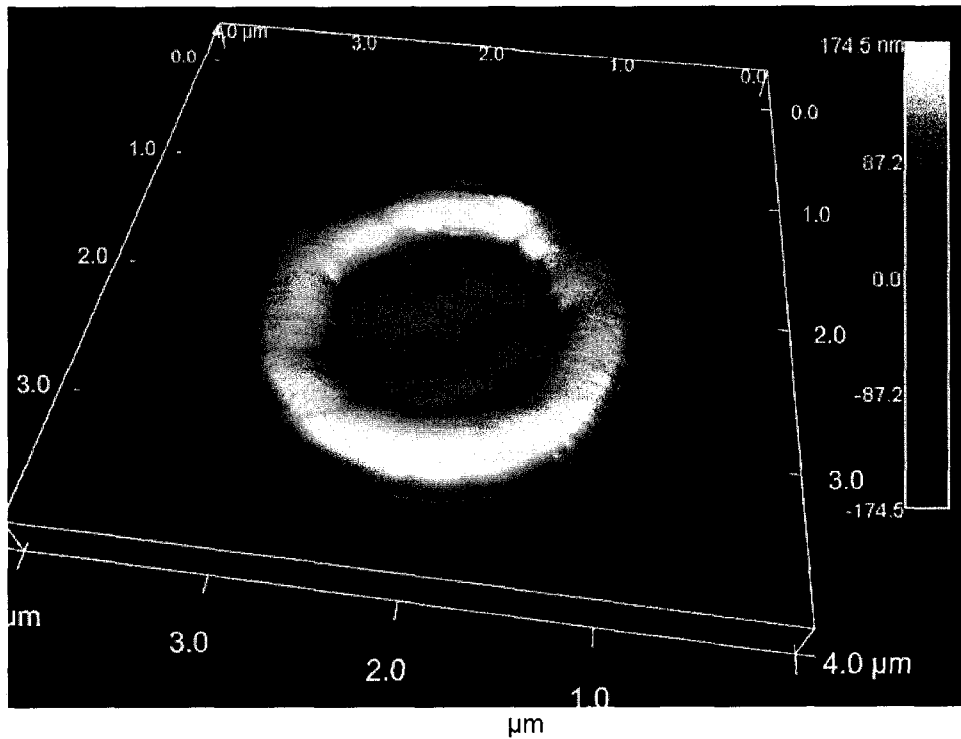


Figure 2.21 AFM 3D image representation of a 2.36 μm diameter macroparticle along with two cross-section height profiles

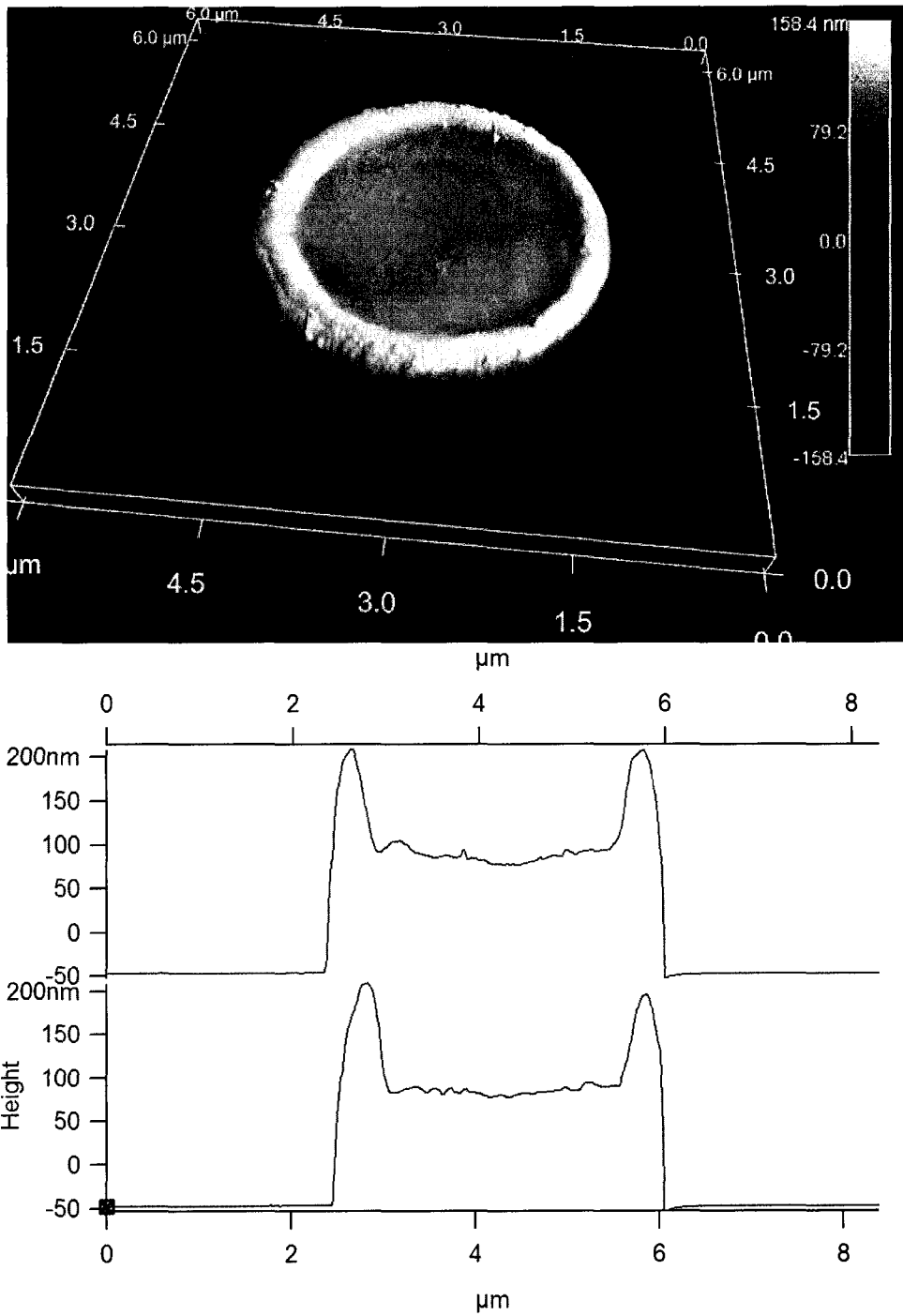


Figure 2.22 AFM 3D image representation of a 3.65 μm diameter macroparticle along with two cross-section height profiles

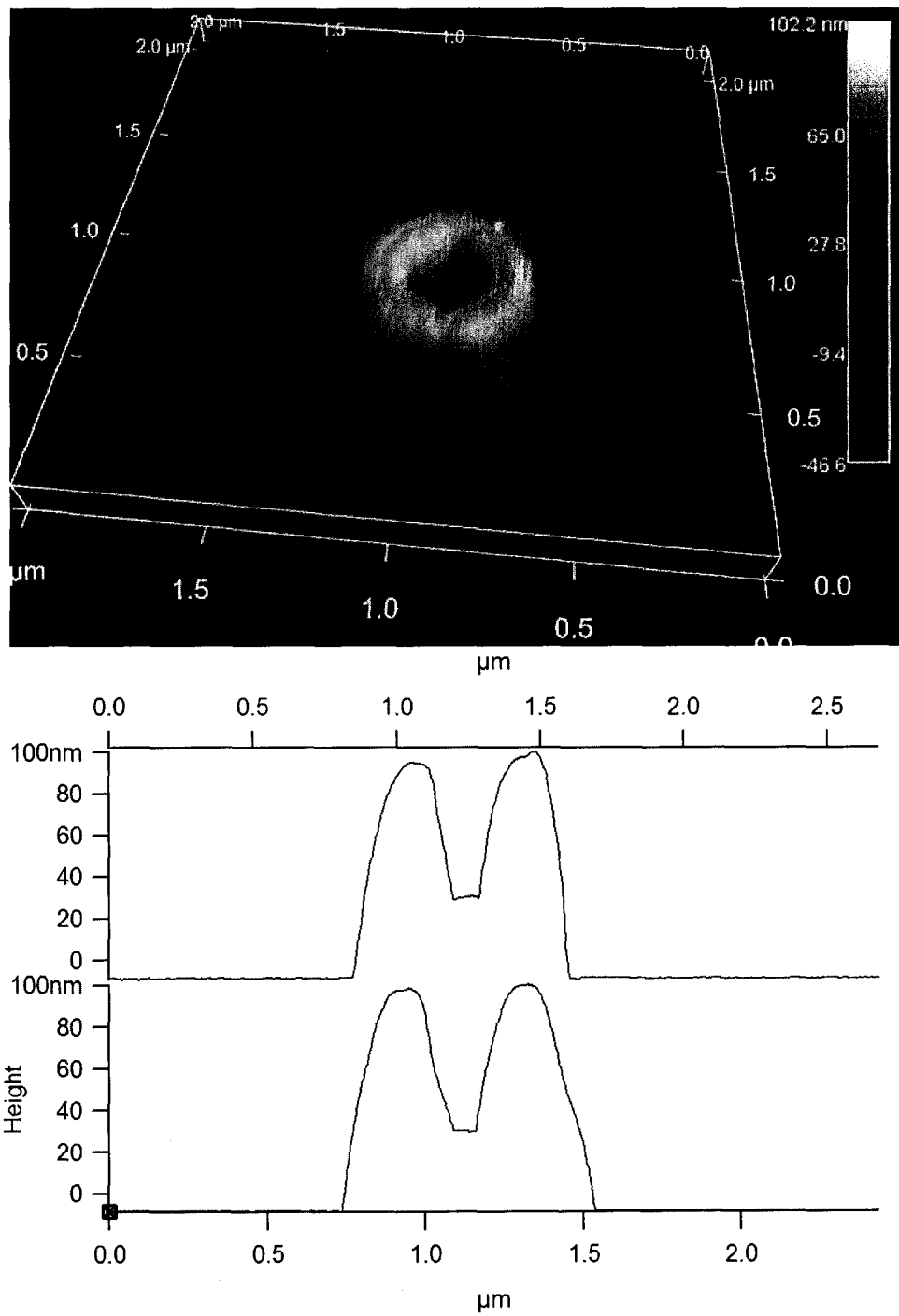


Figure 2.23 AFM 3D image representation of a 0.78 μm diameter macroparticle along with two cross-section height profiles

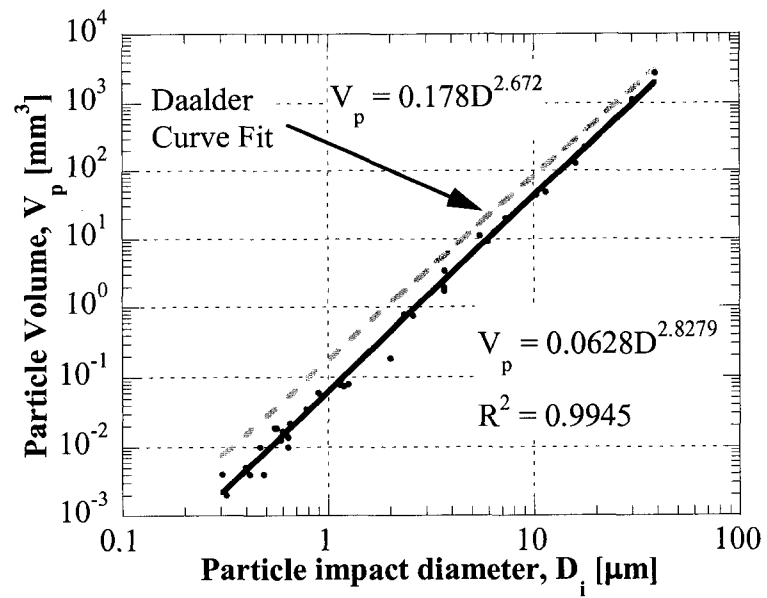


Figure 2.24 Particle volume measured using an atomic force microscope, plotted versus the particle impact diameter

Chapter 3

Experimental Results

Before tests could be run to measure the charge on ejected macroparticle using the experiment design described in Chapter 2, first the witness plate alignment is verified. This is done for the 0.37 mm and 0.51 mm diameter orifice configuration. Once it is verified that the placement of the witness plate is repeatable, and the location of the un-deflected particle distribution is located on the witness plate, then tests to measure the particle deflection and calculate the charge are run. The deflection and charge of each collected MP is plotted and a relation between the charge and particle diameter is determined.

3.1 Witness Plate Alignment

To verify the repeatability of the setup alignment, as well as determine the location of the un-deflected particle distribution, some preliminary tests were run. First, two tests collected particles without the use of the velocity filter or deflecting electric field, using the 0.51 mm diameter orifice and 0.8 mm cathode width configuration listed in Table 2.1. The same witness plate was used for both tests, in order to compare directly the location of particles. Figure 3.1 shows the location of particles collected during the two tests. The width of the distribution is slightly less than the 1.9 mm width expected from the geometry. Not only are the two particle distributions approximately the same width as the calculated width from the geometry, they are also centered on the same z-location, indicating that the method used to align the witness plates is repeatable. The height of the distribution extends above and below the plot. Due to time limitation on the SEM, images of the entire particle distribution were not taken. The portion shown corresponds to the highest particle density of the whole distribution. Note that the particle size is not represented in this figure.

Figure 3.2 shows a histogram of the particle locations using 0.05 mm "bins". The figure shows that the width of the actual particle distribution is slightly smaller than the calculated 1.9 mm width. One possible reason for this is the fact that particles traveling through the orifice cannot come closer to the orifice wall than one particle radius. However, for a 10 μm diameter particle, this reduces the size of the calculated particle distribution width by 0.02

mm which does not account for the total discrepancy between the actual and calculated particle width. The precise reason for this discrepancy is not known, however it is possible that macroparticles simply did not form as often near the edges of the cathode face. Because the particle distribution is an image of the cathode face, this would result in a smaller particle distribution.

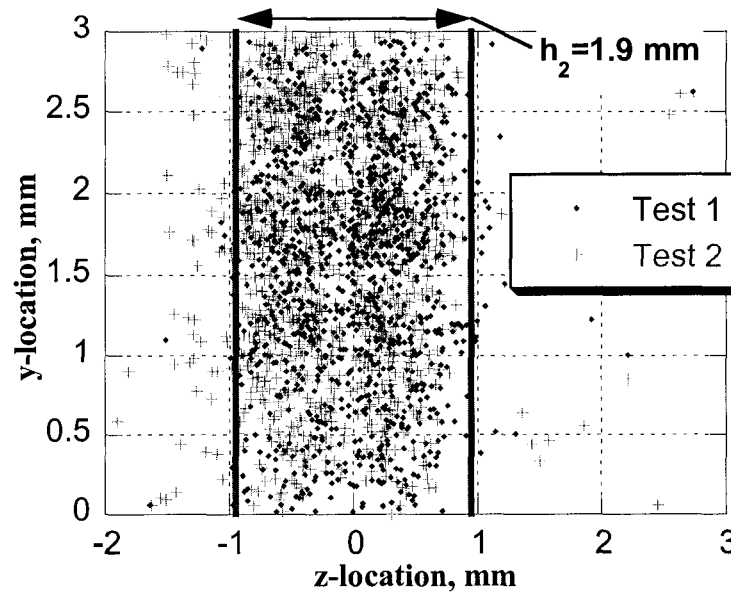


Figure 3.1 Collected particle distribution without an electric field or velocity filter for two tests using the 0.51 mm orifice

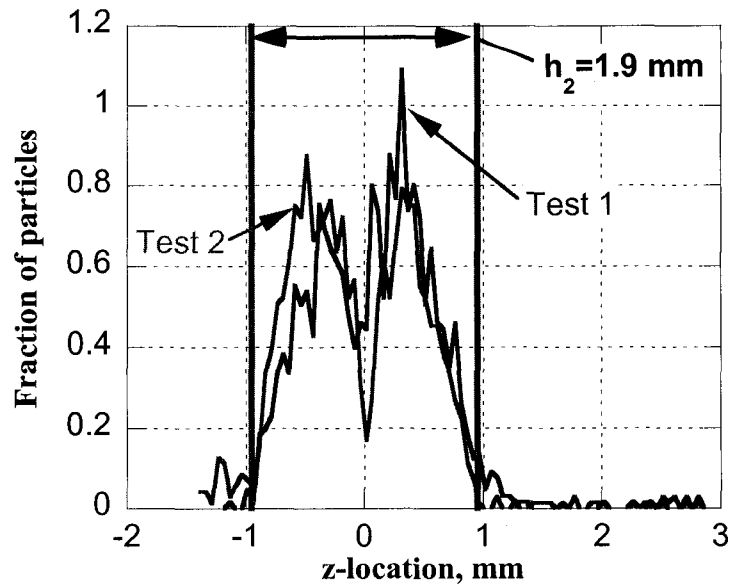


Figure 3.2 Number density of particles normalized by the total number of collected particles versus the z-location, along with the calculated particle distribution width based on the 0.51 mm orifice geometry

From the data in Figure 3.1, it is possible to determine the diameter of macroparticles that account for the majority of the mass ejected from the vacuum arc. Figure 3.3 shows the fraction of mass in the form of macroparticles that are larger than a given particle diameter D^* , plotted versus D^* . This figure shows that even though there are fewer large particles, their mass accounts for a significant fraction of the total mass lost due to MPs.

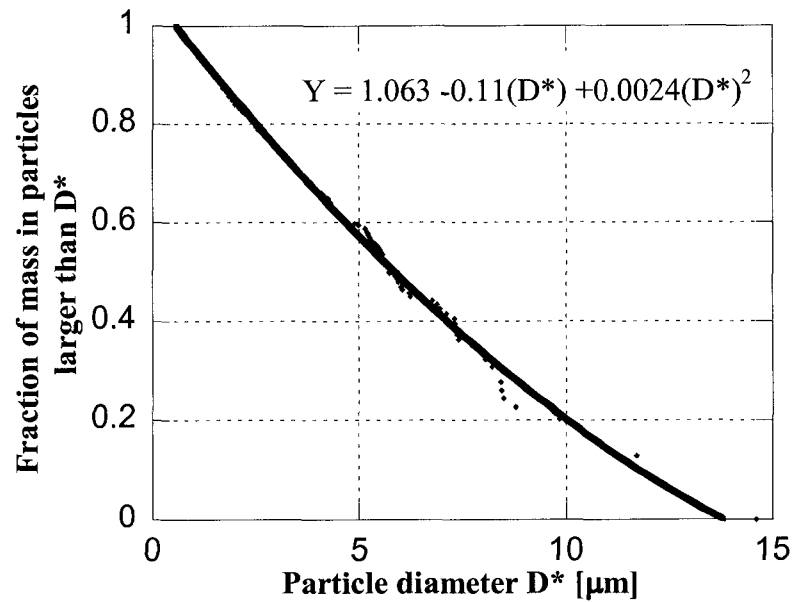


Figure 3.3 Fraction of mass in the form of particles that are larger than a particle diameter D^* , plotted versus D^*

The location of the center of the distribution in Figure 3.1 is measure to be 9.30 mm from the edge of the witness plate. This number is used to determine the location of particles relative to their initial trajectory. Figure 3.4 shows a schematic of the location of the particle distribution relative to the witness plate wall. Recall that the witness plate mount is designed to contact the witness plate at one point on the right edge.

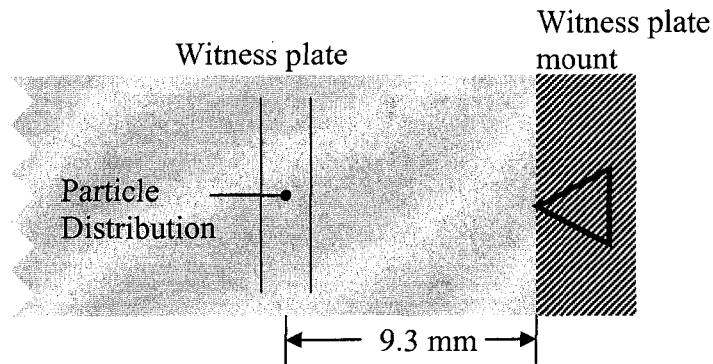


Figure 3.4 Schematic showing the relative location of the un-deflected particle distribution

This geometry with the orifice diameter of 0.51 mm was used on all succeeding tests, except for a final test. In that test, a smaller 0.37 mm diameter orifice and 0.4 mm cathode were

used in order to reduce the width of the un-deflected distribution, thus reducing the error bars on the results. Figure 3.5 shows the size of the un-deflected particle distribution for the 0.37 mm orifice setup, along with the calculated width of 1.2 mm. Figure 3.6 shows a histogram of this distribution using 0.05 mm sections. The width of the un-deflected particle distribution is approximately equal to the 1.2 mm calculated value. The center of this distribution is measured to be 8.98 mm from the edge of the witness plate.

The total height of the cathode in this test is approximately 6.3 mm. Because the thruster is tilted by 50°, the image of the cathode on the witness plate is only 4.1 mm high. However, because of the finite orifice diameter, the resulting particle distribution on the witness plate is expected to be 5.1 mm high. In this test, the SEM images span a height of 4.4 mm which is almost the entire calculated distribution height. This is seen in Figure 3.5 as there are significantly fewer particles on the top and bottom of the distribution.

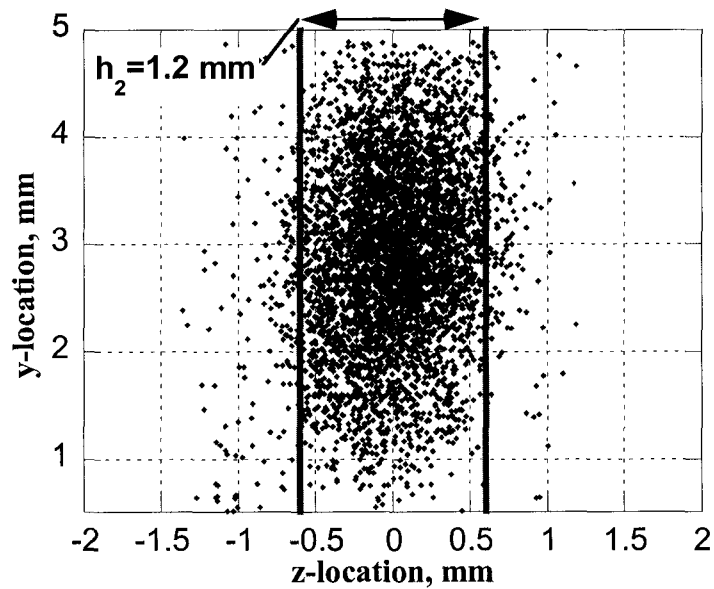


Figure 3.5 Collected particle distribution without an electric field or velocity filter for the secondary configuration

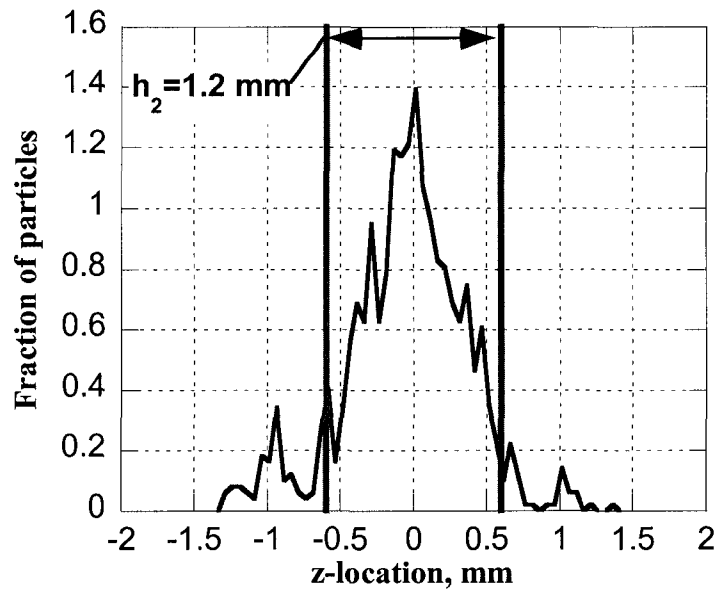


Figure 3.6 Number density of particles normalized by the total number of collected particles versus the z-location, along with the calculated particle distribution width based on the 0.37 mm orifice geometry

3.2 Results

Four primary tests were performed with the velocity filter, as well as the deflecting electric field. For each of these tests, an electric field of 5.5×10^5 V/m was used to deflect the particles. One secondary test in addition to the four primary tests was run with a 0.37 mm diameter orifice and 0.4 mm width cathode (see Table 2.1). Figure 3.7 thru Figure 3.11 show the size distribution of the particles plotted versus the z-displacement on the witness plate s_0 for the four macroparticle velocities tested. The vertical lines are separated by 1.9 mm for the primary setup (first four plots) and 1.3 mm for the secondary setup (last plot) and indicate the location of the particle distribution if no electric field were used. Each test was performed with the velocity filter set to allow a different range of velocities through. Note that the electric field is positive in the direction of the arrow.

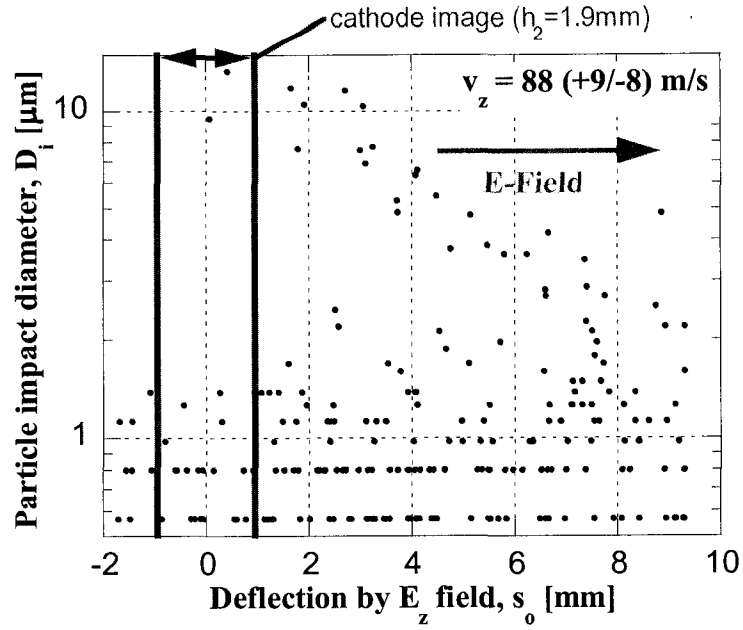


Figure 3.7 Particle impact diameter versus displacement from original trajectory for particles traveling 88 m/s

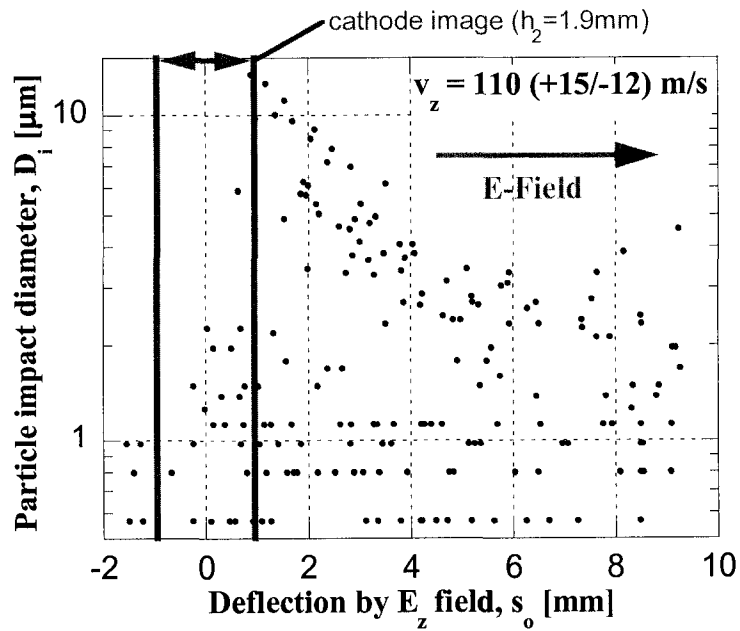


Figure 3.8 Particle impact diameter versus displacement from original trajectory for particles traveling 110 m/s

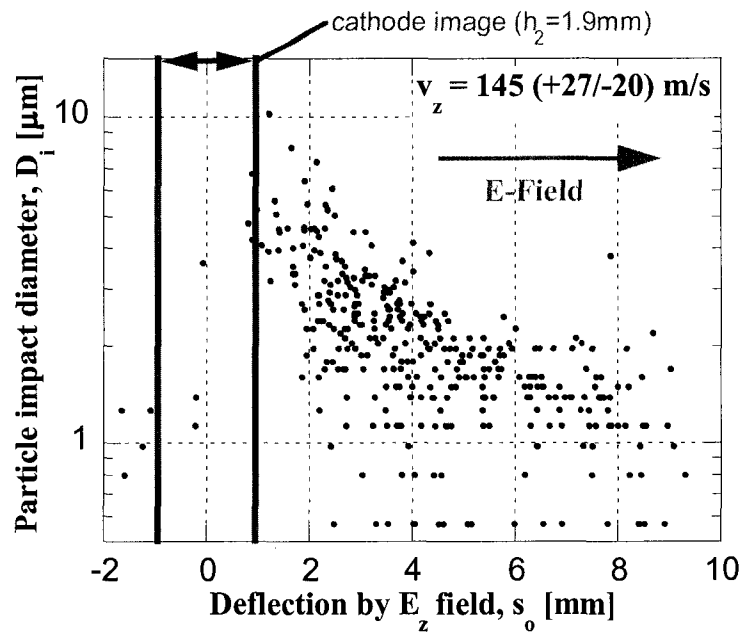


Figure 3.9 Particle impact diameter versus displacement from original trajectory for particles traveling 145 m/s

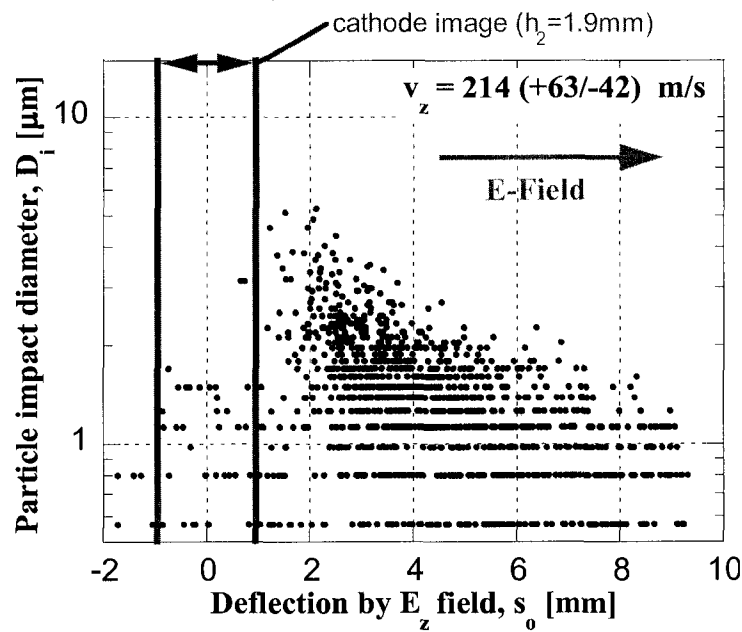


Figure 3.10 Particle impact diameter versus displacement from original trajectory for particles traveling 214 m/s

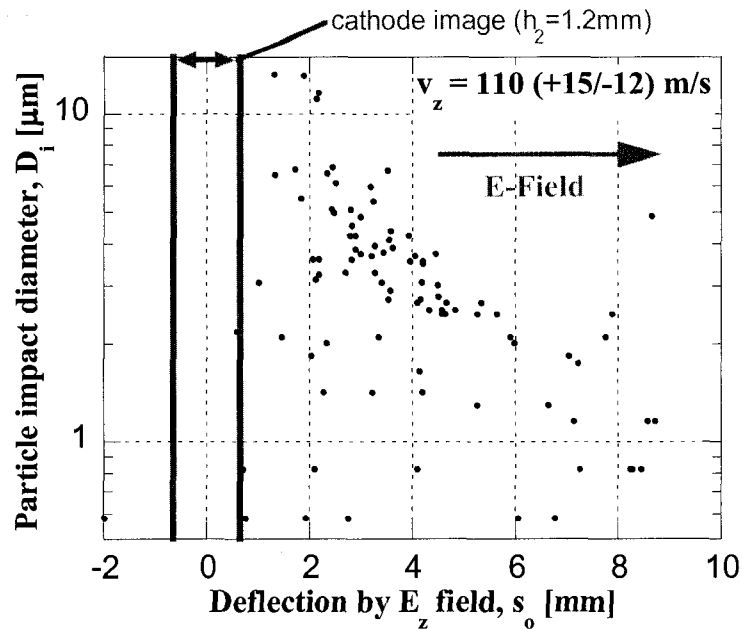


Figure 3.11 Particle impact diameter versus displacement from original trajectory for particles traveling 110 m/s, using the secondary geometry

The plots clearly show that the particles collected on the witness plates have a positive charge and are deflected by the electric field. The plots also show that the larger particles were deflected less than the smaller particles. The particle impact diameter D_i is calculated from the number of pixels that represent the particle in the SEM image. For small particles, each pixel represents a significant fraction of the particle area. Because each pixel represents a discrete particle area, the difference in impact diameter between particles with a one pixel difference is relatively large for small particles. This can be seen for particle diameters D_i less than approximately $1.5 \mu\text{m}$. In order to count the particles using the analysis software, the image has to be converted into black and white. This process introduces an error in the determination of the size of the impacted particles. For this reason, particles less than 6 pixels ($1.25 \mu\text{m}^2$), have relatively large error bars associated with them.

Using Eq. 2-15, the charge on each of the collected macroparticles is calculated and plotted in Figure 3.12 thru Figure 3.16. The displacement s_o is the distance between the location of the particle on the witness plate and the midway point of the unperturbed particle distribution. The electric field used during the tests is $5.5 \times 10^5 \text{ V/m}$ for the primary setup,

and 5.7×10^5 V/m for secondary setup. The length of the electric field region ℓ is 0.098 m. A quadratic curve fit of the form $q=C_2D^2+C_1D+C_0$ has been used to show the trends of the data. Along with the calculated charge, the figures show a line on the log-log plot with a slope of 2.0 or $q \sim D^2$ for comparison.

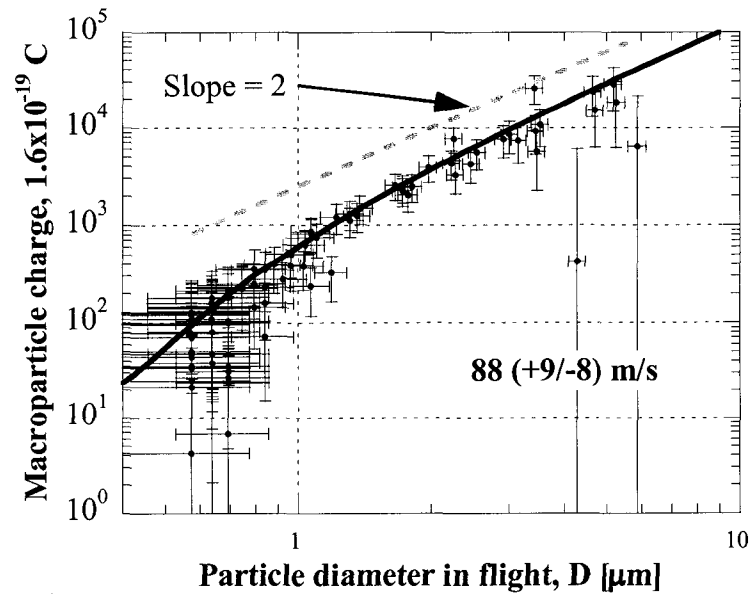


Figure 3.12 Accumulated macroparticle charge, plotted versus the particle diameter in flight for particles traveling 88 m/s, along with curve fit of the form $q=C_2D^2+C_1D+C_0$. Test performed using 0.51 mm orifice configuration

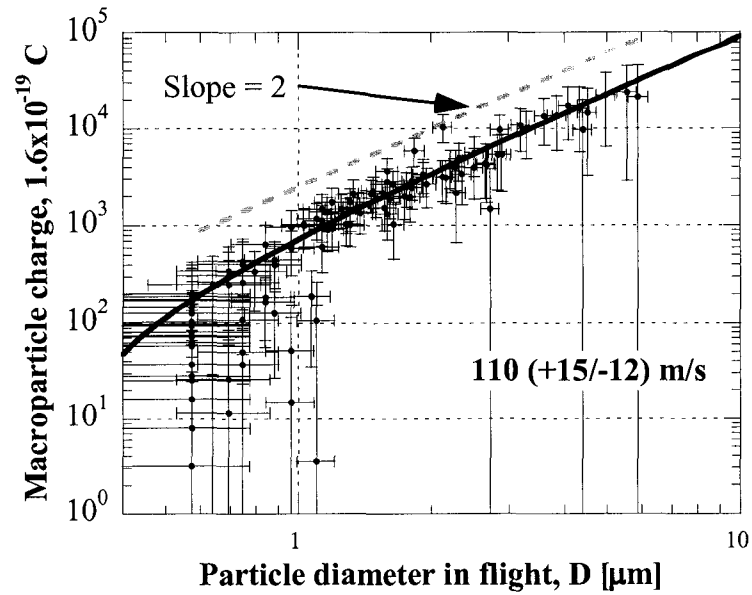


Figure 3.13 Accumulated macroparticle charge, plotted versus the particle diameter in flight for particles traveling 110 m/s, along with curve fit of the form $q=C_2D^2+C_1D+C_0$.
Test performed using 0.51 mm orifice configuration

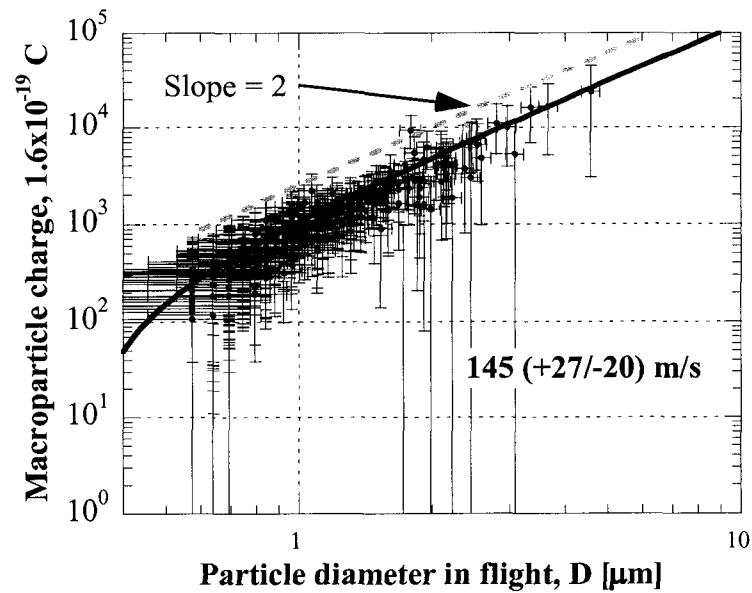


Figure 3.14 Accumulated macroparticle charge, plotted versus the particle diameter in flight for particles traveling 145 m/s, along with curve fit of the form $q=C_2D^2+C_1D+C_0$.
Test performed using 0.51 mm orifice configuration

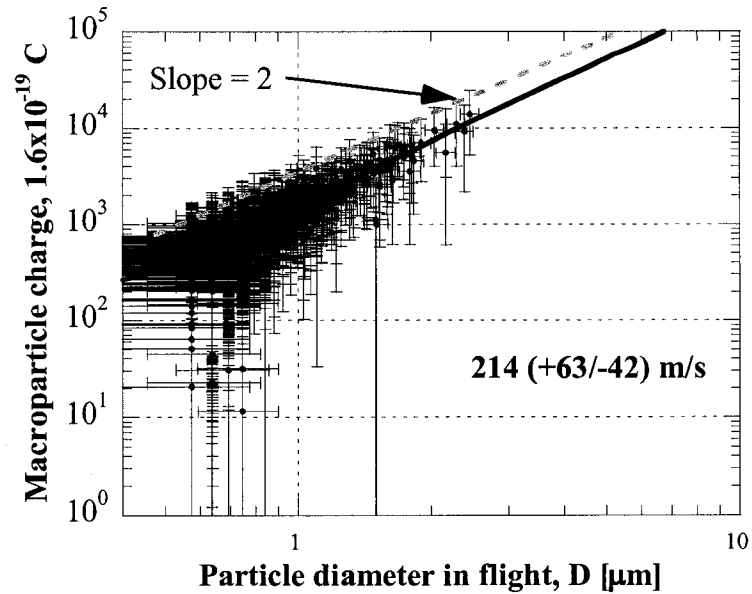


Figure 3.15 Accumulated macroparticle charge, plotted versus the particle diameter in flight for particles traveling 214 m/s, along with curve fit of the form $q=C_2D^2+C_1D+C_0$.
 Test performed using 0.51 mm orifice configuration

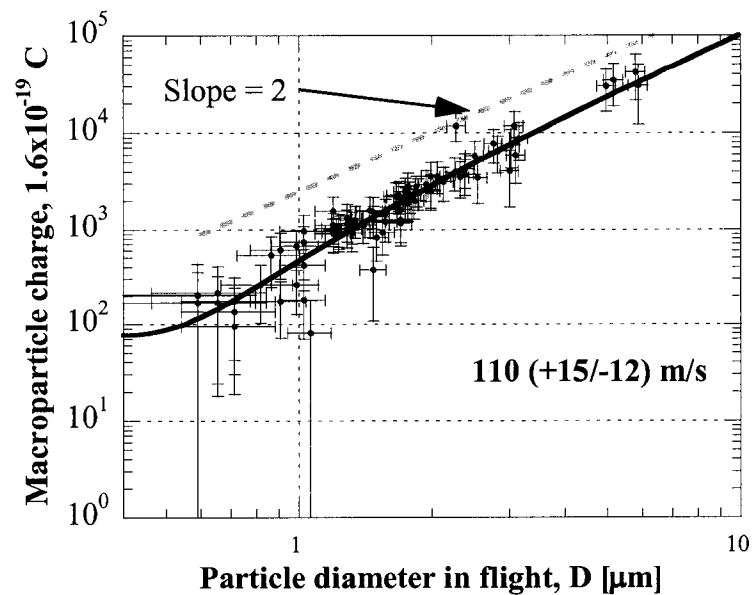


Figure 3.16 Accumulated macroparticle charge, plotted versus the particle diameter in flight for particles traveling 110 m/s, along with curve fit of the form $q=C_2D^2+C_1D+C_0$.
 Test performed using 0.37 mm orifice configuration

Figure 3.17 shows the curve fits of all the data, plotted to show how they compare to each other. From the figure, it appears that the particles collected during the 214 m/s test collected more charge than those in the other tests. Except for the 214 m/s data, within the

error bars, all the remaining data appear to lie on the same curve fit, regardless of the particle velocity.

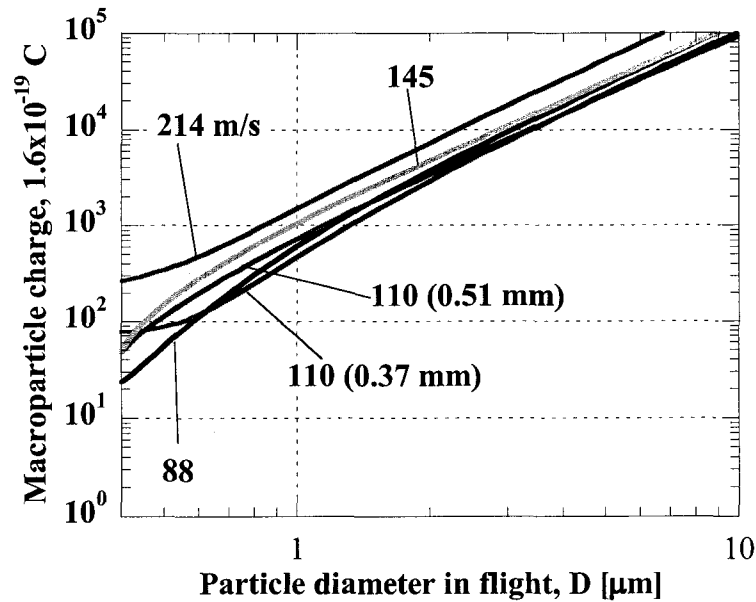


Figure 3.17 Curve fit of macroparticle charge, plotted versus diameter of particle in flight for all tested velocities

3.3 Error Analysis

Due to a number of uncertainties, the error bars associated with the calculated charge data is relatively large, especially for smaller particles. The error bars are calculated using the following equation.⁴⁸

$$w_r = \left[\left(\frac{\partial R}{\partial x_1} w_1 \right)^2 + \left(\frac{\partial R}{\partial x_2} w_2 \right)^2 + \dots + \left(\frac{\partial R}{\partial x_i} w_i \right)^2 \right]^{1/2} \quad 3-1$$

In the above equation, w_r is the total error, R is the results or the equation used to calculate the result, x_i are the independent variables, and w_i are the errors associated with each of the independent variables. In our case, R is the equation for the diameter of the particle in flight, (Eq. 2-13) and the equation to calculate the charge on the particles (Eq. 2-15). Table 3.1 shows the equations and values used in the calculation of the error bars.

Table 3.1 Parameters and equations used to calculate error bar for the macroparticle charge q

Independent Variable (uncertainty)	Derivative
$\rho_s = 8.92 \times 10^{-15} \pm 1 \times 10^{-17}$	$\frac{\partial q}{\partial \rho_s} = \frac{q}{\rho_s}$
$d = .01285 \pm .0005$	$\frac{\partial q}{\partial d} = \frac{q}{d}$
$\ell = 0.098 \pm .001$	$\frac{\partial q}{\partial \ell} = -\frac{2q}{\ell}$
$V_o = 7125 \pm 40$	$\frac{\partial q}{\partial V_o} = -\frac{q}{V_o}$
$s_o \pm 0.00095$ (primary) ± 0.00065 (secondary)	$\frac{\partial q}{\partial s_o} = \frac{q}{s_o}$
v_x (see Table 2.3)	$\frac{\partial q}{\partial v_x} = \frac{2q}{v_x}$
$A \pm 3$ pixels	$\frac{\partial q}{\partial A} = \frac{bq}{2A}$
$a = 0.0628 \pm 0.006$	$\frac{\partial q}{\partial a} = \frac{q}{a}$
$b = 2.83 \pm 0.1$	$\frac{\partial q}{\partial b} = \frac{1}{2} \ln\left(\frac{4A}{\pi}\right)q$

Table 3.2 Parameters and equations used to calculate error bars for the macroparticle flight diameter D

Independent Variable (uncertainty)	Derivative
$\rho_s = 8.92 \times 10^{-15} \pm 1 \times 10^{-17}$	$\frac{\partial D}{\partial \rho_s} = \frac{D}{3\rho_s}$
$\rho_l = 8.00 \times 10^{-15} \pm 5 \times 10^{-16}$	$\frac{\partial D}{\partial \rho_l} = -\frac{D}{3\rho_l}$
$A \pm 3$ pixels	$\frac{\partial D}{\partial A} = \frac{bD}{6A}$
$a = 0.0628 \pm 0.006$	$\frac{\partial D}{\partial a} = \frac{D}{3a}$
$b = 2.83 \pm 0.1$	$\frac{\partial D}{\partial b} = \frac{1}{6} \ln\left(\frac{4A}{\pi}\right)D$

There are three major sources of experimental uncertainty in the calculated charge: the measured surface area A , the particle velocity v_x , and the displacement s_0 . Other errors such as the value of the electric field and the variation in copper density as a function of temperature are negligible for most particles. For the calculated diameter during flight, the primary source of error is in the correlation between the particle volume and the impact diameter.

The uncertainty in the particle impact area stems from the fact that before the software can be used to locate and measure the size of the particles, the SEM images have to be converted to black and white. This involves setting a threshold value where a pixel brighter than the threshold is considered part of the particle, and pixels darker are not. The threshold value is different for each test, based on the contrast and brightness settings used in the SEM. The threshold is set in such a way that none of the background noise in the SEM images appears as particles. Because pixels on the edge of a particle may have a brightness near this threshold, this process has the effect of slightly changing the perceived size of macroparticles. The number of pixels actually changed by this process per macroparticle is relatively small, but for small particles, it has a large effect on the calculated charge. At 200x, a 1 μm diameter corresponds to 4 pixels, resulting in large errors for small particles.

The uncertainty in the velocity is based on the finite velocities that the filter allows through. Notice that as the velocities increase, the transmitted velocity distribution become wider. This is due to the short flight time of the particle ($\sim 350 \mu\text{s}$) compared to the pulse duration ($\sim 150 \mu\text{s}$). This is one of the reasons why there are many more particles in the 214 m/s velocity case, compared to the 88 m/s. There are also uncertainties in the electronics of the velocity filter, based on the precision of the motor speed, and the delay pulse duration, however, these are outweighed by the uncertainty associated with the design of the velocity filter.

The largest source of uncertainty is the error in the displacement s_0 , especially for the larger particles which were not displaced as much by the electric field as the smaller particles. Some of the largest particles were displaced as little as 2-3 mm. Since the error in that displacement is $\pm 0.95 \text{ mm}$ due to the size of the particle distribution as a result of the

geometry of the setup, the error bars on the large particles become large. This uncertainty assumes that the undeflected particle distribution is uniform. That is, the probability of a macroparticle forming anywhere on the cathode surface is the same. Figure 3.2 and Figure 3.6 show that this is not the case. The actual particle distribution is weighted toward the middle, resulting in a smaller error. In this instance, the error used to calculate the error bars is a worst case value.

The uncertainty in the correlation between the particle volume and the impact diameter is based on the standard deviation of the measured AFM data. Even though the AFM results have a high precision, the actual measurements deviate from the curve fit enough to result in a significant uncertainty of the final diameter calculation.

The calculation of the diameter in flight D also depends on the density of the liquid copper. That density varies with the temperature. The difference in copper density between the melting point (1356 K) and 2500 K is approximately 12% of the value resulting in an underestimation of the particle flight diameter by 4%. This error is reflected in the value of uncertainty of the liquid density in Table 3.2. Even with such a large variation, the uncertainty in the impact area A , and the correlation between the volume and impact diameter (a and b), greatly outweigh the uncertainty in the density of the liquid.

There is an error associated with the fact that the electric field used to deflect the particles may not be perfectly perpendicular to the flight of the particle. This could have the effect of slightly increasing or decreasing the MP velocity. Such an error is greatly outweighed by the uncertainty in the particle velocity due to the design of the velocity filter.

The electric field is generated by finite length parallel plates resulting in fringe fields near the ends of the deflecting region. This will have the effect of increasing the length of the electric field. Although the magnitude of the electric field in the fringe area will be reduced, there will be a traverse electric field present. Because the length of the electric field region is much longer than the plate separation, this error is assumed to be negligible.

The analysis used to calculate the charge on the macroparticle is based on the assumption that the MP charge is constant throughout its flight in the electric field. Due to the MP's

thermionic emission of electrons, the charge varies throughout its flight to the witness plate. However, it will be shown in a later section that the charge on the MP due to thermionic emission increases sharply after the plasma has extinguished, and then again when the particle enters the deflecting electric field. The time that the particle takes to reach an equilibrium charge is expected to be small compared to the time of flight. This means that particle charge throughout the electric field region will be approximately constant. Further discussion and analysis will be shown in Section 4.5.

3.4 Summary

This experiment measured the charge on macroparticles ejected from a pulsed, copper vacuum arc by measuring their change in trajectory after traveling through a transverse electric field. The vacuum arc current of 100 A, lasting 140 μs was generated using a LC pulse forming network. The experimental results show that the ejected macroparticles emitted have a positive charge, as opposed to the negative charge accumulated on MPs from a DC vacuum arc.³⁷ The results also show that the charge on the macroparticles is approximately proportional to the square of the particle diameter in flight ($q \sim D^2$). Within the error bars of this experiment, the charge on the MPs is not dependent on particle velocity.

Chapter 4

Macroparticle Charging Model

4.1 Background

As the macroparticle travels from the cathode spot to the witness plate, its flight can be separated into three stages. The first stage is when the vacuum arc is still present and the MP is traveling within the arc plasma. The second stage occurs after the arc has extinguished, and the MP has not yet reached the orifice or deflecting electric field. In this stage, the MP is traveling in a vacuum with little external influence. In the final stage, the particle has traveled through the two orifices, and entered the deflecting electric field. Each of these three stages is treated separately because the method of MP charging is significantly different during each stage.

During the first stage, the charge on the MP is a balance between three factors. When plasma particles, namely electrons, ions and neutrals collide with the MP, they are captured. When the MP collides with electrons or positive ions, the charge of the MP decreases or increases respectively. Each macroparticle in the plasma acts as a floating Langmuir probe, i.e. it will assume a potential necessary to assure zero net current to the macroparticle. Due to their high directed velocity compared to random velocity, the ions can be described as beam-like, while the electrons are gas-like because their random velocity is much higher than their drift velocity.

Macroparticle charging and transport in vacuum arcs was also studied by Keidar et al.^{37,49,50} Those studies found that due to the higher mobility of the electrons, more electrons are collected than ions, resulting in a net negative MP charge in the plasma. An experimental test where macroparticles were deflected from a witness plate by placing the witness plate at a negative potential later confirmed this result.³⁶ Before the present experiment, it was therefore predicted that the pulsed vacuum arc MP would also have a negative charge.

Later theoretical studies by Delzanno et al showed that for high temperatures a third factor, namely the thermionic emission of the MP must be taken into consideration when modeling

MP charge in a plasma. If the MP has a sufficiently high temperature, this electron emission can alter the equilibrium charge, even reversing it and resulting in a net positive charge.⁵¹ The orbit motion limited (OML) theory describes the charging of particles in a plasma, taking into consideration the thermionic emission of the particle.⁵² However, using a numerical simulation, it was shown that the quantitative results of the OML theory are only accurate for small particles.⁵¹ For particles whose diameter is larger than the Debye length near the particle, the OML theory becomes inaccurate.

During the second stage of flight, the MP is flying in vacuum without the presence of a plasma, or other external influences. The MP charge is affected solely by the thermionic emission due to the high temperature of the particle. In this stage, as the MP charge increases, the floating potential of the particle becomes high enough to inhibit emitted electrons from escaping the potential well. Once the MP floating potential becomes high enough, the particle reaches a potential where very few electrons have sufficient energy to escape, and consequently, the MP charge remains constant.

Once the particle enters the strong deflecting electric field however, the strength of the electric field is such that for larger particles, the potential well around the particle is significantly affected. On one side of the MP, the electric field emitted from the particle is increased, making it more difficult for electrons to escape. On the other side, the deflecting electric field decreases the strength of the particle local electric field, resulting in increased electron emission. For a 10 μm diameter particle charged to 10000e the electric field at the surface of the particle is 5.7×10^5 V/m. This is approximately the same magnitude as the as the deflecting electric field of 5.5×10^5 .

When the particle charge is small, the electric field on one half of the particle surface is reversed, resulting in increased electron emission due to the negative electric field. For larger particles, this effect results in a jet of electrons emitted from one side of the particle. This jet further increases the charge on the particle, until the electric field due to the particle charge counteracts the effect of the deflecting electric field. At this point, electrons on the up-field side of the particle must have a sufficient energy to overcome the electric field near the particle surface. This results in reduced electron emission, until the electric field at the

surface is such that very few electrons have sufficient energy to escape the particle, and thermionic emission ceases.

It will be shown later that the charge on the particle after the arc is extinguished does not affect the final MP charge significantly, and that the thermionic emission of the particle in vacuum, and in the deflecting electric field, dominates the final charge on the macroparticle. Therefore, in this work, primary consideration will be given to the second and third stages of the particle flight.

4.2 Macroparticle Thermionic Emission

When the MP leaves the cathode spot, it is estimated that the particle temperature is greater than 1500 °C, depending on where in the cathode spot it was formed. At these temperatures, the copper is a liquid, and emits electrons through thermionic emission. The emission current density J_{the} for a particle at temperature T_p is described by Richardson's Law or the Richardson-Dushman equation shown below.

$$J_{\text{the}} = AT_p^2 \exp\left[-\frac{e}{kT_p}(\phi)\right] \quad 4-1$$

where ϕ is the material work function in electron volts and A is Richardson's constant:

$$A = \frac{4\pi m_e k^2 e}{h^3} = 1.2017 \times 10^6 \frac{\text{A}}{\text{m}^2 \text{K}^2} \quad 4-2$$

where m_e and e are electron mass and charge respectively, k is Boltzmann's Constant, and h is Planck's constant. This equation assumes that the energy states available to the free electrons in the particle are uniformly distributed in the momentum space, and the Fermi function describes the probability of occupation of any state. An electron will escape through the surface of the particle if its normal kinetic energy is sufficient to overcome the surface barrier ψ . The surface barrier is described by $\psi = \phi - E_f$ where the Fermi energy $E_f = 7.00 \text{ eV}$ for Copper.^{53,54}

4.2.1 Negatively Charged Particle

If the emitting particle becomes negatively charged, an electric field is formed around the macroparticle, accelerating electrons away. In this case, the Richardson-Dushman equation must be adjusted for the Schottky effect. The thermionic emission is dependent on the work function of the material. This work function is reduced by the presence of an electric field at the particle surface according to the following equation:⁵⁵

$$J_{\text{the}} = AT_P^2 \exp\left[-\frac{e}{kT_P}\left(\phi - \sqrt{\frac{e(-E_s)}{4\pi\epsilon_0}}\right)\right] \quad 4-3$$

where ϵ_0 is the permittivity of free space and E_s is the electric field at the particle surface:

$$E_s = \frac{q}{\pi\epsilon_0 D^2} \quad 4-4$$

The electric field is defined as positive in the radial direction. When the particle charge is negative, the electric field is pointing toward the particle surface.

4.2.2 Positively Charged Particle Without External Electric Field

After the plasma has extinguished, and the MP is traveling in the open vacuum, there is no longer a mechanism to charge the particle negatively. Thus, thermionic emission will dominate the charge of the MP, resulting in a positive charge. It will be shown later that even if the MP charge is negative coming out of the plasma, the time it takes to emit enough electron to charge positively is short compared to the flight time. A positively charged particle has a spherically symmetric potential hump around the particle, and radial electric field lines from the particle surface. The bottom plot in Figure 4.1 shows the potential and electric field lines for a 10 μm diameter particle charged to 3000e. The top plot in the figure shows the potential along the z axis ($\theta = 0$ and $\theta = \pi$).

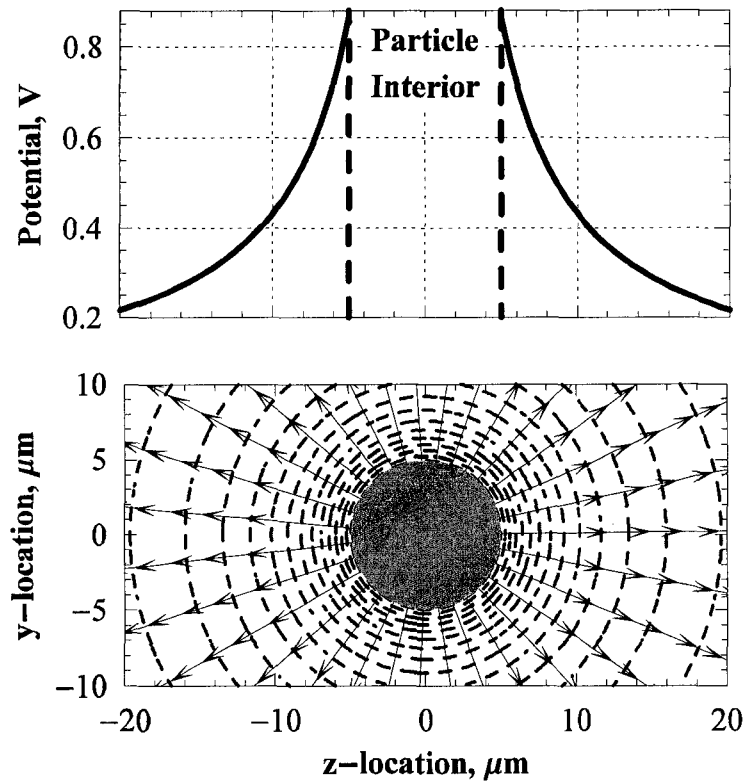


Figure 4.1 Plot of the potential along the z-axis (top) and the potential (dashed) and electric field (solid arrows) lines near a 10 μm diameter macroparticle with $q=3000e$ and $E_z = 0$

In order for an electron to escape the particle, not only does it have to overcome the energy barrier associated with leaving the particle surface, it then has to have enough kinetic energy to escape the potential hump formed around the particle. Namely:

$$\frac{1}{2} m_e u^2 > \frac{eq}{2\pi\epsilon_0 D} \quad 4-5$$

where u is the magnitude of the electron velocity. The same analysis used to determine the Richardson-Dushman equation is used with this added requirement, resulting in the following equation for the thermionic emission of a positively charged particle without an external electric field.⁵⁶

$$J_{\text{the}} = AT_P^2 \left(1 + \frac{e\Phi_a}{kT_P} \right) \exp \left[-\frac{e}{kT_P} (\phi + \Phi_a) \right] \quad 4-6$$

In this equation, the work function ϕ in the exponent is adjusted by the particle floating potential Φ_a :

$$\Phi_a = \frac{q}{2\pi\epsilon_0 D} \quad 4-7$$

The total current emitted from the MP is simply the current density times the surface area.

$$I_{\text{the}} = \pi D^2 J_{\text{the}} \quad 4-8$$

4.2.3 Particle in Transverse Electric Field

Immediately after the arc is extinguished, the particle is traveling in open vacuum, where the thermionic emission is governed by Eq 4-6. Once the particle travels past the orifice and enters the electric field, Eq. 4-6 is no longer valid because the equation assumes that the potential hump that the electrons have to overcome in order to escape the particle is spherically symmetric. Once a high external electric field E_z is applied, the potential around the particle becomes strongly modified.

This problem is solved using the method of images as discussed by Jackson (Ref. 57). The potential Φ around the particle in a uniform electric field of strength E_z is

$$\Phi = -E_z \left(r - \frac{a^3}{r^2} \right) \cos(\theta) + \frac{q}{4\pi\epsilon_0 r} \quad 4-9$$

where a is the radius of the MP, and r and ϕ are the radius and azimuthal angle in spherical coordinates. Differentiating this equation in spherical coordinates gives the radial and azimuthal electric field terms.

$$E_r = E_z \left(1 + \frac{2a^3}{r^3} \right) \cos(\theta) + \frac{q}{4\pi\epsilon_0 r^2}$$

$$E_\theta = -\frac{E_z}{r} \left(r - \frac{a^3}{r^2} \right) \sin(\theta)$$
4-10

Once the particle has passed the orifices and has entered the deflecting electric field, the potential contours due to the electric field will dominate the potential in the vicinity of the particle. The electric field at the surface of the MP on the side nearest the positive electric field plate (up-field side) will be significantly altered by the electric field, possibly opposite in sign to the electric field on the down-field side. This effect is more pronounced for larger particles. The field lines near a 10 μm particle with a charge of 3000e, entering a region of $E_z = 5.5 \times 10^5$ V/m are calculated using equations 4-9 and 4-10, and shown in Figure 4.2. The potential plot (top) assumes that the particle is precisely half way between the plates producing the electric field.

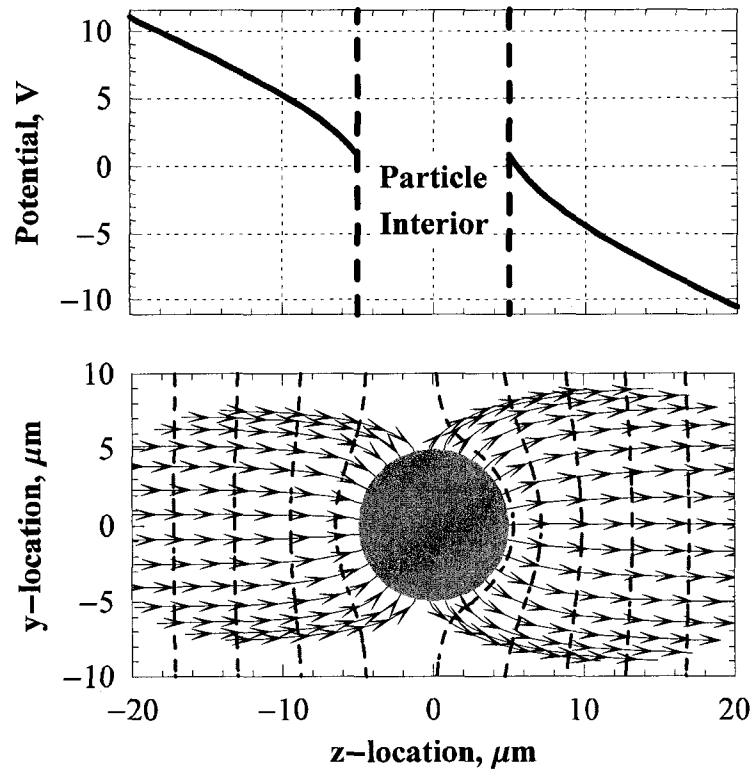


Figure 4.2 Plot of the potential along the z-axis (top) and the potential (dashed) and electric field (solid arrows) lines near a $10\ \mu\text{m}$ diameter macroparticle with $q=3000e$ and $E_z = 5.5 \times 10^5\ \text{V/m}$

As the charge of the particle increases to a point where it overcomes the E_z field, the electric field on the entire surface will be positive. The potential in the immediate vicinity of the MP on the up-field side (left side in Figure 4.3) begins to form a potential hump near the particle, similar to spherically symmetric potential hump shown in Figure 4.1. Farther away from this particle, the deflecting electric field again dominates. Figure 4.3 shows an example of such a configuration where the charge is $30,000e$ and the E_z field remains $5.5 \times 10^5\ \text{V/m}$.

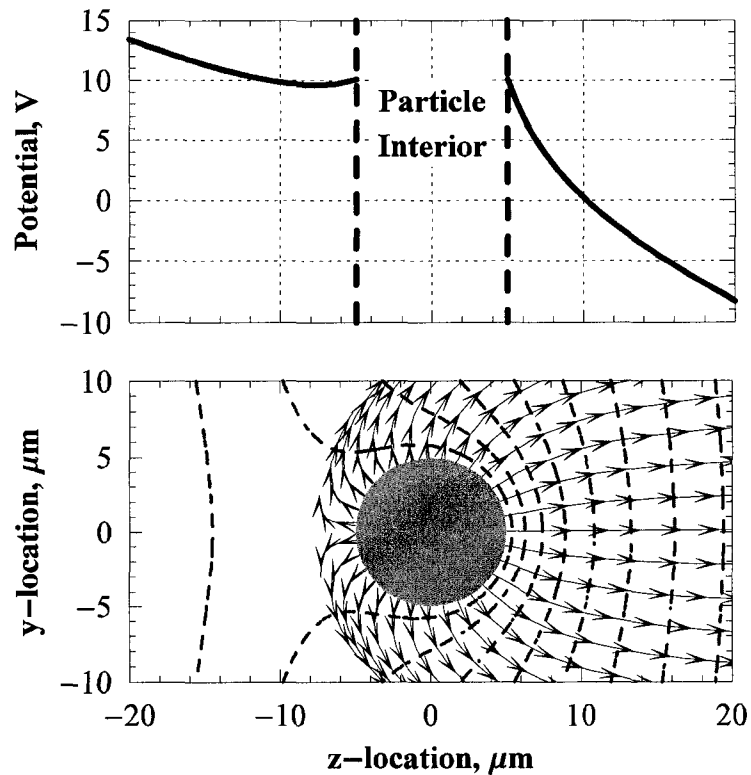


Figure 4.3 Plot of the potential along the z-axis (top) and the potential (dashed) and electric field (solid arrows) lines near a 10 μm diameter macroparticle with $q= 30,000e$ and $E_z = 5.5 \times 10^5 \text{ V/m}$

In order to calculate the thermionic emission from such a particle, the current density is integrated over the surface of the particle. The equation for the current density is determined by the potential experienced by an emitted electron. By assuming a radial electron trajectory ($\theta = \text{constant}$), that potential can be calculated from Eq 4-9. The trajectory is not typically radial, however, calculating the thermionic emission by calculating the trajectory of each electron emitted is left for future work.

If the electron sees a negative electric field, the current density from the emitted location will be that of a negatively charged particle (Eq. 4-3). If the electric field is positive, and the potential has a minimum value as in the left side potential in Figure 4.3, then the current density takes the form of a positively charged particle (Eq 4-6). In this case, in order to escape the MP, the electron kinetic energy must be greater than the depth of the potential well through which it travels ($\Delta\Phi$) as opposed to the floating potential of the particle. For

this reason Φ_a in equation 4-6 is replaced with the difference between the potential at the particle surface, and the potential at the local minimum. Finally, if the electric field is positive, and there is no local minimum, then it is assumed that the electron will be attracted back to the MP. This is the case on the side of the particle nearest the negative electric field plate ($0 < \theta < \pi/2$). The total current emitted from the particle is then the integral of the current density across the particle surface (Eq. 4-11), and the current density is summarized in Eq. 4-12.

$$I_{the} = 2\pi a^2 \int_0^\pi J_{the}(a, \phi, T_p, q, \theta, E_z) \sin(\theta) d\theta \quad 4-11$$

$$J_{the} = \begin{cases} E_s \leq 0 & AT_p^2 \exp\left[-\frac{e}{kT_p} \left(\phi - \sqrt{\frac{e(-E_s)}{4\pi\epsilon_0}}\right)\right] \\ E_s > 0 & \begin{cases} E_z = 0 & AT_p^2 \left(1 + \frac{e\Phi_a}{kT_p}\right) \exp\left[-\frac{e}{kT_p}(\phi + \Phi_a)\right] \\ E_z \neq 0 & \begin{cases} \theta > \frac{\pi}{2} & AT_p^2 \left(1 + \frac{e(\Delta\Phi)}{kT_p}\right) \exp\left[-\frac{e}{kT_p}(\phi + \Delta\Phi)\right] \\ \theta \leq \frac{\pi}{2} & 0 \end{cases} \end{cases} \end{cases} \quad 4-12$$

where $\Delta\Phi$ is the depth of the potential well through which the electron travels and E_s is the radial electric field at the surface of the particle.

Figure 4.4 shows the current emitted from a 10 μm diameter particle at 2200 K, both with and without an external electric field of 5.5×10^5 V/m. When the particle has a low positive charge, the electric field has the effect of reducing the total thermionic current from 3.1×10^{-8} to 1.9×10^{-8} . However, at high particle charge, the electric field significantly increases the thermionic current, which increases the final particle charge by a factor of 5 for a 10 μm particle.

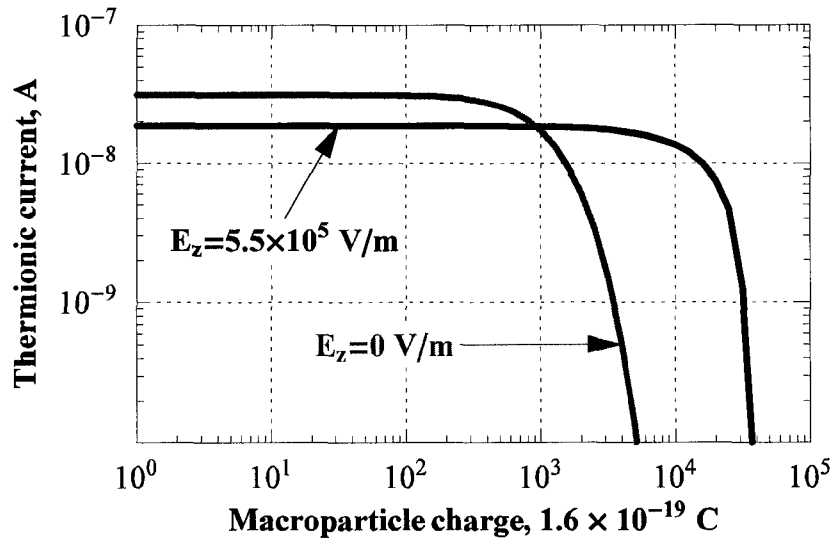


Figure 4.4 Thermionic current from a $10 \mu\text{m}$ diameter particle at $T_p = 2200$ K, plotted versus the MP charge, both with and without an external electric field $E_z = 5.5 \times 10^5$ V/m

4.3 Macroparticle Temperature

All the above equations for the thermionic current density are heavily dependent on the particle temperature. After the arc has extinguished and the particle is in open vacuum, two sources of heat loss dominate the temperature calculations for the particle. The primary source of heat loss is due to radiation. The power lost to radiation follows the following equation.

$$P_{\text{rad}} = \epsilon \sigma a^2 (T_p^4 - T_c^4) \quad 4-13$$

Where ϵ is the emissivity for the particle, σ is the Stefan-Boltzmann constant, T_c is the temperature of the surroundings and a is the MP radius.

The second source of heat loss is the energy removed by each electron as it escapes the particle through thermionic emission. Each electron removes an energy equal to the work function ϕ as it leaves the MP, resulting in a power loss due to thermionic emission:

$$P_{\text{the}} = \phi I_{\text{the}} \quad 4-14$$

Another source of heat loss is the energy removed due to the MP evaporation. As copper atoms evaporate from the surface of the MP, they remove energy equal to the heat of vaporization. The heat of vaporization for copper is 300 kJ/mol or 4.98×10^{-19} J/particle. Using calculations for thermal evaporation from particle vapor deposition,⁵⁸ the molecular flux F from the MP surface follows the following equation

$$F = \frac{p_{eq}}{\sqrt{2\pi mkT_p}} \quad 4-15$$

where p_{eq} and m are the vapor pressure and molecular weight of copper respectively. The vapor pressure of copper is:

$$p_{eq} = 10^A 10^{-\frac{B}{T_p}} \quad 4-16$$

where A and B for copper are 10.588 and 15821 respectively.⁵⁹ Using the values for copper, Eq. 4-16 is plotted in Figure 4.5.

For all particle sizes considered, the heat loss due to evaporation is equal to the heat loss due to radiation at $T_p = 2200$ K. The evaporation heat loss is much more sensitive to the MP temperature than the radiation term which is proportional to T_p^4 . For this reason, evaporation term will dominate the MP heat loss at temperatures above 2200 K. Also, because the evaporation heat loss term rises so quickly with temperature, MPs that start at temperatures above 2200 K will quickly lose heat until their temperature falls to approximately 2200 K where the radiation heat loss term will begin to dominate. This means that even though the MP temperature is not well known, the peak MP temperature outside of the plasma is not expected to be larger than 2200 K.

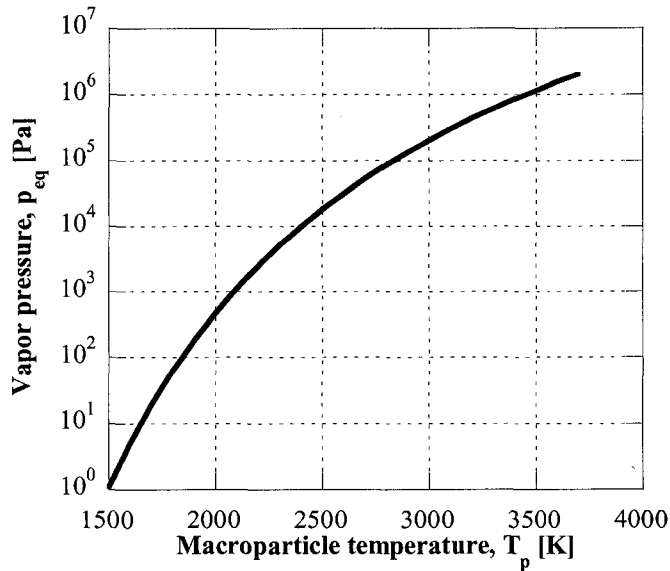


Figure 4.5 Vapor pressure of copper versus temperature

4.4 Model Results

In order to calculate the MP temperature and charge during flight, the following differential equations were solved using Mathematica's numerical differential equation solver⁶⁰

$$T_p'[t] = -\frac{P_{rad}[t] + P_{the}[t]}{\rho[T_p]C_p V_p} \text{ Kelvin/sec} \quad 4-17$$

$$q'[t] = \frac{P_{the}}{\phi e} \text{ Coulombs/sec}$$

where C_p is the specific heat of liquid copper $494 \text{ J}/(\text{kg K})$ ⁴², V_p is the volume of the particle, and $\rho[T_p]$ is the density of the copper particle as a function of the temperature:

$$\rho[T_p] = 8002 - 0.801(T_p - 1083) \quad 4-18$$

The work function⁶¹ and the emissivity⁶² used in these calculations are $\phi = 4.7 \text{ eV}$ and $\epsilon = 0.14$ respectively. Equation 4-17 assumes that the temperature distribution inside the macroparticle is constant. Namely, the heat conduction from the surface into the center of the sphere is faster than the heat loss due to radiation. The heat loss due to radiation P_{the} is shown in Eq. 4-13, and the heat conducted away from the surface into the particle P_{cond} is approximated by the equation:

$$P_{\text{cond}} = \frac{\kappa T_p}{a} \pi D^2 \quad 4-19$$

where the thermal conductivity of copper $\kappa = 380$ W/m-K. For $T_p = 2500$ K, the ratio $P_{\text{cond}}/P_{\text{the}}$ is 6×10^5 , indicating that the assumption of a constant temperature distribution inside the particle is valid.

The following plots show sample results for 1 μm and 10 μm diameter particles with initial conditions: $T_o = 2200$ K and $q_o = 0$. An initial charge $q_o = 0$ is chosen because the high thermionic emission rate of negatively charged particles makes the final charge almost independent of initial charge as discussed in Section 4.5. Figure 4.6 and Figure 4.7 show the charge and temperature during flight. As described above, the charge increases sharply when the particle enters the electric field. This increase is more pronounced for larger particles. Figure 4.8 and Figure 4.9 show the magnitudes of the power lost to radiation and thermionic emission during the flight.

Figure 4.10 and Figure 4.11 show the final charge and temperature drop after the particle flight versus initial temperature. The initial temperature is not well known for a number of reasons discussed in Section 4.5. Throughout the flight, for all initial conditions, the radiation term dominates the total power loss compared to thermionic emission. This makes the rate of change of temperature proportional to the particle surface area divided by the volume, which results in the greater temperature change for smaller particles shown in Figure 4.10 and Figure 4.11. By compiling the final charge data for particles of different size, a relationship between the particle diameter and final particle charge is calculated and shown in Figure 4.12. Figure 4.12 also includes an approximate curve fit to the experimental data from Section 3.2. The charge in Figure 4.12 is plotted for 5 different initial temperatures ranging up to 3500 K.

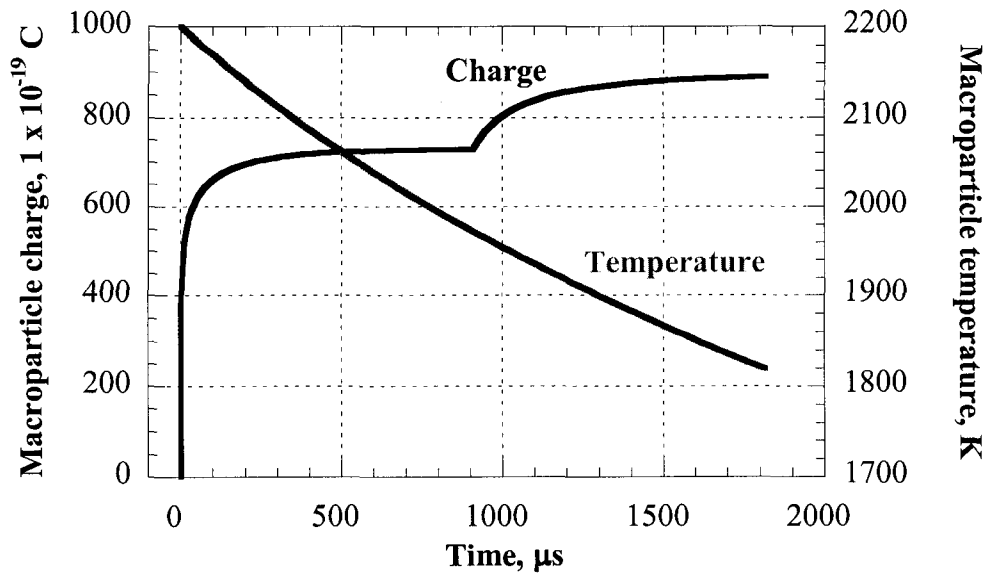


Figure 4.6 Macroparticle charge and temperature during flight for a 1 μm diameter particle, with initial conditions: $T_0=2200$ K and $q_0=0$

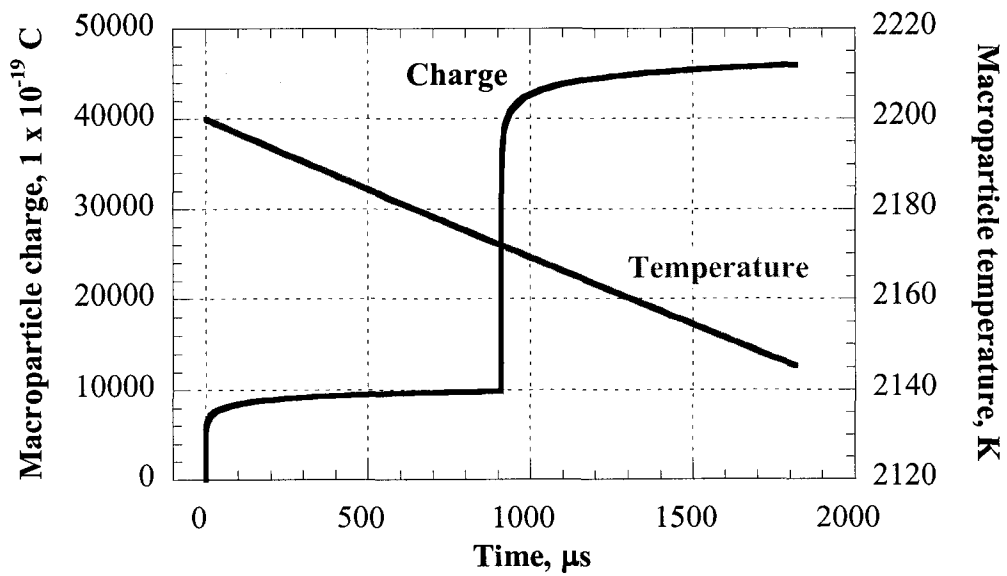


Figure 4.7 Macroparticle charge and temperature during flight for a 10 μm diameter particle, with initial conditions: $T_0=2200$ K and $q_0=0$

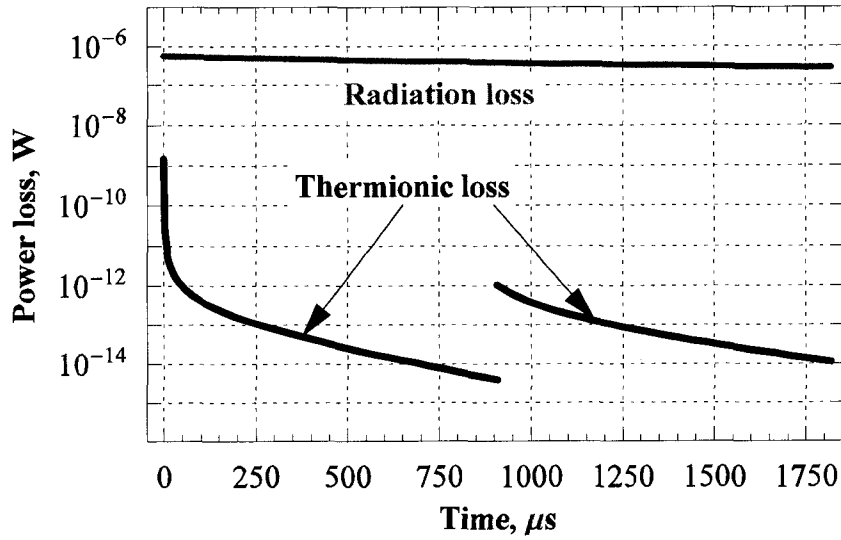


Figure 4.8 Power loss due to radiation and thermionic emission during flight for a 1 μm diameter particle, with initial conditions: $T_0=2200\text{ K}$ and $q_0=0$. $\Delta T_p = 564\text{ K}$

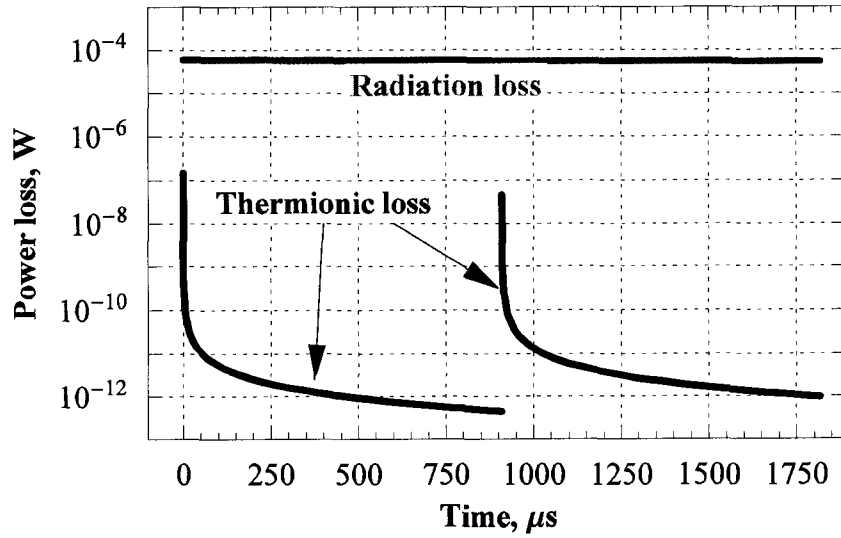


Figure 4.9 Power loss due to radiation and thermionic emission during flight for a 10 μm diameter particle, with initial conditions: $T_0=2200\text{ K}$ and $q_0=0$. $\Delta T_p = 92\text{ K}$

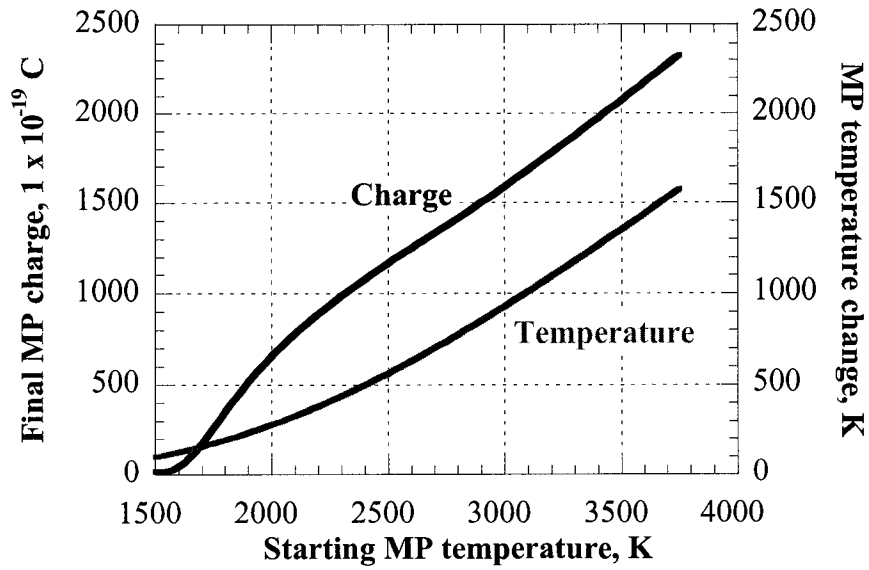


Figure 4.10 Final MP charge and change in MP temperature plotted versus the starting temperature for a 1 μm diameter particle, with initial conditions: $q_0 = 0$

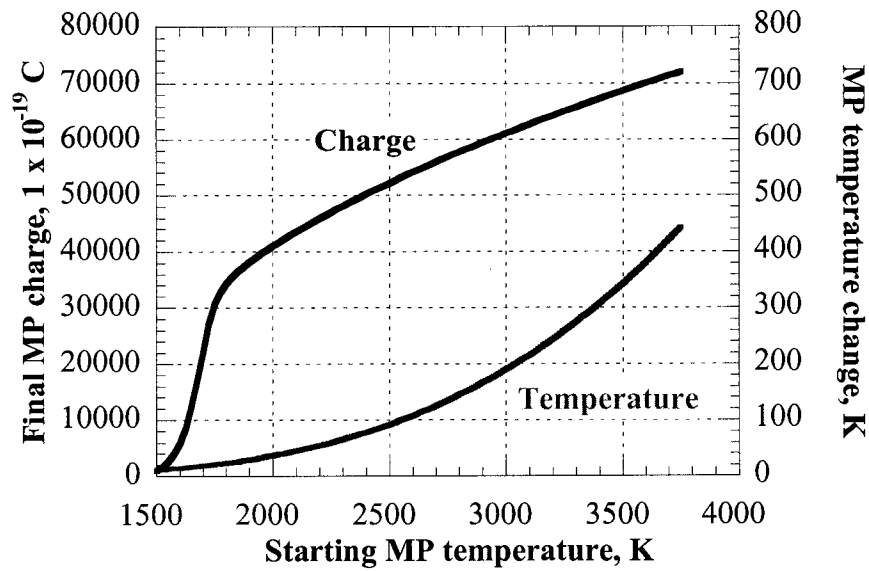


Figure 4.11 Final MP charge and change in MP temperature plotted versus the starting temperature for a 10 μm diameter particle, with initial conditions: $q_0 = 0$

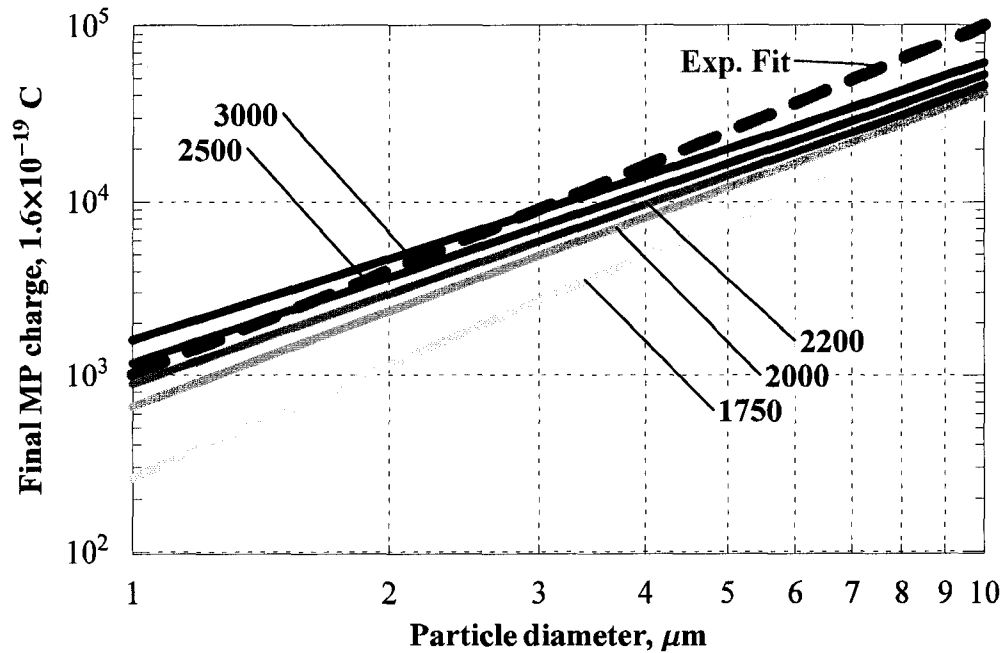


Figure 4.12 Final macroparticle charge plotted versus diameter for various initial temperatures, along with an approximate curve fit to the experimental data.

4.5 Discussion

As was mentioned before, this model is primarily focused on the flight of the macroparticle after the vacuum arc has extinguished. The interaction between the macroparticle and the plasma provide the initial conditions for the above calculations. A model to determine the effect that the vacuum arc plasma has on the macroparticle temperature and charge can be found in the literature.^{26,37} These models indicates that the plasma will heat the MP as well as bring the MP to a negative charge. It also indicates that the increase in temperature of a MP in the plasma due to neutral electron and ion collisions will be inversely proportional to the MP size. However, one of the input parameters into that model is the poorly-known temperature of the MP as it ejects from the cathode spot.

The temperature in the center of the cathode spot can be as high as 4000 K.¹⁰ However, that temperature falls off with radial distance from the center, until the temperature is below the melting point of copper. Thus, the MP temperature is dependent on where within the cathode spot it was formed. The MPs are formed when magnetic and gas dynamic pressure splash out liquid cathode material.²⁵ This implies that the MPs are formed at the outer edge

of the cathode spot, resulting in a MP temperature lower than the temperature of the center of the cathode spot. As the particle size increases, the MP diameter becomes on the order of the cathode spot diameter, indicating that some of the higher temperature metal from the center of the cathode spot may be included in the MP. This could mean that the initial MP temperature could be dependent on the MP size.

The interaction between the MP and the plasma also affects the MP temperature. Although a model of this effect is available in the literature, the amount of time that a MP spends in the plasma depends on when the MP was formed. If the MP was formed near the beginning of the pulse, it may spend the entire arc duration inside the arc. However, if the MP is formed near the end of the pulse, only a small fraction of time will be spent inside the plasma. These factors make it difficult to model an accurate MP temperature, and there is no known experimental study of the MP temperature leaving the cathode spot, or the vacuum arc plasma. For this reason, the initial temperature for the model described above has been left as a variable.

From Figure 4.6 and Figure 4.7, the charge of a particle with $q_0 = 0$ increases to 80% of its final charge outside the deflecting electric field ($t \approx 800 \mu\text{s}$) within the first $10 \mu\text{s}$ of its flight. Also, the thermionic emission increases exponentially when the particle is charged negatively (Eq. 4-3). Thus, even though the charge of the macroparticle in the plasma is expected to be negative due to the higher mobility of the electrons, the time for the particle to become positively charged is insignificant compared to the time of flight. This has the effect of making the final charge independent of the initial charge q_0 for $q_0 <$ the final charge.

On the other hand, if the ion collisions or thermionic emission of the particle during the arc overpowers the electron collision rate, and the particle charge were positive when the arc extinguished, this would have the same effect as increasing the flight time. However, because the final charge is not limited by the flight time, but instead by the final floating potential of the MP, the charge of the MP would not be affected by variations in the initial charge.

As mentioned above, in the beginning of the MP flight, the charge on the MP quickly increases until it reaches an equilibrium value, after which point it increases only slightly. Recall that the method used to calculate the charge on a particle from the experimental results assumes that the charge on the MP is constant (Section 2.1.3). In order to estimate the error associated with this assumption, the actual displacement using the charge profile during flight was calculated. This calculated displacement was then plugged in to Eq. 2-11 to calculate the charge based on a constant charge assumption. Figure 4.13 shows a plot of the percentage error as a function of initial temperature for various particle sizes. This error is never greater than approximately 10 %. The charge calculated by Eq 2-11 is an average charge on the MP during its flight, which in the case of an increasing MP charge, will underestimate the actual final charge.

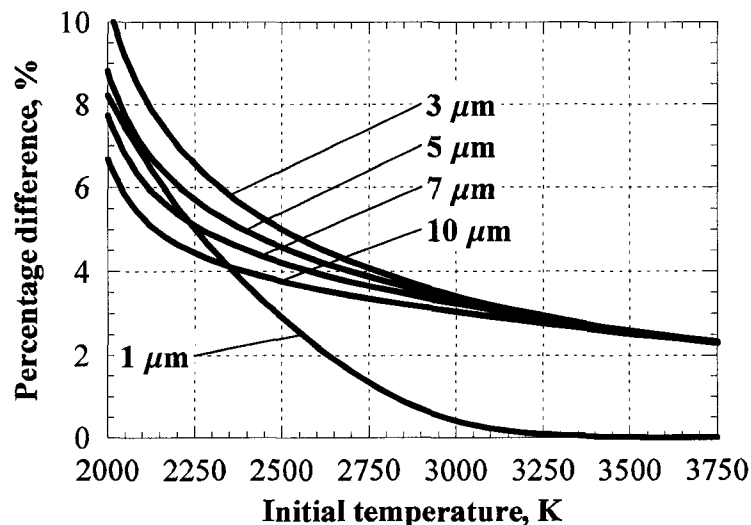


Figure 4.13 Error associated with the assumption of a constant charge on the MP during flight though the electric field.

Due to the complexity of the calculation of the thermionic emission of a macroparticle inside a transverse electric field, including a numerical integral over the surface of the MP, the equation for the power loss due to thermionic emission could not be calculated "on-the-fly" or during the course of the normal calculations. Instead, the thermionic power loss was tabulated in increments of 25 K and 50e Coulombs within the temperature and charge range for each particle size. This tabulated data is a 2 dimensional array of values for each particle size, approximately 160,000 data points per particle size. The final results were then

calculated using first order interpolations of these tables. The largest error between the actual value and the interpolated data occurs at low temperatures where the thermionic emission is no longer contributing to the total charge of the particle. In the range of particle charge and temperature where the thermionic emission is significant to the calculation, the maximum error in thermionic emission is approximately 0.2% of the actual value. This magnitude of error only occurs between tabulated points. Due to the large change in the thermionic emission, this error has no effect on the final calculated charge.

The actual value of the emissivity of copper varies from 0.112 to 0.20 in the literature.^{63,64,65} One study showed that the emissivity increases with temperature to a value of 0.20 at 1800 K.⁶⁵ The sensitivity of the calculated final charge to the emissivity is not severe. Table 4.1 shows the percentage difference that a 43% change in the emissivity has on a particle of various size for an initial temperature of 2200 K. A smaller emissivity results in a greater final charge because the temperature drop throughout the flight is reduced. The largest effect is on a 1 μm particle with a reduced emissivity of 0.08, resulting in an increase of 17%. As the particle diameter increases, this effect quickly falls resulting in a 6% change in a 3 μm diameter particle and a 1% change in a 10 μm diameter particle.

Table 4.1 Percentage difference in the calculated final MP charge for a 43% change in the original emissivity $\epsilon = 0.14$

MP diameter [μm]	$\epsilon = 0.08$	$\epsilon = 0.20$
1	+18%	-12%
3	+5%	-4%
5	+2%	-2%
7	+2%	-1%
10	+1%	-1%

There is some uncertainty in the literature as to the work function of liquid copper. Some measurements indicate that the work function can be as low as 4.4 eV.^{61,66} The effect of lowering the work function on the final charge of the macroparticle is shown in Figure 4.14. The greatest effect occurs when the starting temperature is below 2000 K. Above $T_0=2000$ K the effect of reducing the work function to 4.4 is small compared to the uncertainty of the temperature.

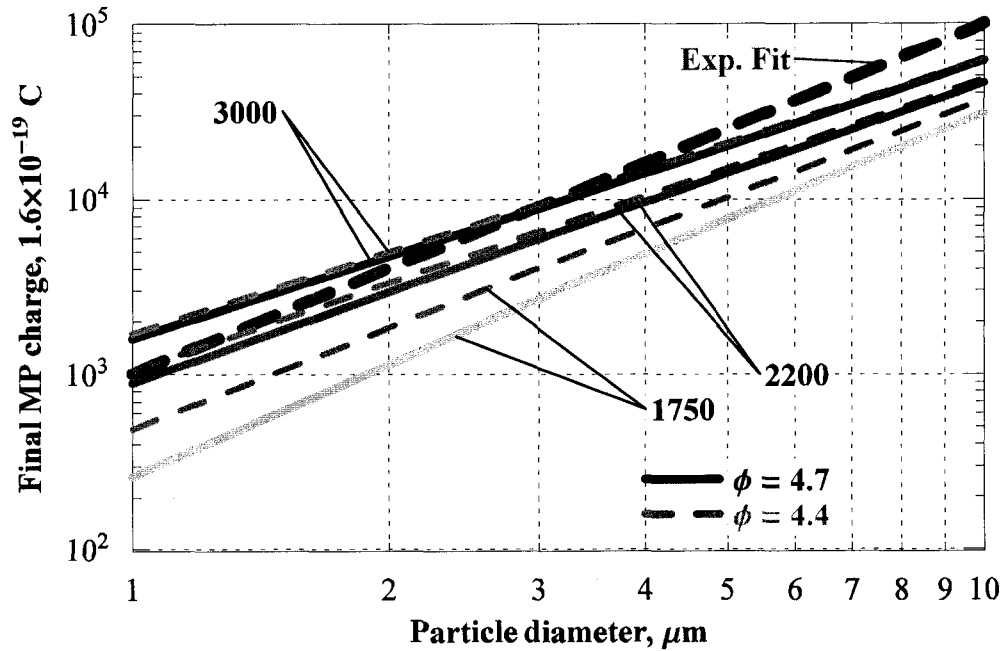


Figure 4.14 Comparison between final MP charge vs. diameter for two work functions

Near the end of the particle's flight, as well as before the particle enters the electric field, it reaches a positive equilibrium charge. At this point, most of the electrons emitted from the particle surface return to the particle due to its attractive potential. This results in an electron cloud around the particle. The current density emitted from the surface of the particle for a positively charged particle is given by the Richardson-Dushman equation (Eq 4-1). That current density is distributed evenly across the surface of the particle and is related to the electron number density and velocity according to the equation

$$j = en_e v_e \quad 4-20$$

where n_e and v_e are the electron number density and velocity respectively. The electron number density n_e can be determined by assuming the electron velocity is equal to the thermal velocity:

$$v_e = \sqrt{\frac{2kT_e}{m_e}} \quad 4-21$$

where the electron temperature T_e is equal to the particle temperature T_p . Dividing Eq. 4-22 by the electron velocity v_e and charge e , an electron number density at the surface of the particle can be estimated. Using this electron density, a Debye length is calculated according to

$$\lambda_D = \sqrt{\frac{\epsilon_0 k T_e}{n_e e^2}} \quad 4-22$$

where the electron temperature T_e is equal to the particle temperature T_p . The electron density is also used to calculate the electron mean free path:

$$\lambda = \frac{1}{n_e Q_{ee}} \quad 4-23$$

where the electron-electron cross section is given by³⁸

$$Q_{ee} = \frac{6.5 \times 10^{-13}}{T_{eV}^2} \text{ cm}^2 \quad 4-24$$

The electron mean free path is plotted for a 1 μm and 10 μm diameter particle in Figure 4.15. This calculation assumes that the electron density remains constant with radius. That means that the actual mean free path will be larger than the calculated value. The plot shows that for temperature near 3750 K, the electron mean free path approaches the diameter of the particle, for larger particles. However, for most conditions considered, the mean-free path is long enough that the sheath around the MP is collisionless. This means that electrons emitted from the macroparticle do not interact with each other, and their motion is governed purely by the local electric field.

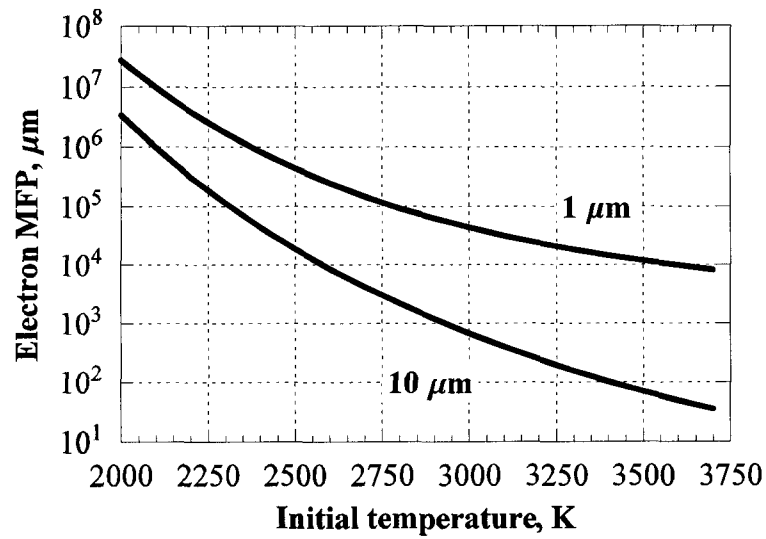


Figure 4.15 Electron mean free path in the vicinity of a 1 μm and 10 μm diameter macroparticle versus the particle temperature

Chapter 5

Summary and Conclusion

5.1 Summary

This paper described the design and implementation of an experiment to measure the charge on macroparticles leaving the exhaust plume of a pulsed vacuum arc thruster. The macroparticles exiting the VAT are in the form of molten copper cathode droplets. The experiment accomplished this by first limiting the velocity of macroparticles examined to a small range with a time-of-flight velocity filter. Once a particle traveled through the velocity filter, it was exposed to a transverse E_z electric field generated by charging two parallel plates to a positive and negative high voltage. By measuring the change in trajectory of the MPs after traveling through the electric field, the charge was calculated.

The velocity filter was designed to pass particles during a short time window using a spinning slotted disk. Only particles that arrive at the velocity filter when the slot is in the correct position will make it through. By adjusting the time when the vacuum arc fires relative to the position of the slot, only particles that are traveling in a certain velocity range will make it through the filter. Due to the duration of the arc, this method is more accurate with longer flight times, i.e. lower velocities.

The primary mechanism that determines the MP charge after the vacuum arc has extinguished is the thermionic emission. A model of the thermionic emission was developed to calculate the charge on the ejected MPs. From the model, the electric field has a significant effect on the MP charge. However, after entering the electric field region, the MP reaches a charge 80% of its final value within 1% of its flight time. This fast response of the MP charge to the electric field, allows the approximation of constant MP charge used during the experimental calculations. Although the electric field affects the charge, an electric field could possibly be employed in an attempt to reduce MP contamination on a spacecraft. The knowledge gained by employing an electric field in this experiment was important to help develop a method of deflecting MPs from their original trajectory.

The model results indicate that the macroparticle charge after the arc has extinguished is almost independent of the charge during the arc. When the arc extinguishes, and there is no plasma to charge the MP negatively, thermionic emission dominates the charging of the MP, resulting in a positive charge. As the MP charge increases, the thermionic emission continues, but emitted electrons are attracted back to the particle due to its local potential well resulting in an asymptotic limit to charge, an effect amplified by particle cooling. As the particles enter the deflecting electric field, the potential well around the particle is altered to the point where more electrons are able to escape. This causes the charge on the MP to increase, until the local electric field around the MP is strong enough to dominate the potential in the vicinity of the MP and reduce or eliminate the effect of the external electric field.

An early model of the thermionic emission of the MPs by Keidar³⁹ determined that the final accumulated charge approximately follows:

$$q = C_2 D^\gamma \quad 5-1$$

where C_2 is a constant and γ is approximately 1.0 for particles larger than $D = 2 \mu\text{m}$.³⁹ A curve fit of the experimental data (see Figure 3.12 - Figure 3.17) indicates that $\gamma \approx 2$ and $C_2 \approx 1000$. By including the effect of the electric field in the model of the MP thermionic emission as described in Chapter 4, the value of gamma increases from 1.0 to 2.0 for a starting temperature $T_o = 1750 \text{ K}$, and 1.6 for $T_o = 3500 \text{ K}$ (see Figure 4.12), which more closely matched the experimental results. For the $T_o = 1750 \text{ K}$ case, the magnitude of the charge is lower than the experimental data (Figure 4.12). Although the temperature of the MP is not well known, models of the cathode spot, as well as the effect that the plasma has on the MP temp indicate that the MP temp after the arc will be greater than 2200 K.

The difference between the model described above and the experimental data is likely to be accounted for by a more precise model of the electron motion around the MP. The assumption of radial electron trajectory is an approximation of the actual electron motion, and a more in-depth analysis is suggested as future work.

Due to their interaction with the plasma, macroparticles ejected from the cathode spot of a vacuum arc are initially charged negatively due to the higher electron mobility. In a pulsed arc, once the vacuum arc extinguishes thermionic emission from the particle will begin to dominate, resulting in a positive charge. This will also be the case for a DC arc, because the plasma density will decrease as the particle travels away from the vacuum arc source. As the particle travels away from the spacecraft, both the positively charged particle and the emitted electrons may collide with the spacecraft, affecting the charge on the spacecraft. If the particle does not collide with the spacecraft, it will solidify into a solid copper sphere in less than 100 ms for a 10 μm particle due to heat loss due to radiation and evaporation. For a typical velocity of 100 m/s this will occur about 10 meters from the spacecraft.

During the experiment, the trajectory of MPs larger than 1 μm in diameter was changed by no more than approximately 5° . This was done using a relatively strong electric field. Larger particles on the order of 10 μm in diameter were deflected less than 1° . A system of electric fields could be used to reduce MP contamination on a spacecraft, but care would have to be taken in the design of such a system because of the limited effect that the electric field has on the larger MPs.

5.2 Future Work

There are two areas where improvements can be made to the described work. First, improvements to the model should be made in order to better represent the motion of the electrons around the MP. Currently, the trajectory of the electrons is assumed to be radial. A first step toward the improvement of the model would be to use a differential equation solver to calculate the trajectory of an electron emitted from the MP surface and to determine the kinetic energy needed to escape the MP. In this way, a different function for $\Delta\Phi$ in Eq. 4-12 could be calculated that would better establish the energy required by an electron to escape the potential well of the MP. A further step would be to perform a Monte Carlo type analysis including all possible electron trajectories and electron velocities. This type of analysis was done for a particle inside a plasma in Ref. 51. Once these improvements have been made to the model of the thermionic emission, the addition of the model used to determine the MP charge and temperature inside the arc should be added in order to lock down the initial conditions.

Improvements or modifications to the experiment itself are also suggested. Below are some supplementary tests to refine the data.

- By performing a test with a shorter pulse length, the error associated with not knowing the formation time of the MP could be greatly reduced. This would reduce the error due to the uncertainty in MP velocity, but would greatly increase test duration because less mass will be ejected per pulse.
- A more detailed survey of the witness plate using a higher resolution could increase the amount of usable data for smaller MPs. Currently, $\times 200$ magnification was used to map the witness plate. Increasing the magnification by a factor of 2 may provide data about the charge of particles approximately $1\ \mu\text{m}$ in diameter and smaller. Doubling the SEM magnification will quadruple the time required to map the witness plate from ~ 6 hours to ~ 24 .
- By modifying the electric field strength, the effect of the E-field on the charge could be established. Increasing the electric field has a greater effect on larger MPs than it does on smaller ones. Thus, if the electric field changed, the slope of the charge vs. diameter would be changed, along with the magnitude Figure 3.17. This could then be used to refine the model discussed in Chapter 4.
- One of the limitations while performing the experiments has been the extended test duration. The primary reason for this is that few macroparticles were collected per pulse because of the small size of the two orifices, and the number of macroparticles formed during one pulse. By increasing the pulse width, the number of MPs per coulomb of current transfer increases.²² However, increasing the pulse width reduces the effectiveness of the time-of-flight velocity filter. If a velocity filter were developed which did not rely on the time of flight of the MPs, the pulse length could be significantly increased, increasing the number of MPs collected, or decreasing the duration of a single test.
- If a method such as a quartz crystal microbalance could be used to measure the mass of collected particles, in conjunction with a charge amplifier system to simultaneously measure the charge, a deflecting electric field as well as an SEM scan might not be necessary.

Appendix A

Velocity Filter Timing Circuit

In order for the velocity filter to work properly, the thruster must fire at a specific time relative to the orientation of the velocity filter disk. A circuit was designed and implemented to accomplish this.

The orientation of the disk is determined by using a light/LED sensor combination to send a signal when one of the three velocity filter disk slots is located at the 12 o'clock location. Depending on the velocity of the particles desired, the thruster must fire anywhere between 200 μs and 1100 μs before that slot reaches the orifice at the 6 o'clock position. The LED sensor circuit sends a signal to a timer circuit which generates the delay pulse. The length of this delay pulse determines when the thruster will fire, so in order to adjust the velocity of particles transmitted, the delay pulse is adjustable. For the setup in this work, the delay pulse is adjustable from approximately 6.9 to 8.2 ms using a 10 turn potentiometer.

At the end of the delay pulse, a firing pulse circuit generates a pulse that is sent to the SCR/Thruster Firing Circuit as well as an Inhibit Pulse Circuit. The Thruster Firing Circuit activates an SCR to fire the trigger pulse. The Inhibit Pulse Circuit sends an inhibit pulse to the Delay Pulse Circuit to keep the thruster from firing uncontrollably. This circuit determines the approximate thruster firing rate. Figure A.1 is a diagram showing the timing of the pulses from the various parts of the velocity filter timing circuit. Figure A.2 is a flow diagram of the complete circuit.

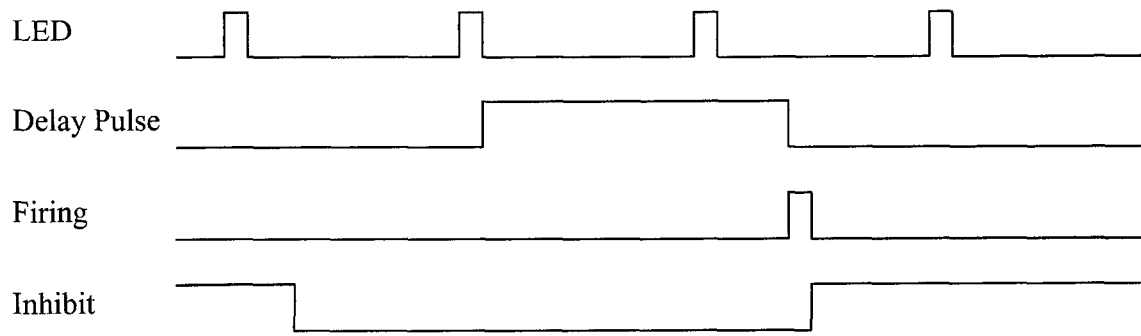


Figure A.1 Pulse timing diagram for the velocity filter timing circuit

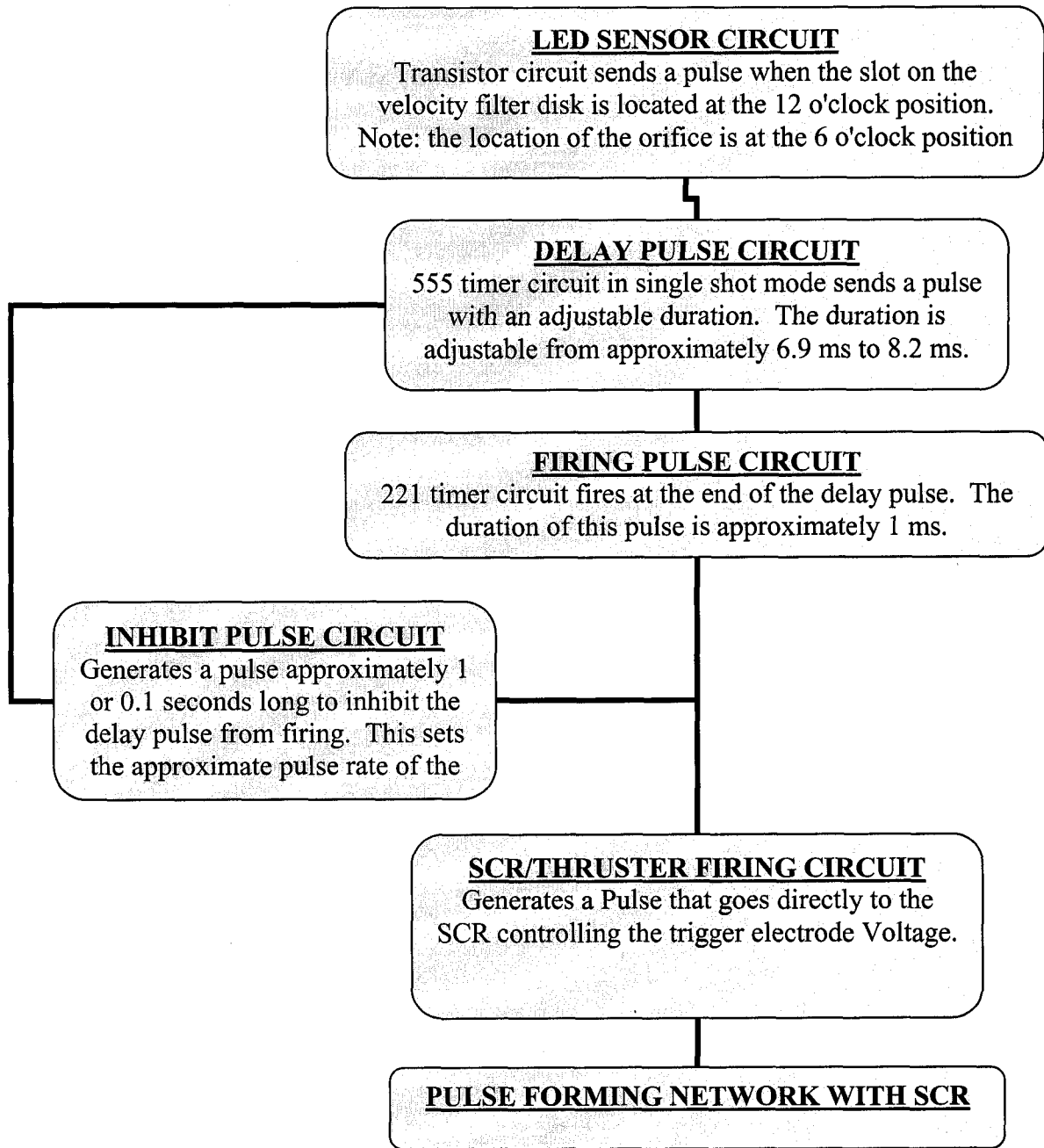


Figure A.2 Flow diagram for the velocity filter timing circuit

List of References

- ¹ Qi, N., Schein, J., Binder R., Krishnan, M., "Compact Vacuum Arc Micro-Thruster for Small Satellite Systems," Joint Propulsion Conference, AIAA 2001-3793, 2001
- ² Schein, J., Qi, N., Binder, R., Krishnan, M., Ziemer, J.K., Polk, J.E., Anders, A., "Inductive energy storage driven vacuum arc thruster," Review of Scientific Instruments, Vol. 73(2), 2002, pp 925
- ³ M.Keidar, J.Schein, K.Wilson, A.Gerhan, M.Au, B.Tang, L.Idzkowski, M.Krishnan, I.I.Beilis, "Magnetically enhanced vacuum arc thruster," Plasma Source Science & Technology, Vol. 14, 2005, pp.661-669
- ⁴ Anders, A., Brown, I.G., MacGill, R.A., and Dickinson, M.R., "'Triggerless' Triggering of Vacuum Arcs," Journal of Physics D: Applied Physics, Vol. 31(7), 1989, pp 584
- ⁵ Anders, A., Schein, J., Qi, N., "Pulsed vacuum-arc ion source operated with a 'triggerless' arc initiation method," Review of scientific instruments, Vol. 71, 2000, pp 827
- ⁶ Rysanek, F., Hartman, J., Schein, J., Binder, R., "MicroVacuum Arc Thruster Design for a CubeSat Class Satellite," USU Conference on Small Satellites, SSC02-I-2, 2002
- ⁷ *Space News* 5-September 2006, "Recent CubeSat Losses Spur Renewed Development" by Leonard David(http://www.space.com/spacenews/archive06/cubesat_0904.html)
- ⁸ Tang, B., Idzkowski, L., Au, M., Parks, D., Krishnan, M., Ziemer, J., , "Thrust improvement of the Magnetically Enhanced Vacuum Arc Thruster (MVAT)," International Electric Propulsion Conference, IEPC 2005-304, 2005
- ⁹ Boxman, R.L. "Early History of Vacuum Arc Deposition" IEEE Transactions on Plasma Science, Vol. 29(5), 2001, pp 759
- ¹⁰ Boxman, R.L., Martin, P.J., Sanders, D.M., *Handbook of Vacuum Arc Science and Technology*, Preface
- ¹¹ Hantzsche, E., "Theory of the expanding plasma of vacuum arcs," Journal of Physics D: Applied Physics, Vol. 24, 1991, pp 1339
- ¹² Harris, L.P., "Arc Cathode Phenomenon" in *VACUUM ARCS, Theory and Application*, J.M. Lafferty Ed., New York: Wiley, 1980, p120
- ¹³ Beilis, I.I., "State of the Theory of Vacuum Arcs," IEEE Transactions on Plasma Science, Vol. 29(5), 2001, pp 657

- ¹⁴ Djakov, B.E., Holmes, R., "Cathode Spot Division in Vacuum Arcs with Solid Metal Cathodes," *Journal of Physics D: Applied Physics*, Vol. 4, 1971, pp 504
- ¹⁵ Juttner, B., "Formation time and heating mechanism of arc cathode craters in vacuum," *Journal of Physics D: Applied Physics*, Vol. 14, 1981, pp 1265
- ¹⁶ Boxman, R.L., Martin, P.J., Sanders, D.M., *Handbook of Vacuum Arc Science and Technology*, Chapter 3 Cathode Spots,
- ¹⁷ Anders, S., Juttner, B., Pursch, H., Siemroth, P., "Investigations of the current density in the Cathode Spot of a Vacuum Arc.," *Contributions to Plasma Physics*, Vol. 25(5), 1985, pp 467
- ¹⁸ Hantzsche, E., Juttner B., "Current Density in Arc Spots," *IEEE Transactions on Plasma Science*, Vol. 13(5), 1985, pp 230
- ¹⁹ Anders, S., Anders, A., "On Modes of Arc Cathode Operation," *IEEE Transactions on Plasma Science*, Vol. 19(1), 1991, pp 20
- ²⁰ Tuma, D.T., Chen, C.L., Davies, D.K., "Erosion products from the cathode spot region of a copper vacuum arc," *Journal of Applied Physics*, Vol. 49(7), 1978, pp 3821
- ²¹ Kimblin, C.W., "Erosion and Ionization in the Cathode spot regions of vacuum arcs," *Journal of Applied Physics*, Vol. 44(7), 1973, pp 3074
- ²² Daalder, J.E., "Components of Cathode erosion in vacuum arcs," *Journal of Physics D: Applied Physics*, Vol. 9, 1976, pp 2379
- ²³ Anders, A., Yushkov, G.Y., "Ion flux from vacuum arc cathode spots in the absence and presence of a magnetic field," *Journal of Applied Physics*, Vol. 91(8), 2002, pp 4824
- ²⁴ Hantzsche, E., "Mysteries of the Arc Cathode Spot: a retrospective Glance," *IEEE Transactions on Plasma Science*, Vol. 31(5), 2003, pp 799
- ²⁵ McClure, G.W., "Plasma expansion as a cause of metal displacement in vacuum-arc cathode spot," *Journal of Applied Physics*, Vol. 45(5), 1974, pp 2078
- ²⁶ Boxman, R.L., Goldsmith, S., "The interaction between plasma and macroparticles in a multi-cathode-spot vacuum arc," *Journal of Applied Physics*, Vol. 52(1), 1981, pp 151
- ²⁷ Moizhes, B.Y., Nemchinskii, V.A., "Erosion and Cathode Jets in a Vacuum Arc," *Soviet Physics Technical Physics*, Vol. 25(1), 1980, pp 43
- ²⁸ Harris, L.P., "A Mathematical Model for Cathode Spot Operation," *Proceedings VIII International Symposium on Discharge and Electrical Insulation in Vacuum*, F1, 1978

- ²⁹ Davis, W.D., Miller, H.C., "Analysis of the Electrode Products Emitted by dc Arcs in a Vacuum Ambient," *Journal of Applied Physics*, Vol. 40(5), 1969, pp 2212
- ³⁰ Plyutto, A.A., Ryzhkov, V.N., Kapin, A.T., "High Speed Plasma Streams in Vacuum Arcs," *Soviet Physics JETP*, Vol. 20(2), 1965, pp 328
- ³¹ Wieckert, C., "A Multicomponent Theory of the Cathodic Plasma Jet in Vacuum Arcs," *Contributions to Plasma Physics*, Vol. 27, 1987, pp 309
- ³² Shalev, S., Boxman, R.L., Goldsmith, S., "Velocities and Emission Rates of Cathode-Produced Molybdenum Macroparticles in a Vacuum Arc," *Journal of Applied Physics*, Vol. 58(7), 1985, pp 2503
- ³³ Shalev, S., Boxman, R.L., Goldsmith, S., "MacroParticle Dynamics During Multi-CathodeSpot Vacuum Arcs," *IEEE Transactions on Plasma Science*, Vol. 14, 1986, pp 59
- ³⁴ Boxman, R., Goldsmith, S., "Principles and Applications of Vacuum Arc Coatings," *IEEE Transactions on Plasma Science*, Vol. 17(5), 1989, pp 705
- ³⁵ Keidar, M., Beilis, I.I., Aharonov, R., Arbilly, D., Boxman, R.L., Goldsmith, S., "Macroparticle distribution in a quarter-torus plasma duct of a filtered vacuum arc deposition system," *J. Phys D: Applied Physics*, Vol. 30, 1997, pp 2972
- ³⁶ Keidar, M., Aharonov, R., Beilis, I.I., "Influence of an electric field on the macroparticle size distribution in a vacuum arc," *Journal of Vacuum Science and Technology A*, Vol. 17(5), 1999, pp 3067
- ³⁷ Keidar, M., Beilis, I.I., Boxman, R.L., Goldsmith, S., "Nonstationary Macroparticle Charging in an Arc Plasma Jet," *IEEE Transactions on Plasma Science*, Vol. 23(6), 1995, pp 902
- ³⁸ Jahn, *Physics of Electric Propulsion*, Chapter 5, New York: McGraw-Hill 1968
- ³⁹ Rysanek, F., Burton, R.L., Keidar, M., "Macroparticle Charging in a Pulsed Vacuum Arc Thruster Discharge" 42nd AIAA/ASME/SAE/ASEE Joint Propulsion Conference, Sacramento, CA 2006.
- ⁴⁰ Particle Analysis Routine written by Stefan Vinzelberg, Atomic Force F&E GmbH, DE-68259 Mannheim
- ⁴¹ Chapter 14-6, *Metals Reference Book*, Smithells, Colin J. Editor, 6th Edition, Boston: Butterworths 1983
- ⁴² Perry, R. and Green, D., *Perry's Chemical Engineers' Handbook*, 7th Edition, Chapter 2, New York : McGraw-Hill, 1997

- ⁴³ Anders, A., MacGill, R.A., McVeigh, T.A., "Efficient, compact power supply for repetitive pulsed, "triggerless" cathodic arcs," *Review of scientific instruments*, Vol. 70(12), 1999, pp 432
- ⁴⁴ Brown, I.G., "Vacuum Arc Ion Sources," *Review of scientific instruments*, Vol. 65, 1994, pp 3061
- ⁴⁵ Panorama Factory, Software Package, Version 4.2 and Version 2.4, John Strait & Smoky City Design, LLC, Copyright 1999-2006
- ⁴⁶ ImageJ, Software Package, Ver. 1.34s, National Institute of Health, USA
- ⁴⁷ Abbott, E.J., and Goldschmidt, E., "Surface Quality, a Review of "Technische Oberflächenkunde" by G.Schmaltz," *Mechanical Engineering*, Vol. 59(11), 1937, pp 813
- ⁴⁸ Holman, J.P. *Experimental methods for Engineers*, 6th Ed. Chapter 3, p 45
- ⁴⁹ Keidar, M., Beilis, I.I., Boxman, R.L., Goldsmith, S., "Transport of macroparticles in magnetized plasma ducts." *IEEE Transactions on Plasma Science.*, Vol. 24, 1996, pp.226-234,
- ⁵⁰ Keidar, M., Beilis, I.I., Boxman, R.L., Goldsmith, S., "Macroparticles interaction with a substrate in cathodic vacuum arc deposition," *Surface & Coatings Technology.*, Vol. 86/87, 1996, pp.415-420
- ⁵¹ Delzanno, G.L., Lapenta, G., and Rosenberg, M., "Attractive Potential around a Thermionically emitting MicroParticle," *Physical Review Letters*, Vol. 92(3), 2004
- ⁵² Shukla, P.K., and Mamun, A.A., *Introduction to Dusty Plasma Physics*, London, Institute of Physics publishing, 2002
- ⁵³ Sodha, M.S., and Guha, S., "Physics of Colloidal Plasmas," *Advances in Plasma Physics*, Vol. 4, 1971, pp 219
- ⁵⁴ Ashcroft, N. W., and Mermin, N. D., *Solid State Physics*, Saunders, 1976
- ⁵⁵ Swanson, L.W., and Bell, A.E., "Recent Advances in Field Electron Microscopy of Metals," *Advances in Electronics and Electron Physics*, Vol. 32, 1973, pp 193
- ⁵⁶ Sodha, M.S., "Thermionic Emission from Spherical Metallic Particles," *Journal of Applied Physics*, Vol. 32, 1961, pp 2059
- ⁵⁷ Jackson, J.D., *Classical Electrodynamics*, 2nd Ed. Wiley & Sons, New York, 1975

- ⁵⁸ Madou, M. J., *Fundamentals of MicroFabrication: The Science of Miniaturization 2nd Ed.*, CRC Press LLC, Boca Raton, FL, 2002
- ⁵⁹ F. Geiger, C.A., Busse, R.I., Loehrke, "The Vapor Pressure of Indium, Silver, Gallium, Copper, Tin, and Gold Between 0.1 and 3.0 Bar" *International Journal of Thermophysics*, Vol. 8(4), 1987
- ⁶⁰ Mathematica, Software package, Version 5.0, Wolfram Research, Inc., USA
- ⁶¹ Tipler, Paul A. and Llewellyn, Ralph A., *Modern Physics*, 3rd Ed., W.H. Freeman, 1999.
- ⁶² Nagata, K., Nagane, T., and Susa, M., "Measurement of Normal Spectral Emissivity of Liquid Copper," *ISIJ International*, Vol. 37(4), 1997, pp 399
- ⁶³ Watanabe, H., Susa, M., Nagata, K. "Discontinuity in normal spectral emissivity of solid and liquid copper at the melting point", *Metall. Mater. Trans. A, Phys. Metall. Mater. Sci.* Vol 28A(12) 1997
- ⁶⁴ Dokko, W., Bautista, R.G. "The normal spectral emissivity measurements on liquid copper" *Metallurgical Transactions B (Process Metallurgy)*, v 10B, n 3, Sept. 1979, 450-3
- ⁶⁵ Cagran, C., Brunner, C., Seifert, A., Pottlacher, G. " Liquid-phase behaviour of normal spectral emissivity at 684.5 nm of some selected metals", *High Temperatures - High Pressures*, Vol 34, 2002, p669
- ⁶⁶ E. W. J. Mitchell; J. W. Mitchell, "The Work Functions of Copper, Silver and Aluminium" *Proceedings of the Royal Society of London. Series A, Mathematical and Physical Sciences*, Vol. 210, No. 1100.(Dec. 7, 1951), pp. 70-84.

Author's Biography

Filip Rysanek was born on April 22, 1975 in Czechoslovakia. His family escaped from Czechoslovakia in 1981 and eventually settled in St. Louis MO, where he graduated from Parkway South High School in 1993. While working on his Bachelor's degree in Aeronautical and Astronautical Engineering at the University of Illinois at Urbana-Champaign (UIUC), he worked on various engineering projects as a Co-Op student at Fermi National Accelerator Laboratory in Batavia, Illinois. After completing his B.S. in May 1998, he continued on for his Master of Science in the Electric Propulsion Group under Dr. Rodney Burton at UIUC. His M.S. research on the performance and heat loss of a coaxial electrothermal pulsed plasma thruster was completed in May 1998. While working on his Ph.D. at the University of Illinois, he was the propulsion lead for the university's 2 kg CubeSat project. As the propulsion lead, he helped to design and integrate a four vacuum arc thruster propulsion system from Alameda Applied Sciences Corp (AASC) in San Leandro, CA. To this end, he interned with AASC in the summer of 2003, and returned the following summer to characterize the plume of a coaxial vacuum arc thruster. Filip married Jennifer Hargens on August 9th, 2003, a fellow Ph.D. student in the Aerospace Engineering department. Near the end of his Ph.D., he worked with the Chemical Oxygen Iodine Laser Group to help design a new basic Hydrogen Peroxide (BHP) delivery system. He also helped implement a web based inventory database for the Aerospace Engineering department business office. His Ph.D. work on the charge of macroparticles ejected from a vacuum arc was completed in December 2006.